

QUANTUM ACOUSTICS
WITH LITHIUM NIOBATE NANOSTRUCTURES

A DISSERTATION
SUBMITTED TO THE DEPARTMENT OF APPLIED PHYSICS
AND THE COMMITTEE ON GRADUATE STUDIES
OF STANFORD UNIVERSITY
IN PARTIAL FULFILLMENT OF THE REQUIREMENTS
FOR THE DEGREE OF
DOCTOR OF PHILOSOPHY

Patricio Arrangoiz-Arriola
August 2019

© 2019 by Patricio Arrangoiz Arriola. All Rights Reserved.
Re-distributed by Stanford University under license with the author.



This work is licensed under a Creative Commons Attribution-
Noncommercial 3.0 United States License.
<http://creativecommons.org/licenses/by-nc/3.0/us/>

This dissertation is online at: <http://purl.stanford.edu/hp858nr1426>

I certify that I have read this dissertation and that, in my opinion, it is fully adequate in scope and quality as a dissertation for the degree of Doctor of Philosophy.

Amir Safavi-Naeini, Primary Adviser

I certify that I have read this dissertation and that, in my opinion, it is fully adequate in scope and quality as a dissertation for the degree of Doctor of Philosophy.

Martin Fejer

I certify that I have read this dissertation and that, in my opinion, it is fully adequate in scope and quality as a dissertation for the degree of Doctor of Philosophy.

Patrick Hayden

Approved for the Stanford University Committee on Graduate Studies.

Patricia J. Gumpert, Vice Provost for Graduate Education

This signature page was generated electronically upon submission of this dissertation in electronic format. An original signed hard copy of the signature page is on file in University Archives.

A mamá, papá, Santi, Jero, y Vale.

Abstract

Phononic crystals are today the most sophisticated technology for manipulating acoustic waves on the surface of a chip. As such, ordinarily these devices can be described by the classical physics of elasticity; accessing a regime where their behavior is manifestly quantum mechanical has so far remained elusive. One way of reaching this regime would be to use a superconducting qubit to monitor and control the acoustics. Such ‘quantum acoustic’ devices would have wide-ranging applications to quantum transduction, sensing, and information processing.

In this thesis I present a collection of works that lay the groundwork for realizing this vision. First I introduce a technique for calculating coupling strengths between superconducting circuits (which include, but are not restricted to, transmon qubits) and arbitrary piezoelectric nanostructures. I then present the first demonstration of direct, resonant coupling between a superconducting circuit and a phononic-crystal-defect resonator (PCDR). This required developing a fabrication process that combines superconducting microwave circuits and suspended lithium niobate nanostructures in a fully integrated, on-chip platform. I then present results from a later generation of devices, including the demonstration of a transmon qubit and an array of PCDRs in the strong coupling regime. Finally, using these same devices I show we can generate a strong dispersive interaction that results in phonon-number-dependent splitting of the qubit spectroscopic line. This constitutes the first observation of the quantized energy levels of a nanomechanical oscillator, taking us back to the original scientific motivation of directly observing the quantum mechanical nature of a (confined) acoustic wave. Needless to say, such dispersive physics also has applications in quantum sensing and information processing. I conclude with a discussion on future experiments along that direction, including quantum nondemolition measurements of single phonons and generation of coherent state superpositions (a.k.a. cat states) of mechanical motion.

Preface

Five years ago, during my first week at Stanford, I told Amir I wanted to put wires near a silicon optomechanical crystal to read out its motion using an electrical circuit. That was a fairly stupid idea of course, but it set the tone for what I wanted to do in my PhD. Over the first couple of years Amir and I refined the concept and later, Alex and I, propelled by a tsunami of luck, brainstormed, built, and tested the devices that would eventually become this dissertation. What resulted, although similar in spirit, turned out to be much more interesting than that original idea of 2014.

It is now my job to tell how it all happened.

Acknowledgments

The success and accomplishments that resulted from my PhD do not belong to me. They belong to all of the people who have touched my life up until this point. First and foremost I would like to thank Amir for being an outstanding research advisor over the past five years. Amir, the freedom (and means) that you gave me to pursue my interests is quite rare in grad school, as I have now come to appreciate. I interpret this gesture as an expression of your deep belief in my abilities and I am deeply grateful for this vote of confidence. This freedom has allowed me to feel ownership and eventually take the helm of the research program that we started, even though it is now my turn to pass it on to the younger generations. Despite this great degree of autonomy (and responsibility) that you granted to me, I think that, ultimately, it was your intuition for physics problems and your dogged insistence to stay focused on the things that matter what made this program a great success. Eventually these personality traits transferred and I learned to stay deeply focused, with eyes locked on the mission. You have made an indelible mark on me, without which I would not feel the right to call myself a scientist.

Numerous other teachers and mentors have contributed to my formation as a scientist during the PhD years. Jeff Hill, in addition to being a great friend and colleague, you taught me to stay disciplined and more importantly to stay *honest*. Needless to say, the training I received from you in the cleanroom and in the lab was invaluable. Most importantly, all of us (past, present, and future members of the group) are indebted to you for your enormous contribution to designing, building, and setting up the lab. Patrick Hayden, thank you for teaching such an outstanding quantum mechanics course at Stanford and for always being a source of inspiration. I admire your passion for teaching, your patience, and your clarity of thought. I also want to thank Aash Clerk, Florian Marquardt, Marc-Antoine Lemonde, Oriol Romero-Isart, and Andrew Cleland for the deeply influential discussions we had at Les Houches and the years beyond.

At Caltech, several people encouraged and shaped my passion for physics with lots of patience and dedication. To the late Tom Tombrello, whose true, selfless love for students left such a deep mark in the fabric of Caltech undergraduate life. Dave Stevenson, thank you for being such a patient teacher during my young and restless years. Paul Bellan, you were a caring research mentor and teacher. I will never forget how you decided to teach the plasma physics course despite the fact that

I was the only student in it that year. Even though I didn't end up pursuing plasma physics as a career, you instilled a love for physics and experiments that I am deeply grateful for. Frank Rice, thank you for teaching me that experiments are as much about art as they are about science, and Michael Roukes, your crystal-clear delivery of your low-noise electronics lectures is what inspired me to pursue a PhD in quantum devices.

High school, more than a formative stage, was an age of discovery. Many teachers played a key role in helping me unearth my calling. Michael Gorman, Renato Galicia, and Patricia Hernández from Colegio Marymount, Francisco Aquino Roblero from UAEM, Juan Vazquez-Montejo from Cinvestav Mérida and rest of the crew at CIMAT, thank you all for your dedication to teaching.

Throughout these past five years at Stanford, my colleges and labmates have provided a pillar of support that has been essential to surviving — and even enjoying — such an intense experience.

Alex, you were the best lab and cleanroom partner I could have ever hoped for. Even though I started off as your mentor, your intense dedication and outstanding ability to learn meant that you and I quickly became equals. Your selfless passion for making things better and to do the ‘invisible’ work that makes everything function played a fundamental role in our success. Without you none of this would have been possible, and I cannot think of a better person to carry the torch of quantum acoustics.

Chris, what are you doing reading this. Get. To. Work. Slacker. We ain’t in Florida anymore. But in all seriousness, you have been an essential part of the lab for all these years, and an awesome friend. Your outstanding and prolific contributions and the energy you inject to it all has made this lab 10^{18} times better than it would have been without you. Now that this endeavor is over for me I look forward to what you will build in the next few years, and for you to teach me the way of the sea. I got my eyes on them halibuts.

Rishi. Oh Rishi. What can I say. We were there since the beginning. You and Chris are the reason I joined this lab. All I heard was that there was this Amir guy coming to Stanford and that you and Chris were joining and that it would be so much fun building the lab and that we would carry the torch of optomechanics and that ohhhh, it might become intense but that it would be a fulfilling experience, you know, to build it all from scratch. Such a dubious proposition may have fallen on deaf ears were it not for that trust-inspiring demeanor that you carry around. Like Chris, you have continuously lifted the morale of the group, with an uncanny ability to stay positive at all times.

Jeremy, you and I were cleanroom soldiers since the very beginning. You may underestimate the extent to which your resilience and your strength has inspired me to push onward when the going gets tough. You took the lead of the most difficult project in the lab and elevated it (and the entire field) to new heights. What you’ve done in lab is remarkable, but the family that you have managed to build while doing all of this is even more remarkable. Only a man of values can accomplish such things.

Tim, quit snooping around. This is personal stuff OK? I thought you were here for the circuit QED stuff. What a guy this Tim. You are such a positive force in the group. I guess that's all I have to say. I had to put you up here because, you know, seniority. No but really, you're an incredibly gifted physicist and engineer, and your problem-solving ability has no better metaphor than a bulldozer. We are all very lucky that you decided to join the group. To learning wheelies, manuals, and bunny hops, in that order. I'm coming for you.

Marek, erudite of the quantum. I have always looked up to you and can only hope to one day become a tenth as good as you are. Your mathematical reasoning is remarkable and very much needed in a field that often lacks rigor. Your derivations make everybody drool. I hope our paths cross once again in the future.

Rrrrrraphaël, sorry for butchering your name continuously for the past three and something years. You have put up with it very well, which I think speaks of a larger truth about you. You have an incredible patience and resilience when doing research, and an unflinching commitment to do what is right, even if it isn't the easiest route. I very much look forward to see where time will take you. Thank you for being a trustworthy and mature friend all these years.

Nathan, The God of Liftoff. You are a cleanroom soldier as well, and your efforts at last paid off. What a nice experiment you did in the end. And it's crazy to think you're not even done yet, despite such a nice success. With the skill set you've acquired, I'm very eager to see what new crazy idea you will work on and, I'm sure, carry to fruition.

Zhaoyou, you are Marek's padawan for a reason. Your amazing talents take this group to a higher level. Thank you for your support in the very intense months that followed our number splitting experiment.

Wentao, you are such a character! Your quirkiness makes Feynman look like an altar boy. And your gift for building things is truly jaw-dropping. Whoever in your life encouraged you to do physics did a favor to you and the world. It is your calling.

Agnetta, thank you for injecting so much positive energy to the group. It really is funny that you ended up in quantum acoustics, given, you know, ahem... your family tree, but it fits you extremely well and even at year two you are already making incredibly complex and original contributions. It gives me peace of mind that you and Alex will be taking the helm.

Okan, one day you will get old and have a beer belly and I will beat you in the mile. Don't even think that you will get away with it. Thank you for bringing such good spirits to the group.

Felix, the guy who hasn't even joined the group yet and already appears in the acknowledgements of a dissertation. This should speak more than a thousand words. Even though we won't overlap I'm sure I'll be seeing you around in the coming years. I cannot wait to see the remarkable things you'll do.

Yanni, last but certainly not least. I wish you all the best in your journey up in the East (inferior) Coast. Your work here with us culminated in a beautiful and very useful paper. Thank you for

bringing positivity and lightheartedness to the group.

Outside the lab, friends have always been there for me, even during periods of ‘silence’ when I was so intensely focused in research it sometimes took me days to respond to messages. I am sorry I acted that way, it was never my intention to be unavailable. Thank you for being so loyal and understanding, all of you: Anish, Michael, Karan, Juan, Marcus, Jules, Lan, Ani, Stan, Nikhil, Behrad, Jenny, Pau, Jaco, Imanol, Bernardo, Eugene, Prastuti, Emmett, Sofia, Sam, Nico, Dori, and many more whose paths have crossed with mine at some point. I look forward to cultivating our friendship for the years to come.

Santi, Jero, Vale, mamá, papá. You have kept me grounded all these years. Thank you for your unwavering support during all my crazy pursuits. Time has separated us, but I sincerely hope and will devote all of my strength to making sure we converge in the near future. You have taught me what matters most. Los quiero más que a nadie.

And to Mamacitas, the best tacos on this side of the border.

Contents

	iv
Abstract	v
Preface	vi
Acknowledgments	vii
1 Introduction	1
1.1 Broad motivation and overarching themes	1
1.1.1 Quantum transduction	2
1.1.2 Quantum sensing	2
1.1.3 Quantum information processing	3
1.2 Background	4
1.2.1 Cavity optomechanics	4
1.2.2 Josephson circuits and mechanical systems: early days	6
1.2.3 Quantum acoustics with surface- and bulk-acoustic waves	6
1.2.4 The need for phononic crystals	7
1.3 Outline of remaining chapters	8
2 Fundamentals	10
2.1 Elastic waves in piezoelectric media	10
2.1.1 Classical continuum theory	10
2.1.2 Quantization	12
2.2 Superconducting circuits	13
2.2.1 Classical circuit theory and quantization	13
2.2.2 Josephson junctions	15
2.2.3 SQUID array resonators	18
2.2.4 Transmon qubits	25

2.3	Piezoelectric coupling	35
2.3.1	Toy model	35
2.3.2	General case	37
3	Calculating couplings to phononic nanostructures	38
3.1	Introduction	38
3.2	Thin-film bulk-acoustic-wave resonator	39
3.2.1	Model	39
3.2.2	Foster synthesis and two-mode Hamiltonian	41
3.2.3	Coupling rate	42
3.3	Lamb-wave resonator	42
3.4	Phononic-crystal-defect resonator	44
3.4.1	Black-box quantization	44
3.4.2	Polariton anharmonicities	47
3.5	Conclusion	49
4	Coupling a superconducting circuit to a PCDR	50
4.1	Introduction	50
4.2	Device design and fabrication	51
4.3	Modeling and measurement results	53
4.4	Outlook	55
5	Resolving phonon-number states	61
5.1	Introduction	62
5.2	Device	63
5.3	Characterization via continuous-wave spectroscopy	64
5.4	Observation of phonon-number splitting	65
5.5	Conclusion	66
6	Outlook	71
A	Supplementary information for Chapter 3	73
A.1	Derivation of two-mode Hamiltonian	73
A.2	Finite element simulations	76
A.3	Foster synthesis for acoustic systems	78
B	Supplementary information for Chapter 4	81
B.1	Reflection spectra	81
B.2	Wide-band characterization of SQUID array resonator	83
B.3	Complete mechanical spectrum of the system	84

B.4	Finite-element simulations	85
B.5	Experimental setup	85
C	Supplementary information for Chapter 5	90
C.1	Device fabrication	90
C.2	Device parameters	91
C.3	Qubit and mechanical oscillator control	92
C.4	Qubit readout	92
C.5	Characterization of qubit and mechanics	94
C.6	Pulse sequence	95
C.7	Flux drift correction and qubit tracking	96
C.8	Phononic-crystal resonator design	97
C.9	Supplementary data	99
C.10	Numerical simulations of qubit spectra	100
C.10.1	System Hamiltonian	100
C.10.2	Master equation simulations	100
C.10.3	Excitation of phonons through the transmon	102
C.11	Optimization of the dispersive coupling χ	102
D	Device fabrication	107
D.1	Process flow	107
D.2	List of abbreviations	108
D.3	List of tools	109
D.4	Details	109
D.4.1	Film thinning	109
D.4.2	Small-scale LN patterning	111
D.4.3	Large-scale LN patterning	114
D.4.4	Microwave base layer deposition	116
D.4.5	Josephson junction growth	117
D.4.6	PCDR electrode deposition	119
D.4.7	Bandage deposition	121
D.4.8	Release mask	122
D.4.9	Dice and release	123
E	List of publications	125
	Bibliography	126

Chapter 1

Introduction

Far from being confined to laboratories, mechanical oscillators are a critical technology that permeates and powers our world. They are everywhere, and their application space is enormous. Think of the fact, for example, that micro- and nanomechanical devices exist in the pockets of billions of people in the form of RF filters, frequency references, accelerometers, gyroscopes, and so on. Interestingly, despite their established success as a *classical* technology, today there is plenty of room to study these devices from the standpoint of *quantum* physics.

Unlike atoms or photons, micro- and nanomechanical oscillators are mesoscopic entities composed of a vast number of atoms, so their behavior is purely classical under ordinary conditions. However, today we know to an extremely high degree of certainty that quantum mechanics ought to hold at all scales, even if its landmark effects such as quantization, superposition, and entanglement are blurred by decoherence in our everyday world. It was Einstein who first postulated that the energy of vibrating solids should be quantized [42], and shockingly, hypothesized that this should hold for arbitrarily large masses¹. However, it was until the late 1970's that the issue of quantum effects in the measurement and control of macroscopic objects became of practical importance. The issue arose in the context of gravitational wave laser interferometers, where it became clear that effects such as shot noise and radiation pressure backaction would ultimately impose limits on the ability to measure the position of a moving mirror [16, 121, 21, 23, 22, 54].

1.1 Broad motivation and overarching themes

Today, the field of mechanical systems in the quantum regime extends far beyond position measurements. At the risk of oversimplification, it is my view that research is now more broadly centered on finding ways to manipulate, stabilize, and characterize the quantum state of mechanical systems, and

¹I would like to credit Amir for this finding. I should also emphasize that I am genuinely shocked by this piece of historical trivia.

of interfacing them to other systems to access new functionalities. There are plenty of motivations for mastering this art, but here I will focus on three examples.

1.1.1 Quantum transduction

First, acoustic waves can effectively mediate interactions between photons — even between photons with wavelengths separated by many orders of magnitude. This is obvious to anyone familiar with acousto-optic modulators, which make it possible to modulate or steer laser light using low-frequency electrical signals. It remains an outstanding challenge to extend this capability to the quantum regime, i.e. to be able to convert, with high efficiency, quantum information encoded in microwave photons to the optical domain [107, 14, 3]. This is desirable as it would enable long-distance communication in quantum networks with nodes that operate at microwave frequencies. Needless to say, having a clear grasp on how to measure and control the state of the mechanical system is crucial. For example, the mechanical oscillator ought to be in its ground state, otherwise it will imprint its thermal noise on the converted photons.

1.1.2 Quantum sensing

Second, because mechanical systems couple to a wide variety of external forces and fields, they can be used as sensors. Think of AFM (which maps the topography of a sample by responding to the repulsive contact force between atoms on the surface and a cantilever), or MEMS accelerometers (which can measure both inertial and gravitational forces), and so on. As I alluded to earlier, it was roughly four decades ago that people began to think of the ultimate limits on the precision of measurements performed on mechanical oscillators. For example, it was found that measurements of the position of a mirror performed with a *classical* probing force — such as an ordinary laser — would be subject to a so-called Standard Quantum Limit (SQL) [22]. In a nutshell, the SQL imposes a limit on the ultimate sensitivity of such a detection scheme through the combination of two sources of noise: the vacuum fluctuations of light (or shot noise), and radiation pressure backaction [21, 97, 34]. Not surprisingly, this limit can be overcome if the mirror is probed with squeezed light [59], or if careful backaction evasion schemes [31, 116] are employed.

More interestingly, rather than modifying the probing force, dramatic sensitivity enhancements can be attained by preparing the mechanical system itself in a ‘special’ quantum state [93], such as a Fock state or a cat state. This was demonstrated recently with a single-ion mechanical oscillator [78], with the ion prepared in a Fock state superposition $|\psi\rangle = (|0\rangle + |n\rangle)/\sqrt{2}$. The prospect of extending these schemes to more massive mechanical objects would be quite exciting.

1.1.3 Quantum information processing

Last, but not least, mechanical degrees of freedom could be used for processing or storing quantum information. In contrast to the previous two examples, which are quite sensible², this one would certainly raise some eyebrows among certain circles. But no one can deny that the field quantum computation is still in its infancy, and that even the most promising approaches to date, such as superconducting circuits, are plagued with uncertainties. At the very least, it is sensible to contend that new, creative ideas will likely be needed to build a large-scale quantum computer, if not a complete paradigm shift.

For this motivating example I will focus on superconducting qubits; it is the natural place to start this discussion because we already employ them in our devices. Whereas these qubits work phenomenally well on their own, and even in small numbers — single qubit and two-qubit gate fidelities are now well above 99% — there is currently no viable path to systems well beyond ~ 100 qubits, let alone to the numbers that will be needed to achieve fault tolerance using existing error correction schemes (many orders of magnitude larger than what is currently available). To my understanding, these scaling difficulties exist for a variety of reasons, which I list here in order of increasing importance.

1. *Footprint.* Because superconducting qubits are resonant microwave circuits, they are quite large, currently occupying an area $\sim 10^5 \mu\text{m}^2$ on the chip. This would impose an upper bound of $\sim 10^5$ on the number of qubits that could be packed onto a 300 mm wafer. It is currently by no means a limitation, but one day it may become one.
2. *Input/output.* Unlike a modern CPU, which has $\sim 10^3$ I/O pins and $\sim 10^9$ transistors, the number of control and readout lines in today’s mainstream quantum computing architectures scales linearly with the number of qubits, with a scaling factor on the order of one. With today’s dilution refrigerator technology, it is difficult to imagine a system that could support the thermal loading associated with the wiring required for $\sim 10^3$ qubits and beyond.
3. *Cross-talk.* Perhaps most importantly, because superconducting qubits are electromagnetic devices, a grid of coupled qubits has parasitic cross-talk that is difficult to suppress. In other words, the physical nature of the hardware makes it difficult to engineer a system that is described exactly by the desired Hamiltonian.

All of these problems could in principle be ameliorated by integrating phononic elements into the hardware. More specifically, one could use a ‘bank’ of mechanical resonators that can each store a qubit, for example using the $\{|0\rangle, |1\rangle\}$ subspace (in the phonon-number basis). These qubits could be manipulated, measured, and entangled with each other using a single superconducting circuit, such as a transmon [83, 92, 50]. Architectures of this flavor enjoy the following advantages:

²No pun intended.

1. phononic-crystal resonators have a footprint $\sim 10 \mu\text{m}^2$
2. a single transmon controls a large number of phononic qubits, and
3. the phononic qubits have no direct cross-talk, as phonons do not propagate through vacuum.

The true utility of phononics in quantum computation is still speculative, but it merits further investigation and the devices I will present in Chapter 5 provide a platform to perform this research.

1.2 Background

It is in part because of these prospects (there are a few more that I will not go into) that the field of mechanical systems in the quantum regime has been so vibrant over the past two decades. Rather than providing a complete survey, in this section I will attempt to trace the train of ideas that ultimately led to this work.

1.2.1 Cavity optomechanics

As mentioned at the start of this chapter, the problem of quantum measurement and control of mechanical systems arose in the context of *cavity optomechanics* [9]. Apart from the usual historical reasons associated with LIGO, this was a very natural context for this problem to arise. This is ultimately because laser light is a very sensitive probe of mechanical motion, so it is not surprising that such probing schemes (as opposed to, say, electronic readout of NEMS) would be the first to run into quantum limits.

In cavity optomechanics, laser light parametrically interacts with the mechanical motion of a cavity mirror via the dependence of the cavity frequency on the mirror position x . Here ‘cavity’ may refer to a variety of different physical implementations. The canonical example is a Fabry-Pérot cavity [32], in which \hat{x} is literally the position of the mirror along the cavity axis. More generally, the cavity may be any deformable dielectric object such as an photonic crystal [40, 24, 102] or a microtoroid [110], in which \hat{x} refers to the amplitude of a particular mechanical mode of the structure. This scheme can also be implemented at microwave frequencies (often referred to as *cavity electromechanics*), where the ‘cavity’ is a resonant LC circuit in which one of the electrodes of a capacitor is allowed to move [119]. In any of these cases, the Hamiltonian is

$$\hat{H}/\hbar = \omega_c(\hat{x})\hat{a}^\dagger\hat{a} + \omega_m\hat{b}^\dagger\hat{b}. \quad (1.1)$$

Here the operators $\hat{a}^\dagger(\hat{a})$ and $\hat{b}^\dagger(\hat{b})$ are the creation and annihilation operators of the cavity and mechanical modes, respectively, $\omega_c(\hat{x})$ is the position-dependent cavity frequency, and ω_m is the mechanical frequency. Typically the cavity frequency can be expanded to linear order in \hat{x} as

$\omega_c(\hat{x}) \approx \omega_c(0) + g_0(\hat{x}/x_{\text{zp}})$, where

$$g_0 = \left. \frac{\partial \omega_c}{\partial x} \right|_{x=0} x_{\text{zp}}, \quad (1.2)$$

and $x_{\text{zp}} = \sqrt{\hbar/2m\omega_m}$ is the magnitude of the zero-point position fluctuations. The rate g_0 is known as the vacuum optomechanical coupling rate and parametrizes the strength with which the mechanical motion perturbs the cavity frequency. The phonon-photon coupling therefore takes the form $\hat{H}_{\text{int}} = \hbar g_0 \hat{a}^\dagger \hat{a} (\hat{b} + \hat{b}^\dagger)$.

In all solid-state systems reported to date, this vacuum coupling rate is orders of magnitude smaller than the optical decoherence rate κ . In order to achieve any appreciable coupling, it is therefore necessary to drive the optical mode with a large coherent pump so as to ‘displace’ the cavity operator $\hat{a} \rightarrow \hat{a} + \alpha$. This linearizes the coupling term in the Hamiltonian as follows:

$$\hat{H}_{\text{int}}/\hbar = g_0 \hat{a}^\dagger \hat{a} (\hat{b}^\dagger + \hat{b}) \rightarrow G(\hat{a}^\dagger + \hat{a})(\hat{b}^\dagger + \hat{b}), \quad (1.3)$$

where $G = |\alpha|^2 g_0$. Without going into further detail (Aspelmeyer *et al.* do so very successfully in Ref. [9]), it is sufficient to say that such a linear interaction severely restricts the range of measurements and operations that can be performed on the mechanical system. To quote the experts, “[w]hen injecting Gaussian optical states, as is the case for the usual laser drive, this can produce arbitrary mechanical Gaussian states [...]” [9]. Gaussian states are indeed very interesting and useful — let us not forget that squeezed light injection, for example, enhances the sensitivity of position measurements beyond the SQL [59]. But they are still a tiny subset of all the possible quantum states that the mechanical system could be prepared in. Moreover, this paradigm is generally limited to measuring only the *position* \hat{x} of the mechanical system. Observing effects such as mechanical energy quantization is therefore fundamentally impossible, because energy and position do not commute: $[\hat{b}^\dagger \hat{b}, \hat{b} + \hat{b}^\dagger] = i(\hat{b}^\dagger - \hat{b}) \neq 0$. There are schemes that attempt to measure \hat{x}^2 directly [120], but observing the quantization of mechanical energy is not possible unless the vacuum coupling g_0 exceeds κ_i (the intrinsic optical decoherence rate) [80], a regime that has remained far out of reach.

Nevertheless, even with these limitations cavity optomechanics has been an extremely successful platform for studying mechanical systems in the quantum regime. To name a few results: first observation of radiation pressure backaction noise (both at low temperature [97] and now at room temperature [34]), ground state cooling [25, 118], observation of zero-point motion [103], backaction evasion [116] and squeezing [131], squeezed light generation [104], entanglement between a mechanical oscillator and a microwave field [90], and even continuous-variable entanglement between two mechanical oscillators [87]. More recently, the introduction of photon counting techniques has enabled more sophisticated experiments, including phonon counting via single-photon detection [33] and heralded (non-deterministic) generation of Bell states of two spatially separated resonators [101]. A complete survey (up to 2014) can be found in Ref. [9].

1.2.2 Josephson circuits and mechanical systems: early days

In parallel to the rapid developments in cavity optomechanics, an alternative line of research was pioneered in the early 2000's by A. Armour, M. Blencowe, A. Cleland, M. LaHaye, M. Roukes, K. Schwab, and others. Here the idea was to couple a superconducting Josephson circuit — such as a single-electron transistor (SET) or a Cooper pair box (CPB) — to a nano-electromechanical system (NEMS). In the case of a CPB, the coupling mechanism is the same as in cavity electromechanics: the motion of the resonator modulates the net capacitance of the CPB and therefore its frequency. These systems can therefore generally be described by the Hamiltonian

$$\hat{H}/\hbar = \frac{1}{2}\omega_q(\hat{x})\hat{\sigma}_z + \omega_m\hat{b}^\dagger\hat{b}, \quad (1.4)$$

which is again similar to the optomechanical Hamiltonian except that instead of a cavity we now have a two-level system (TLS) described by Pauli operators. To my knowledge this was first proposed by Armour *et al.* in 2002 [5]. This paper even outlined a method to use the CPB to generate a superposition of coherent states of the mechanical system, an idea that was far ahead of its time as it has yet to be demonstrated. Nevertheless the idea of using SETs or CPBs to measure and control NEMS was intriguing and produced a number of results, including ultra-sensitive position measurements [62] and backaction cooling [82] using SETs, and the first demonstration of a charge qubit coupled to a NEMS device [63]. In this last experiment the nanomechanical resonator was used to probe the qubit through the CPB-state-dependent dispersive shift of the mechanical frequency. This was an important step in the quest to integrate qubits and NEMS, but the latter still acted very much like a classical readout element.

A few years later Pirkkalainen *et al.* [94] demonstrated a transmon qubit coupled to a NEMS device, and subsequently an experiment where a CPB was used to enhance the optomechanical coupling between a resonator and a superconducting cavity [95]. Finally, last year Viennot *et al.* reported measurements of the ac-Stark shift imparted on a transmon by a micromechanical resonator, approaching the regime where individual phonon-number states are resolvable in the qubit spectrum.

1.2.3 Quantum acoustics with surface- and bulk-acoustic waves

Tempting as it may be, perhaps it would not be fair to refer to the set of experiments described in the previous section as ‘quantum acoustics’. This is because in all cases, the mechanical frequency is fairly low (~ 10 MHz), meaning that even at miliKelvin temperatures there is still a significant thermal phonon population and as a result the mechanics essentially behaves classically. There are a few exceptions to this statement, notably Refs. [98, 125].

In order to demonstrate nontrivial quantum control, A. Cleland had the idea in 2004 to couple a phase qubit to a thin-film bulk-acoustic-wave resonator (FBAR) using *piezoelectricity* [29]. At the time FBARs were already an established technology used for classical RF filters operating at much

higher frequencies (in the GHz) than the capacitive NEMS/MEMS devices discussed in the previous section. Piezoelectric coupling is completely different from the opto/electromechanical coupling mechanism described before. It is a *linear* coupling between the charge degree of freedom of the circuit and the position of the oscillator, caused by a polarization of the material that is linearly induced by strain. As such, the Hamiltonian adopts the form

$$\hat{H}/\hbar = \frac{1}{2}\omega_q \hat{\sigma}_z + \omega_m \hat{b}^\dagger \hat{b} + g \hat{\sigma}_x (\hat{b} + \hat{b}^\dagger). \quad (1.5)$$

This is in fact the well-known Jaynes-Cummings Hamiltonian of quantum optics. If realized, such a system would be conceptually identical to cavity and circuit QED but with photons replaced by phonons. In particular, in the case where the mechanics and the qubit are resonant ($\omega_q \approx \omega_m$) the two systems would coherently exchange quanta if the coupling rate exceeds the decoherence rates, $g \gg \kappa, \gamma$, allowing for full control of the mechanical state within the $\{|0\rangle, |1\rangle\}$ subspace (in the phonon-number basis).

Cleland's 2004 proposal was finally realized by O'Connell *et al.* in 2010 [88]. With a resonance frequency of ~ 6 GHz, their mechanical resonator now operated at a frequency three orders of magnitude larger than any previous experiment in this vein. As a result, the passive refrigeration provided by the cryostat was enough to cool a mechanical device, for the first time, to its quantum ground state. In addition, the fact that the resonator was controlled by a qubit allowed for the preparation of single-phonon Fock states or any superposition $|\psi\rangle = a|0\rangle + b|1\rangle$.

O'Connell's result was an extraordinary achievement in nanofabrication and experimental physics. Perhaps it was because of this that it took another four years for a similar experiment to be published. In 2014, Gustafsson *et al.* [48] reported a transmon qubit coupled to propagating surface-acoustic waves on a GaAs substrate. To this followed a series of similar experiments, including transmon qubits coupled to surface [4, 73, 81, 86] and bulk [26, 58] acoustic wave resonators. In the past year more complex demonstrations have followed, including preparation of multi-phonon Fock states [27] of a bulk wave resonator, arbitrary single-phonon control of a surface-acoustic-wave resonator [109], and quantum state transfer between two transmons using propagating surface-acoustic waves [13].

1.2.4 The need for phononic crystals

These experiments constitute an unprecedented display of quantum control of acoustic waves. They firmly establish superconducting qubits as a valuable tool for metrology and control of mechanical systems. However, all of these approaches suffer from either short qubit and mechanical coherence times, or weak coupling. This is because the sub-micron wavelength of gigahertz-frequency acoustic phonons — far smaller than the scale of the electrodes comprising the qubit circuits — leads to an enormous density of phononic states accessible at the qubit transition frequency. Uncontrolled coupling to phonons is a known source of dissipation in cQED [52], and represents a major challenge

in combining qubits with the strong piezoelectrics needed for phonon sensing and control.

Systems designed to have large coupling rates — mainly the surface wave devices — tend to couple strongly to parasitic modes also, reducing the overall coherence of the qubit as well as the availability of viable operating frequencies. Approaches to mitigating these losses have included tunable couplers that isolate the qubit from the piezoelectric material by rapidly turning off the coupling after interaction [109], or clever transducer design to suppress phonon emission at specific frequencies [114]. On the other hand, bulk wave systems are able to achieve much longer phonon and qubit lifetimes by reducing the fraction of the qubit electric field that overlaps with the piezoelectric [26, 27], which comes at the cost of lowering the coupling strength. It goes without saying that longer lifetimes are of no use when the interaction is slower as well.

This finally brings us to the premise of this dissertation. I contend — and will later show — that there is indeed a way to overcome this seemingly insurmountable tradeoff between coupling and loss: it is to reduce the density of accessible mechanical modes that the qubit can radiate into, by confining the phonons to a very small piezoelectric region where only a few mechanical modes are present at the frequencies of interest. This can be done using *phononic crystals*. For example, by introducing a defect site into a one-dimensional phononic-bandgap structure, it is possible to confine sound waves to a tiny (wavelength-scale) volume with a pristine mode structure [106, 40].

1.3 Outline of remaining chapters

In Chapter 2 I will introduce background material that will serve as a foundation for discussing the main results in later chapters. I will first present a concise treatment of acoustic waves in piezoelectric media and their quantization, followed by a brief review of superconducting circuits, and conclude with an example calculation of piezoelectric coupling rate between a superconducting microwave resonator and a mechanical resonator.

In Chapter 3, I will introduce a practical (though conceptually murkier) method for calculating coupling rates³ [6]. Then in Chapter 4 I will present an experimental realization of the preceding ideas: a tunable superconducting resonator coupled to a phononic-crystal-defect resonator (PCDR)⁴ [7]. This naturally leads to Chapter 5, where I present a transmon qubit strongly coupled to an array of PCDRs — a direct extension of the techniques from previous chapters but now applied to qubit circuits [8]. Finally, also in Chapter 5 I report the observation of the phonon-number states

³This chapter was published as: P. Arrangoiz-Arriola, A.H. Safavi-Naeini, “Engineering interactions between superconducting qubits and phononic nanostructures” *Phys. Rev. A* **94**, 063864 (2016). P.A.-A. performed the work and wrote the paper, with A. H. Safavi-Naeini assisting.

⁴This chapter was published as: P. Arrangoiz-Arriola, E.A. Wollack, M. Pechal, J.D. Witmer, J.T. Hill, A.H. Safavi-Naeini, “Coupling a superconducting quantum circuit to a phononic crystal defect cavity” *Phys. Rev. X* **8**, 031007 (2018). P.A.-A. and E. A. Wollack developed the fabrication process, designed the devices, fabricated the devices, and performed the experiment. P.A.-A. analyzed the data. J. D. Witmer and J. T. Hill contributed to fabrication development. M. Pechal contributed to device design and measurement. P.A.-A. wrote the paper, and A. H. Safavi-Naeini supervised all efforts.

of a single PCDR in the array⁵ [8].

In Chapter 6 I conclude with a discussion on future (and imminent!) experiments enabled by this platform, including quantum nondemolition detection of single phonons and preparation of Schrödinger cat states of mechanical motion. I will also pose what are, in my view, the central questions that we must answer before we can establish phononics as a serious platform for quantum computation.

⁵This chapter was published as: P. Arrangoiz-Arriola*, E. A. Wollack*, Z. Wang, M. Pechal, W. Jiang, T. P. McKenna, J. D. Witmer, R. Van Laer, A. H. Safavi-Naeini, “Resolving the energy levels of a nanomechanical oscillator” *Nature* **571**, 537-540 (2019). P.A.-A. and E. A. Wollack designed and fabricated the device. P. A.-A., E. A. Wollack, W. Jiang, T. P. McKenna, J. D. Witmer, and R. Van Laer developed the fabrication process. Z. Wang, M. Pechal, and A. H. Safavi-Naeini provided experimental and theoretical support. P.A.-A. and E. A. Wollack performed the experiments and analyzed the data. P.A.-A., E. A. Wollack, and A. H. Safavi-Naeini wrote the manuscript, with Z. Wang and M. Pechal assisting. P.A.-A. and A. H. Safavi-Naeini conceived the experiment, and A. H. Safavi-Naeini supervised all efforts. *These authors contributed equally.

Chapter 2

Fundamentals

2.1 Elastic waves in piezoelectric media

2.1.1 Classical continuum theory

We begin this section with a classical treatment of elastic waves in piezoelectric media. In a *continuum* theory, these waves are described by two *pairs* of variables: the electric and displacement fields \mathbf{E} and \mathbf{D} , and the stress and strain tensors S and T , respectively. The coupling between these fields can be expressed as a pair of *linear* constitutive relations written in the so-called stress-charge form [67]:

$$D_i = \epsilon_{ij} E_j + e_{ijk} S_{jk} \quad (2.1a)$$

$$T_{ij} = c_{ijlm} S_{lm} - e_{lij} E_l. \quad (2.1b)$$

Here repeated indices are summed (Einstein convention), c_{ijlm} is the stiffness tensor, ϵ_{ij} is the permittivity tensor, and e_{ijk} is the piezoelectric coupling tensor. These relations tell us everything we need to know about the piezoelectric effect. In English, they say that in a piezoelectric material, charge polarization is induced in response to both electric fields and strain (Eq. (2.1a)), and conversely stress is generated in response to both strain and electric fields (Eq. (2.1b)). The strain is related to the local deformation field $\mathbf{u}(\mathbf{x}, t)$ in the crystal via

$$S_{ij} = \frac{1}{2} (\partial_j u_i + \partial_i u_j). \quad (2.2)$$

In general, the piezoelectric systems that we will be concerned with are far smaller than the wavelength of electromagnetic waves at the frequencies of interest (GHz). We can therefore assume that the electromagnetic fields are quasi-static, i.e. $\mathbf{E} = -\nabla\phi$ for some scalar potential ϕ . To derive an

equation of motion for $\mathbf{u}(\mathbf{x}, t)$, we begin by taking the divergence of Eq. (2.1b),

$$\partial_j T_{ij} = \partial_j c_{ijlm} S_{lm} - \partial_j e_{lij} E_l \quad (2.3a)$$

$$= \frac{1}{2} \partial_j c_{ijlm} \partial_m u_l + \frac{1}{2} \partial_j c_{ijlm} \partial_l u_m - \partial_j e_{lij} E_l \quad (2.3b)$$

$$= \partial_j c_{ijlm} \partial_m u_l + \partial_j e_{lij} \partial_l \phi \quad (2.3c)$$

$$= \rho \partial_t^2 u_i. \quad (2.3d)$$

Here we used the symmetry $c_{ijlm} = c_{ijml}$ in the third line, and Newton's second law for a continuous solid, $\partial_j T_{ij} = \rho \partial_t^2 u_i$ [28]. Taking the divergence of Eq. (2.1a) and using $\partial_i D_i = 0$ (since there are no free charges in the crystal), we obtain

$$\partial_i D_i = \partial_i \epsilon_{ij} E_j + \partial_i e_{ijk} S_{jk} \quad (2.4a)$$

$$= \partial_i \epsilon_{ij} E_j + \partial_i e_{ijk} \partial_k u_j \quad (2.4b)$$

$$= 0. \quad (2.4c)$$

We now Fourier transform the fields as follows:

$$u_i(\mathbf{x}) = \frac{1}{(2\pi)^{3/2}} \int d^3 \mathbf{k} e^{i\mathbf{k}\cdot\mathbf{x}} u_i(\mathbf{k}), \quad (2.5a)$$

$$\phi(\mathbf{x}) = \frac{1}{(2\pi)^{3/2}} \int d^3 \mathbf{k} e^{i\mathbf{k}\cdot\mathbf{x}} \phi(\mathbf{k}). \quad (2.5b)$$

This transforms the preceding equations to

$$\rho \partial_t^2 u_i(\mathbf{k}) = -k^2 [\bar{c}_{il} u_l(\mathbf{k}) + \bar{e}_i \phi(\mathbf{k})] \quad (2.6a)$$

$$\bar{\epsilon} \phi(\mathbf{k}) = \bar{e}_i u_i(\mathbf{k}), \quad (2.6b)$$

where we have defined the projections

$$\bar{c}_{il} = \hat{k}_j c_{jilm} \hat{k}_m \quad (2.7a)$$

$$\bar{e}_i = \hat{k}_l e_{lij} \hat{k}_j, \quad (2.7b)$$

$$\bar{\epsilon} = \hat{k}_i \epsilon_{ijk} \hat{k}_j \quad (2.7c)$$

with $\hat{k} := \mathbf{k}/k$. Combining Eqs. (2.6a, 2.6b), we finally obtain

$$\rho \partial_t^2 u_i(\mathbf{k}) = -k^2 \bar{d}_{il} u_l(\mathbf{k}), \quad (2.8)$$

where $\bar{d}_{il} = \bar{c}_{il} + \bar{e}_i \bar{e}_l / \bar{\epsilon}$ is a modified stiffness tensor. For most materials, d and c are very similar — the effect of piezoelectricity on the elastic properties is small, manifesting primarily as a slight

‘stiffening’ of the material¹.

The symmetries of c and e are passed on to \bar{d} , so that it too is symmetric under the exchange of the i and l indices. Therefore there is a basis $\{\hat{g}_i\}_{i=1}^3$ in which \bar{d} is diagonal [67]. Writing \mathbf{u} in this basis yields solutions of Eq. (2.8), of the form $u_j(\mathbf{k}) = A(\mathbf{k})e^{i\omega_j t} + B(\mathbf{k})e^{-i\omega_j t}$. They obey the dispersion relation $\omega_j = (d_j/\rho)^{1/2}k = v_j k$. Here j indexes the basis element. In other words, the wave speed v_j may in general depend on the direction of propagation due to the anisotropy of the crystal. Taking now the inverse Fourier transform of Eq. (2.8), we obtain for each of the principal axes of \bar{d} a real-space equation

$$\rho \partial_t^2 u_i(\mathbf{x}) = L u_i(\mathbf{x}), \quad (2.9)$$

where L is a self-adjoint differential operator.

Because L is self-adjoint, the solutions of this equation can be expanded in terms of a complete set of orthogonal functions $\{\mathbf{U}_n(\mathbf{x})\}$ as

$$\mathbf{u}(\mathbf{x}, t) = \sum_n (b_n \mathbf{U}_n(\mathbf{x}) e^{-i\Omega_n t} + b_n^* \mathbf{U}_n^*(\mathbf{x}) e^{i\Omega_n t}), \quad (2.10)$$

where $\{b_n\}$ is a set of complex expansion coefficients and n is a generic label for the modes. Substituting this into Eq. (2.9), we obtain the eigenvalue equation

$$-\rho \Omega_n^2 \mathbf{U}_n(\mathbf{x}) = L \mathbf{U}_n(\mathbf{x}), \quad (2.11)$$

which can then be solved to find the eigenfunctions $\{\mathbf{U}_n\}$ (a.k.a. mode functions, or mode profiles) given a set of boundary conditions.

2.1.2 Quantization

From here it is straightforward to quantize the modes by promoting the coefficients $\{b_n\}$ in Eq. (2.10) (and the deformation \mathbf{u}) to operators:

$$\hat{\mathbf{u}}(\mathbf{x}, t) = \sum_n (\hat{b}_n \mathbf{U}_n(\mathbf{x}) e^{-i\Omega_n t} + \hat{b}_n^\dagger \mathbf{U}_n^*(\mathbf{x}) e^{i\Omega_n t}). \quad (2.12)$$

The operators $\hat{b}_n^\dagger, \hat{b}_n$ create and destroy phonons in each mode, respectively. In order to get the correct phonon energies $\hbar\Omega_n$, the mode functions are normalized [108] so as to satisfy

$$x_{\text{zp}, n} = \sqrt{\frac{\hbar}{2m_{\text{eff}, n}\Omega_n}} := \max_{\mathbf{x}} [\|\mathbf{U}_n(\mathbf{x})\|], \quad (2.13)$$

¹A notable exception to this is of course lithium niobate, where the electromechanical coupling constant (a dimensionless measure of the difference between d and c) can be as large as $\sim 15\%$, depending on the mode in question.

where $x_{\text{zp},n}$ is the zero-point fluctuation amplitude for mode n . The effective mass of the mode is defined as

$$m_{\text{eff},n} = \frac{\int d^3\mathbf{x} \mathbf{U}_n^*(\mathbf{x}) \rho(\mathbf{x}) \mathbf{U}_n(\mathbf{x})}{\max [|\mathbf{U}_n(\mathbf{x})|^2]}. \quad (2.14)$$

All of this may seem a little abstract at this point, but this framework will come to life later in Section 2.3, where I analyze the coupling between these waves and an external circuit.

2.2 Superconducting circuits

Let us now turn our attention to superconducting circuits. This section is meant to provide the essential background needed to understand the main results in later chapters, making the assumption that the reader has a basic familiarity with the mathematical treatment of superconducting circuits. There are a number of very good introductory texts available on this topic, most notably Refs. [37, 46]. Nevertheless, in an attempt to make this reading self-contained I will begin with a very brief review of the basic framework and terminology.

2.2.1 Classical circuit theory and quantization

Any circuit, whether superconducting or not, can be described using either a Lagrangian or Hamiltonian formalism. It is useful to think of an arbitrary circuit as a planar graph, where each node represents a wire or an ‘island’ and each edge represents a circuit element, such as a capacitor or an inductor. To keep things simple we will only be concerned with *lossless* elements in this discussion. This will be sufficient to convey the basic physics.

To begin, we select an arbitrary node of the circuit as the ‘ground’ node. Every other node k can now be described by a generalized coordinate called the ‘node flux’, defined in terms of the node voltage V_k (relative to ground) as follows:

$$\Phi_k(t) = \int_{-\infty}^t dt' V_k(t'). \quad (2.15)$$

From this definition it follows that $\dot{\Phi}_k = V_k$.

Let us consider the canonical example of an LC circuit, shown in Fig. 2.1. First, we notice that the energy stored in the capacitor is $T = C\dot{\Phi}^2/2$. On the other hand the voltage across the inductor is $V = L\dot{I} = \dot{\Phi}$, from which we immediately see that Φ corresponds to the magnetic flux (up to a constant)². The energy stored in the inductor is therefore $U = \Phi^2/2L$. Putting these two terms together, we can then write down a Lagrangian for this circuit in terms of the Φ coordinate and the

²In superconducting circuits Φ has in fact a much more general interpretation, for example also playing the role of the phase coordinate ϕ that describes a Josephson junction. This phase is related to the node flux via $\phi = \Phi/\Phi_0$, where $\Phi_0 = \hbar/2e$ is the reduced flux quantum. This will become evident when we discuss Josephson junctions later on.

'velocity' $\dot{\Phi}$:

$$L = T - U \quad (2.16a)$$

$$= \frac{1}{2}C\dot{\Phi}^2 - \frac{1}{2L}\Phi^2. \quad (2.16b)$$

The momentum conjugate of Φ is $\partial_{\dot{\Phi}}L = C\dot{\Phi} \equiv Q$ and is called the node charge. To find the Hamiltonian, we can follow the standard procedure and take the Legendre transform of Eq. (2.16b):

$$H = Q\dot{\Phi} - L \quad (2.17a)$$

$$= \frac{Q^2}{2C} + \frac{\Phi^2}{2L}. \quad (2.17b)$$

This should now look very familiar: it is just the total energy stored among both of the circuit elements. Moreover H is identical to a harmonic oscillator Hamiltonian, with Φ and Q playing the role of position and momentum, respectively.

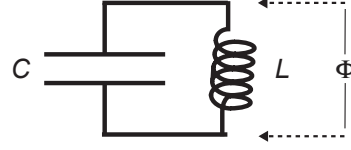


Figure 2.1: Sketch of LC resonator.

To quantize the circuit, we just 'put hats' on all observables \hat{H} , $\hat{\Phi}$, and \hat{Q} , with $\hat{\Phi}$ and \hat{Q} obeying the canonical commutation relation

$$[\hat{\Phi}, \hat{Q}] = i\hbar. \quad (2.18)$$

We can also diagonalize \hat{H} by defining ladder operators \hat{a} , \hat{a}^\dagger in the usual way,

$$\hat{a} = i\frac{1}{\sqrt{2\hbar\omega C}}\hat{Q} + \frac{1}{\sqrt{2\hbar\omega L}}\hat{\Phi}, \quad (2.19a)$$

$$\hat{a}^\dagger = -i\frac{1}{\sqrt{2\hbar\omega C}}\hat{Q} + \frac{1}{\sqrt{2\hbar\omega L}}\hat{\Phi}, \quad (2.19b)$$

with $\omega = (LC)^{-1/2}$. Then indeed $\hat{H} = \hbar\omega(\hat{a}^\dagger\hat{a} + 1/2)$.

This can be readily generalized to arbitrarily complicated circuits as follows:

$$L = \frac{1}{2}\dot{\Phi}_i C_{ij} \dot{\Phi}_j - \frac{1}{2}\Phi_i L_{ij}^{-1} \Phi_j, \quad (2.20a)$$

$$\implies H = \frac{1}{2}Q_i C_{ij}^{-1} Q_j + \frac{1}{2}\Phi_i L_{ij}^{-1} \Phi_j \quad (2.20b)$$

where L and C are now inductance and capacitance matrices, respectively, and the $\{\Phi_i\}$ are the degrees of freedom corresponding to each dynamic node³. Any circuit in which C and L are diagonal is already very simple: the degrees of freedom are all decoupled and oscillate at frequencies $\omega_i = (L_i C_i)^{-1/2}$, where $\{C_i\}$ and $\{L_i\}$ are the diagonal entries of the matrices. Sometimes a circuit may look deceptively complicated, but in fact it can be made diagonal with a simple redefinition of the degrees of freedom — we will see a concrete example of this in Section 2.2.3 when we discuss junction arrays. Other times, the diagonalization procedure must be done systematically, either by diagonalizing the Lagrangian or the Hamiltonian [46]. And finally, there are cases in which we are interested in the non-diagonal Hamiltonian and the coupling rate between degrees of freedom, as will be the case in Chapter 3.

2.2.2 Josephson junctions

So far, all of the circuit elements that we have discussed are linear. Indeed, the diagonalization procedures outlined above are sufficient to decompose any arbitrary network of capacitors and inductors into a set of harmonic oscillators.

To display any sort of nontrivial quantum behavior, a circuit must possess a strong *nonlinearity* [37]. The simplest nonlinear element that can be used in superconducting circuits is the Josephson junction⁴. A junction is composed of two superconducting islands separated by a very thin insulating barrier. This barrier can be an oxide, a normal metal, a semiconductor, etc. In all of the works in this dissertation we use aluminum/aluminum oxide/aluminum junctions, which belong to the first category.

The goal now is to model the junction as a circuit element, i.e. to include the relevant terms in the Lagrangian that correctly describe its behavior. Whereas a ‘proper’ analysis would require the use of BCS theory [122], for our purpose it is sufficient to consider only a phenomenological model, taken directly from S. Girvin’s Les Houches course [46].

We begin by making the assumption that the ground state $|N\rangle$ of the electron gas on an individual island can be uniquely labeled by the number of Cooper pairs on the island⁵, N . Correspondingly, the state of two islands is labeled by two numbers $N_{L(R)}$, the number of Cooper pairs on the left (right) island at any given time. We can alternatively write these numbers as $N_L^{(i)} - m$ and $N_R^{(i)} + m$, where $N_{L(R)}^{(i)}$ are the numbers at some arbitrarily defined initial time and m is the number of Cooper pairs that have tunneled across the junction. In this way, we can concisely write the state of the junction as $|m\rangle$. We can now model the tunneling process with the phenomenological tight-binding Hamiltonian

$$\hat{H}_T = -\frac{1}{2}E_J \sum_m (|m\rangle\langle m+1| + |m+1\rangle\langle m|). \quad (2.21)$$

³The term ‘dynamic node’ is sometimes used to refer to any node of the circuit that is not ground.

⁴For brevity we will just call these ‘junctions’ from now on.

⁵This can of course be rigorously justified with BCS theory.

Here E_J is called the *Josephson energy* and parametrizes the rate at which Cooper pairs tunnel back and forth. The eigenstates of \hat{H}_T are the ‘plane wave’ states

$$|\phi\rangle = \sum_{m=-\infty}^{\infty} e^{im\phi}|m\rangle. \quad (2.22)$$

Indeed, it is easy to verify that

$$\hat{H}_T|\phi\rangle = -E_J \cos \phi |\phi\rangle. \quad (2.23)$$

Two interesting properties follow.

First, if we define an operator \hat{n} that counts the (integer) number of Cooper pairs that have tunneled across as $\hat{n} = \sum_m m|m\rangle\langle m|$, the *current* operator is

$$\hat{I} = 2e \frac{d\hat{n}}{dt} = -2e \frac{1}{i\hbar} [\hat{H}_T, \hat{n}] = \frac{e}{i\hbar} E_J \sum_m (|m\rangle\langle m+1| - |m+1\rangle\langle m|), \quad (2.24)$$

from which it follows that

$$\hat{I}|\phi\rangle = I_C \sin \phi |\phi\rangle. \quad (2.25)$$

In other words, the current $I(\phi) = I_C \sin \phi$ is a sinusoidal function of ϕ . Here $I_C = E_J/\Phi_0$ is called the *critical current*, and it is the largest current of coherently tunneling Cooper pairs that can be supported by the junction. Moreover, it is easy to check that

$$\hat{n}|\phi\rangle = -i \frac{d}{d\phi} |\phi\rangle, \quad (2.26)$$

so the charge operator \hat{n} behaves as the generator of translations in ϕ space, i.e. the momentum conjugate of ϕ . In fact,

$$[\hat{\phi}, \hat{n}] = i, \quad (2.27)$$

although it is technically not correct to talk about an operator $\hat{\phi}$, because the states $|\phi\rangle$ and $|\phi + 2\pi\rangle$ are identical⁶ (from which it follows that the wavefunction $\psi(\phi)$ must obey the boundary condition

⁶To see why this is the case, we use the fact that \hat{n} generates translations in ϕ to calculate

$$|\phi + 2\pi\rangle = e^{i(2\pi)\hat{n}} |\phi\rangle \quad (2.28a)$$

$$= e^{i(2\pi)\hat{n}} \sum_{m=-\infty}^{\infty} e^{im\phi} |m\rangle \quad (2.28b)$$

$$= \sum_{m=-\infty}^{\infty} e^{im(\phi+2\pi)} |m\rangle \quad (2.28c)$$

$$= \sum_{m=-\infty}^{\infty} e^{i(2\pi)m} e^{im\phi} |m\rangle \quad (2.28d)$$

$$= |\phi\rangle. \quad (2.28e)$$

The crucial step is in the second to last line, where we use the fact that the eigenvalues of \hat{n} are integers $m \in \mathbb{Z}$.

$\psi(\phi + 2\pi) = \psi(\phi)$. We will nevertheless keep using the cleaner notation $\hat{\phi}$, keeping in mind that only functions of $\hat{\phi}$ that respect this symmetry — such as $\cos \hat{\phi}$ — are well-defined operators. This will be important when we discuss transmon qubits in Section 2.2.4.

Second, let us imagine that we connect a voltage source to the junction so as to maintain a fixed voltage drop V across it. With this addition the Hamiltonian of the junction is now

$$\hat{H} = \hat{H}_T - 2eV\hat{n}, \quad (2.29)$$

from which we obtain the time evolution of the phase variable:

$$\frac{d\hat{\phi}}{dt} = \frac{1}{i\hbar} [\hat{H}, \hat{\phi}] = 2eV/\hbar. \quad (2.30)$$

In other words $V = \partial_t \hat{\phi}/\Phi_0$, where $\Phi_0 = \hbar/2e$ is the reduced flux quantum⁷. As promised, this clarifies the connection between the node flux introduced in the beginning of this section and the phase coordinate that we use to describe junctions. However, the fact that ϕ corresponds to the phase difference of the superconducting order parameter is not immediately clear from this analysis, although I will admittedly say that I have a loose grasp on the theory of superconductivity.

Superconducting quantum interference devices (SQUIDs)

As is clear from the discussion above, even a single junction displays interesting physics and, as we will see in later sections, is also an extremely useful nonlinear circuit element. However, an even more useful device is what is called a superconducting quantum interference device (or SQUID), which consists of two junctions arranged in a parallel configuration. This configuration is useful because it allows us to tune the effective Josephson energy of the whole SQUID by threading the SQUID loop with an externally applied magnetic flux, Φ_e . To see why this is the case, consider the following hand-wavy argument. Suppose the phase difference between either side of the SQUID is ϕ . If we take a Cooper pair around the loop once, the total phase it accumulates is $\delta\phi = \phi - \phi = 0 \bmod 2\pi$. However, in the presence of a magnetic field the total accumulated phase is really

$$\delta\phi = \frac{2e}{\hbar} \oint d\mathbf{s} \cdot \mathbf{A} = \Phi_e/\Phi_0, \quad (2.31)$$

where \mathbf{A} is the vector potential. Another way of writing this accumulated phase is

$$\delta\phi = (\phi + \Phi_e/2\Phi_0) - (\phi - \Phi_e/2\Phi_0), \quad (2.32)$$

⁷Most texts define $\Phi = h/2e$ (the regular flux quantum) but here I adopt a contrarian — and more convenient — notation.

which strongly suggests that the phase differences across each of the individual junctions correspond to each of the two terms above. If the junctions have the same Josephson energy E_J , the Hamiltonian for the SQUID must then be

$$H_{\text{SQUID}} = -E_J \cos \left(\phi + \frac{\Phi_e}{2\Phi_0} \right) - E_J \cos \left(\phi - \frac{\Phi_e}{2\Phi_0} \right) \quad (2.33\text{a})$$

$$= -E_{J,\Sigma} \cos \left(\frac{\Phi_e}{2\Phi_0} \right) \cos \phi \quad (2.33\text{b})$$

$$= -E_J(\Phi_e) \cos \phi, \quad (2.33\text{c})$$

where $E_J(\Phi_e) = E_{J,\Sigma} \cos(\Phi_e/2\Phi_0)$ and $E_{J,\Sigma} = 2E_J$ is the total Josephson energy of both junctions. The SQUID therefore behaves like a single junction with a tunable tunneling rate $E_J(\Phi_e)$, or ‘transparency’⁸. In the case where the junctions have different Josephson energies $E_{J,1}$, $E_{J,2}$, this generalizes to [60]

$$E_J(\Phi_e) = E_{J,\Sigma} \cos \left(\frac{\Phi_e}{2\Phi_0} \right) \sqrt{1 + \delta^2 \tan^2 \left(\frac{\Phi_e}{2\Phi_0} \right)}, \quad (2.34)$$

where $E_{J,\Sigma} := E_{J,1} + E_{J,2}$ and $\delta := (E_{J,1} - E_{J,2})/(E_{J,1} + E_{J,2})$ is a measure of the junction asymmetry.

2.2.3 SQUID array resonators

Let us now turn to the specific example of a SQUID array resonator, a type of circuit that will be of interest later on in Chapter 4 because it turns out to be a very good probe of nanomechanical motion. This is because, despite their tiny size, piezoelectric nanostructures can strongly couple to a resonant microwave field provided the field’s zero-point fluctuations are large enough. In practice, this amounts to confining the electric field to a very small volume, a task that can be accomplished with a circuit that has a very high impedance.

To an expert in the field an obvious choice might be a fluxonium qubit [75, 74]. However, the fluxonium is nonlinear at the single photon level and is therefore much more difficult to measure and manipulate than linear resonators than can be probed with a large number of photons. For an initial round of measurements of phononic crystal devices at low temperatures, we ideally require a tunable, high impedance microwave resonator with a large dynamic range. Being able to tune its frequency is a critical requirement, because initially we do not expect to have precise control over the frequencies of the nanostructures. Having the ability to tune the resonator across a wide frequency band makes searching for mechanical modes much more tractable.

The obvious choice that meets all of these requirements is a SQUID array resonator, such as the one reported in Refs. [77], [41], and [115].

⁸Readers may notice the clear similarity between SQUID physics and the Aharonov–Bohm effect.

Low energy model

Consider the circuit shown in Fig. 2.2, composed of a chain of N SQUIDs shunted by a capacitance C_r . We will assume all SQUIDS are identical, ignoring the effects of disorder. The Lagrangian for the circuit is

$$L = \frac{1}{2}C_r(\dot{\phi}_0 - \dot{\phi}_N)^2 - \sum_{i=0}^{N-1} E_J^{(1)}(\Phi_e) \cos(\phi_i - \phi_{i+1}). \quad (2.35)$$

Here we have introduced the notation $E_J^{(1)}(\Phi_e)$ for the (tunable) Josephson energy of a single SQUID, given by Eq. (2.34). The coordinates that we are using in this Lagrangian are the dimensionless node fluxes $\phi_i = \int dt' V_i(t')/\Phi_0$, so we write $C_r := C_r \Phi_0^2$ in order to get the right units.

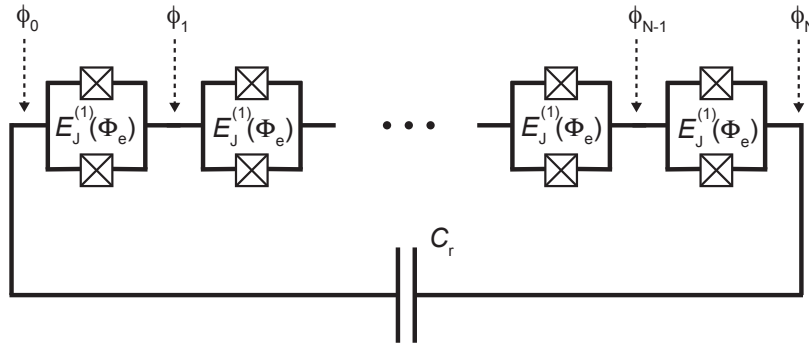


Figure 2.2: Sketch of SQUID array resonator.

We will now make a major simplifying assumption. We will assume that the phase difference between any two consecutive nodes in the array, $\phi_i - \phi_{i+1} := \Delta\phi_i$, is the same for all i . Defining $\Delta\phi_i = \Delta\phi \forall i$, then

$$\phi_0 - \phi_N = (\phi_0 - \phi_1) + (\phi_1 - \phi_2) + \cdots + (\phi_{N-1} - \phi_N) \quad (2.36a)$$

$$= \Delta\phi_0 + \cdots + \Delta\phi_{N-1} \quad (2.36b)$$

$$= N\Delta\phi, \quad (2.36c)$$

and

$$L = \frac{1}{2}N^2C_r\dot{\phi}^2 - E_J^{(1)}(\Phi_e) \sum_i \cos \Delta\phi_i \quad (2.37a)$$

$$= \frac{1}{2}N^2C_r\dot{\phi}^2 - E_J^{(1)}(\Phi_e) \sum_i \cos \Delta\phi \quad (2.37b)$$

$$= \frac{1}{2}N^2C_r\dot{\phi}^2 - NE_J^{(1)}(\Phi_e) \cos \Delta\phi. \quad (2.37c)$$

Finally, letting $\phi := N\Delta\phi$ (the total phase change across the array), the Lagrangian becomes

$$L = \frac{1}{2}\mathcal{C}_r\dot{\phi}^2 - NE_J^{(1)}(\Phi_e)\cos(\phi/N). \quad (2.38)$$

This Lagrangian describes the low energy behavior of the circuit, where the phase differences between nearest neighbors in the array all move in synchrony with each other. This means that the array has no internal dynamics, behaving collectively as a single SQUID.

Anharmonicity

If the entire array behaves as a single SQUID (i.e. it has a single degree of freedom), one might wonder why we would use an array at all. The answer lies in the argument of the cosine in Eq. (2.38). In contrast to a single SQUID, where the argument is ϕ , here the argument is ϕ/N because the total phase drop across the array is divided evenly among N SQUIDs. This effectively ‘dilutes’ the nonlinearity of the array and therefore increases its dynamic range (the mean number of photons it can support while still behaving more or less linearly). To see why, we first write the Hamiltonian

$$H = \pi\dot{\phi} - L \quad (2.39a)$$

$$= \frac{1}{2\mathcal{C}_r}\pi^2 - NE_J^{(1)}(\Phi_e)\cos(\phi/N) \quad (2.39b)$$

$$= 4E_C n^2 - NE_J^{(1)}(\Phi_e)\cos(\phi/N), \quad (2.39c)$$

where $\pi = \partial_{\dot{\phi}}L = \mathcal{C}_r\dot{\phi}$ is the canonical momentum (the charge on the capacitor), $E_C = e^2/2C_r$ is the charging energy, and $n = \pi/2e$ is the dimensionless charge. We now assume that $\phi/N \ll 1$. Crudely this assumption can be justified by first noticing that the Hamiltonian in Eq. (2.39c) is the same Hamiltonian of a pendulum with angular coordinate ϕ/N . If the circuit parameters satisfy $\max_{\Phi_e}[E_J^{(1)}(\Phi_e)/NE_C] \gg 1$ (which they usually do), this is analogous to a very ‘light’ pendulum in a strong gravitational field. In such a regime, unless the pendulum is kicked very hard, the pendulum’s angular fluctuations should remain small, i.e. $\phi/N \ll 1$. We will justify this logic more rigorously in Section 2.2.4 when we discuss transmon qubits. With this assumption we can now expand the cosine to quartic order,

$$H = \left(4E_C n^2 + \frac{E_J^{(1)}(\Phi_e)}{2N}\phi^2\right) - \frac{E_J^{(1)}(\Phi_e)}{24N^3}\phi^4 + \mathcal{O}((\phi/N)^6) \quad (2.40a)$$

$$\approx \left(4E_C n^2 + E_J^{(N)}(\Phi_e)\frac{\phi^2}{2}\right) - \frac{E_J^{(N)}(\Phi_e)}{24N^2}\phi^4 \quad (2.40b)$$

$$\equiv H_0 + V, \quad (2.40c)$$

where in the second line we defined $E_J^{(N)}(\Phi_e) := E_J^{(1)}(\Phi_e)/N$, the effective Josephson energy of the array. We now quantize the Hamiltonian as usual by promoting dynamical variables to operators ($n \rightarrow \hat{n}$, $\phi \rightarrow \hat{\phi}$) and defining ladder operators \hat{a} , \hat{a}^\dagger through

$$\hat{n} = i n_{\text{zp}} (\hat{a}^\dagger - \hat{a}) \quad (2.41\text{a})$$

$$\hat{\phi} = \phi_{\text{zp}} (\hat{a} + \hat{a}^\dagger), \quad (2.41\text{b})$$

where $n_{\text{zp}} = (E_J^{(N)}(\Phi_e)/2E_C)^{1/4}/2$ and $\phi_{\text{zp}} = (2E_C/E_J^{(N)}(\Phi_e))^{1/4}$. Indeed now we see that if $\max_{\Phi_e}[E_J^{(1)}(\Phi_e)/NE_C] \gg 1$, $\phi_{\text{zp}} \ll 1$ so our assumption that the phase fluctuations are small is at least self-consistent. In terms of these operators the linear part \hat{H}_0 of the Hamiltonian becomes

$$\hat{H}_0 = \hbar\omega_r(\Phi_e)(\hat{a}^\dagger \hat{a} + 1/2), \quad (2.42)$$

where $\hbar\omega_r(\Phi_e) = \sqrt{8|E_C E_J^{(N)}(\Phi_e)|}$ is the resonator frequency. Also in terms of these operators, the *nonlinear* part \hat{V} is

$$\hat{V} = -\frac{E_J^{(1)}(\Phi_e)}{24N^3} \hat{\phi}^4 \quad (2.43\text{a})$$

$$= -\frac{E_J^{(N)}(\Phi_e)}{24N^2} \left(\frac{2E_C}{E_J^{(N)}(\Phi_e)} \right) (\hat{a} + \hat{a}^\dagger)^4 \quad (2.43\text{b})$$

$$= -\frac{E_C}{12N^2} (\hat{a} + \hat{a}^\dagger)^4. \quad (2.43\text{c})$$

Finally, expanding the term $(\hat{a} + \hat{a}^\dagger)^4$ and dropping all terms that do not preserve photon number (such as $\hat{a}^3 \hat{a}^\dagger$), we get

$$\hat{V} = \frac{\hbar\chi}{2} \hat{a}^\dagger \hat{a} \hat{a}^\dagger \hat{a} + \frac{\hbar\chi}{6} \hat{a}^\dagger \hat{a} + \text{const.} \quad (2.44)$$

where $\hbar\chi := -E_C/N^2$. Finally, the total Hamiltonian is

$$\hat{H}/\hbar = \tilde{\omega}_r \hat{a}^\dagger \hat{a} + \frac{\chi}{2} \hat{a}^\dagger \hat{a} \hat{a}^\dagger \hat{a}, \quad (2.45)$$

where $\tilde{\omega}_r := \omega_r + \chi/6$ is the renormalized resonator frequency. It is clear that such a Hamiltonian differs from that of a linear resonator, because for every photon that gets added to the vacuum the resonator frequency shifts by an amount $\chi/2$. In some cases this shift can be much larger than the resonator linewidth, in which case the resonator is effectively a qubit because driving it with narrowband signals cannot take it out of the single excitation manifold. In other cases, the shift can be much smaller, in which case the resonator behaves linearly up to a certain number of photons. Here we are interested in the latter case.

It should also now be clear that the anharmonicity χ is a factor of N^2 smaller than it would be for an array consisting of a single SQUID (which, as we will see later, is the same thing as

a charge qubit). This is a very strong suppression factor, and is exactly what we need in order to increase the dynamic range of the resonator. For example, a transmon qubit typically has an anharmonicity $\chi = E_C/h \sim 200$ MHz; all else the same, a SQUID array resonator with $N = 20$ would have $\chi \sim 0.5$ MHz.

In order to derive scattering parameters in what will follow, it is more convenient to rewrite the Hamiltonian using the normal-ordered version of the expansion of $(\hat{a} + \hat{a}^\dagger)^4$. It is easy to show that

$$\hat{H}/\hbar = \tilde{\omega}_r \hat{a}^\dagger \hat{a} + \frac{\chi}{2} (\hat{a}^\dagger)^2 (\hat{a})^2, \quad (2.46)$$

with $\tilde{\omega}_r = \omega_r + \chi/2$.

Flux tuning and junction asymmetry

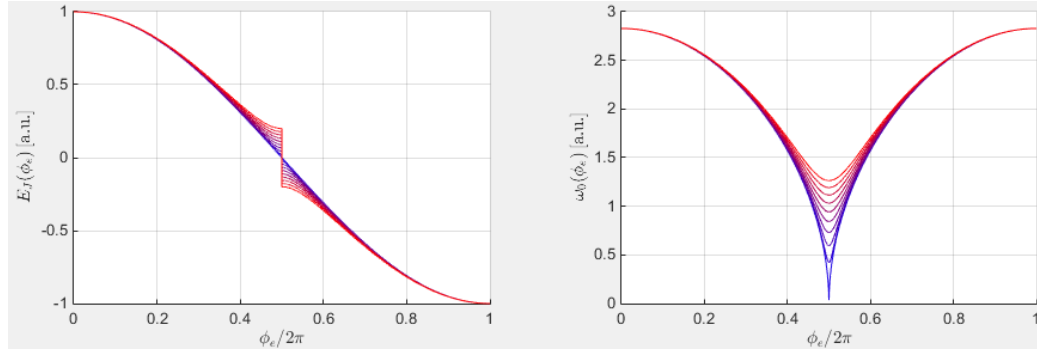


Figure 2.3: Dependence of $E_J^{(N)}$ (left) and ω_r (right) on Φ_e . Different values of δ are shown in different colors, with blue corresponding to $\delta = 0$.

If the SQUIDs are symmetric ($\delta = 0$), it is clear from Eq. (2.34) that tuning Φ_e across the range $\Phi_e \in [0, 2\pi\Phi_0]$ tunes array's effective tunneling energy across the range $E_J^{(N)}(\Phi_e) \in [-E_J^{(N)}, E_J^{(N)}]$. The resonator frequency is therefore tuned from its maximum value $\omega_{r,\max} = \sqrt{8E_C E_J^{(N)}}/\hbar$ down to 0, and back to the maximum.

The effect of finite junction asymmetry ($\delta \neq 0$) is simply to reduce the effective tuning range and smooth out the singularity in the flux susceptibility $\partial\omega_r/\partial\Phi_e$ that occurs at the half-flux-quantum bias point $\Phi_e = \Phi_0/2$. See Fig. 2.3 for a plot of $E_J^{(N)}$ and $\omega_r(\Phi_e)$.

Scattering parameters

Now that we have a basic model the resonator, how do we probe it? The easiest way is to capacitively couple it to a transmission line (also called a feedline, or waveguide) so that its resonance appears in a one-port reflection measurement. For now we can abstract away the circuitry and just use a

simple input-output model [45] — see Fig. 2.4. This will be a simple illustration that should serve as a basis for the slightly more complicated model of Chapter 4, which will additionally include the coupling of the circuit to mechanical resonances.

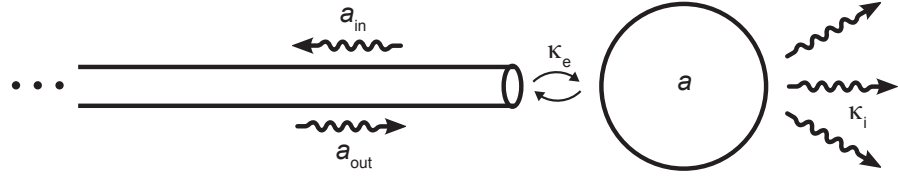


Figure 2.4: Input-output model for SQUID array resonator probed on reflection.

The full Hamiltonian including driving terms is now $\hat{H} = \hat{H}_0 + \hat{V} + \hat{H}_\kappa + \hat{H}_d(t)$, where

$$\hat{H}_d(t) = i\sqrt{\kappa_e}(\hat{a}^\dagger \alpha_{in} e^{-i\omega_d t} - \hat{a} \alpha_{in}^* e^{+i\omega_d t}) \quad (2.47)$$

models the effect of a coherent drive applied to port (1) and \hat{H}_κ is a bath Hamiltonian (including its coupling to the resonator). Here κ_e is the coupling rate to the waveguide, and α_{in} and ω_d are the drive amplitude and frequency, respectively. We now go to an interaction frame rotating at frequency ω_d by transforming the Hamiltonian

$$\hat{H} \mapsto \hat{H}' = \hat{U}(t)\hat{H}\hat{U}^\dagger(t) + i\left(\frac{d\hat{U}}{dt}\right)\hat{U}^\dagger, \quad (2.48)$$

where $\hat{U}(t) = e^{i\omega_d \hat{a}^\dagger \hat{a} t}$. We obtain

$$\hat{H}'/\hbar = -\Delta \hat{a}^\dagger \hat{a} + \frac{\chi}{2}(\hat{a}^\dagger)^2 (\hat{a})^2 + i\sqrt{\kappa_e}(\alpha_{in} \hat{a}^\dagger - \alpha_{in}^* \hat{a}) + \hat{H}'_\kappa, \quad (2.49)$$

with $\Delta := \omega_d - \tilde{\omega}_r$. The Heisenberg equation of motion for the resonator field \hat{a} is then

$$\partial_t \hat{a} = -i[\hat{a}, \hat{H}/\hbar] \quad (2.50a)$$

$$= \left(i\Delta - \frac{\kappa}{2}\right) \hat{a} + i\chi \hat{a}^\dagger (\hat{a})^2 + \sqrt{\kappa_e}(\alpha_{in} + \hat{d}_{in}), \quad (2.50b)$$

where \hat{d}_{in} is a noise operator and $\kappa = \kappa_e + \kappa_i$ is the total linewidth of the resonator, including the intrinsic damping contribution κ_i due to coupling to bath modes that are not monitored. Note that I'm being fairly loose in the way I handle noise operators (for example I only included noise injected from the waveguide and not from any other bath). This does not matter here because in what follows we will only be concerned about the classical behavior of the circuit, where the mean photon number $|\alpha|^2$ is large compared to one.

In order to get an equation of motion for the classical field amplitude, we can write $\hat{a} = \alpha + \hat{d}$, where $\alpha \in \mathbb{C}$ is the amplitude of the classical field — generated by the coherent driving tone — that is superimposed on top of the fluctuations \hat{d} . Substituting this into Eq. (2.50b) and dropping terms that contain \hat{d} , we obtain

$$\dot{\alpha} = \left(i\Delta - \frac{\kappa}{2} \right) \alpha + i\chi|\alpha|^2\alpha + \sqrt{\kappa_e}\alpha_{\text{in}}. \quad (2.51)$$

It is also possible to derive a *linearized* equation of motion for the fluctuations \hat{d} , which is very important in the analysis of quantum limited parametric amplifiers — a great reference on this is Ref. [41].

If we now ignore the nonlinear term in Eq. (2.51), we can solve for the steady-state field by setting $\dot{\alpha} = 0$, resulting in

$$\alpha = \frac{\sqrt{\kappa_e}}{-i\Delta + \kappa/2}\alpha_{\text{in}}. \quad (2.52)$$

Together with the boundary condition relating the forward- and back-propagating fields in the waveguide $\alpha_{\text{out}} = -\alpha_{\text{in}} + \sqrt{\kappa_e}\alpha$ [45, 31], we finally arrive at an expression for the reflection coefficient $\Gamma(\omega)$ at the input port,

$$\Gamma(\omega) := \frac{\alpha_{\text{out}}}{\alpha_{\text{in}}} = -1 + \frac{\kappa_e}{-i\Delta + \kappa/2}. \quad (2.53)$$

This is nothing more than the linear response that we would observe in a reflection measurement through port (1). The full nonlinear response that results from keeping all terms in Eq. (2.51) is more complicated, so the reader is referred to Ref. [41] for a detailed analysis. It is indeed this nonlinearity that enables devices of this type to be used as amplifiers. For an excellent treatise on this topic the reader is referred to Ref. [20].

Dynamic range

The only place where nonlinearity will enter this discussion is in understanding the dynamic range. We define the dynamic range as the range of input powers for which the resonator response is linear. This is true as long as $|\chi|\bar{n} \ll \kappa$, where $\bar{n} = |\alpha|^2$ is the mean photon number in the resonator. We can express this condition in terms of the input power P_{in} at port (1) by noting that

$$P_{\text{in}} = \hbar\omega_d|\alpha_{\text{in}}|^2 \quad (2.54)$$

and

$$|\alpha|^2 = \frac{\kappa_e}{\Delta^2 + \kappa^2/4}|\alpha_{\text{in}}|^2 \leq \frac{4\kappa_e}{\kappa^2}|\alpha_{\text{in}}|^2 \leq \frac{4}{\kappa_e}|\alpha_{\text{in}}|^2. \quad (2.55)$$

In particular we expect $|\alpha|^2 \approx (4/\kappa_e)|\alpha_{\text{in}}|^2$ near the resonance of an overcoupled ($\kappa \approx \kappa_e$) resonator, so the dynamic range is given by

$$0 \leq P_{\text{in}} \ll \hbar\omega_r \frac{\kappa_e^2}{4\chi}. \quad (2.56)$$

Putting in generic numbers ($\omega_r = 2\pi \times 5 \text{ GHz}$, $\kappa_e = 2\pi \times 20 \text{ MHz}$, $\chi = 2\pi \times 2 \text{ MHz}$), we get a maximum power $P_{\text{in}} \approx -128 \text{ dBm}$, which is well within the range of what can be achieved in a dilution refrigerator using a VNA and a high electron mobility transistor (HEMT) amplifier.

Internal dynamics of the array

We remark that the crucial assumption made in the low energy model eliminates any possibility of modeling higher order resonances of the array, which occur at (usually) much larger frequencies than the ‘regular’ $(LC)^{-1/2}$ resonance of the circuit. This is an interesting topic in and of itself — for a detailed discussion the reader is referred to Refs. [77, 76]. It also does not model phase slip processes, an in-depth treatment of which can be found in Ref. [74].

2.2.4 Transmon qubits

Our tour of superconducting circuits has finally come to its last stop: transmon qubits [60]. Transmon qubits are a variation of a class of qubits called *charge qubits*, which bear their name because their energy eigenstates are *almost* the same as the eigenstates of the charge operator \hat{n} . Take, for example, an isolated capacitor. Its Hamiltonian is simply $\hat{H} = 4E_C\hat{n}^2$, where $E_C = e^2/2C$ is called the *charging energy* and it measures the cost in electrostatic energy associated with transferring a single electron from one side to the other. In this case, obviously the eigenstates of \hat{n} — called *charge states* — are also eigenstates of \hat{H} . Charge qubits however contain two pieces: in addition to a capacitance, there is also a Josephson junction that allows charges to tunnel across. The Hamiltonian is therefore

$$\hat{H} = 4E_C(\hat{n} - n_g)^2 - E_J \cos \hat{\phi}. \quad (2.57)$$

Here $n_g \in \mathbb{R}$ is called the *gate charge* and it models the effect of (continuous) charge offsets induced either by externally applied voltages, or random fluctuations in the electrostatic environment of the junction that make it seem as if the junction were being biased. With Cooper pairs now allowed to tunnel from one side of the capacitor to the other ($E_J > 0$), the charge states are no longer stationary. However, if $E_J/E_C \lesssim 1$ the energy cost of tunneling is high and the energy eigenstates remain well localized in the charge basis. Circuits in this regime are called *Cooper pair boxes* (CPBs) and were prevalent until the introduction of the transmon in 2007. Transmons operate in the opposite regime ($E_J/E_C \gg 1$) in order to eliminate their susceptibility to random fluctuations in the gate charge n_g . In this section I will discuss the basic physics of transmons, giving more or less an overview of Refs. [60, 46] and highlighting what I think are the aspects most relevant to the results from Chapter 5.

Energy eigenstates and eigenvalues

Before we discuss transmons, it will be useful to point out some general properties of the Hamiltonian of Eq. (2.57). The first property to take note of is that the eigenenergies of the Hamiltonian are periodic in the gate charge, with periodicity $n_g = 1$. This is because the spectrum of \hat{n} is \mathbb{Z} . More specifically, the unitary transformation $\hat{U} = \exp(\pm i\hat{\phi})$, which displaces the charge by one unit ($\hat{U}\hat{n}\hat{U}^\dagger = \hat{n} \mp 1$), preserves the $\hat{\phi} \rightarrow \hat{\phi} + 2\pi$ symmetry and also preserves the spectrum of \hat{H} because it simply ‘re-shuffles’ the eigenvalues. For example the energy eigenvalue associated with $\hat{n} = 0$ now corresponds to $\hat{n} \pm 1$, and so on.

The argument above also suggests that the spectrum of \hat{H} *does not* stay invariant if n_g is displaced by fractional steps. In fact, it turns out that the spectrum of \hat{H} consists of energy ‘bands’ that vary as n_g is swept from 0 to 1 (or equivalently from $-1/2$ to $+1/2$). To see this, let us first apply the transformation $\hat{U} = \exp(i\hat{\phi}n_g)$ to the Hamiltonian

$$\hat{H} \rightarrow \hat{H}' = \hat{U}\hat{H}\hat{U}^\dagger = 4E_C\hat{n}^2 - E_J \cos \hat{\phi}, \quad (2.58)$$

eliminating the offset charge. The transformed wavefunctions now have the following property:

$$\Psi'(\phi + 2\pi) = e^{i(2\pi)\hat{n}} e^{i\hat{\phi}n_g} \Psi(\phi) \quad (2.59a)$$

$$= e^{i(\hat{\phi}+2\pi)n_g} \Psi(\phi) \quad (2.59b)$$

$$= e^{i(2\pi)n_g} e^{i\hat{\phi}n_g} \Psi(\phi) \quad (2.59c)$$

$$= e^{i(2\pi)n_g} \Psi'(\phi). \quad (2.59d)$$

This should remind us of Bloch’s theorem. Indeed, the Hamiltonian of Eq. (2.58) is invariant under the discrete translation $\phi \rightarrow \phi + 2\pi$, and therefore its eigenfunctions must be of the form

$$\Psi_{m,k}(\phi) = e^{ik\phi} \psi_m(\phi), \quad (2.60)$$

where $\psi_m(\phi)$ is invariant under $\phi \rightarrow \phi + 2\pi$, m is a band index, and $k \in [-1/2, 1/2]$ is a wavevector in the first Brillouin zone. The transformed wavefunction Ψ' from above has exactly this property, with $k = n_g$. So we see that the offset charge n_g plays the role of the Bloch vector for the phase ‘particle’ moving along the periodic $\cos \phi$ potential.

This interesting link to Bloch functions comes with an inconvenient caveat. The fact that the eigenenergies of \hat{H} vary as a function of n_g means that the qubit transition frequencies fluctuate in response to noise in n_g , dephasing the qubit states.

In order to quantify this *charge dispersion* effect it is necessary to diagonalize \hat{H} exactly. This is quite involved and requires solving Shrödinger’s equation in a cosine potential with periodic boundary conditions. The resulting eigenfunctions are called Mathieu functions and are discussed

in depth in Ref. [60]. The relevant thing to know here is that the ‘peak-to-peak’ variation ϵ_m of any given energy band m turns out to be an exponentially decreasing function of the ratio E_J/E_C :

$$\epsilon_m \simeq (-1)^m E_C \frac{2^{4m+5}}{m!} \sqrt{\frac{2}{\pi}} \left(\frac{E_J}{2E_C} \right)^{\frac{m}{2} + \frac{3}{4}} e^{-\sqrt{8E_J/E_C}}. \quad (2.61)$$

In particular, this means that in the limit of $E_J/E_C \gg 1$, ϵ_m becomes vanishingly small and the energy bands become flat. This motivated the invention of the transmon — a CPB with a large capacitance connected in parallel and with a value chosen such that the circuit goes to the limit $E_J/E_C \gg 1$, virtually eliminating the contribution of charge noise to the dephasing rate. Even though solving the Hamiltonian exactly in the general case is complicated (as previously mentioned), luckily in the $E_J/E_C \gg 1$ regime we can solve it to a very good approximation with a simple argument. The argument is in fact a beefed up version of the one we used to calculate the anharmonicity of SQUID array resonators in Section 2.2.3, and proceeds as follows.

First we eliminate the gate charge from the Hamiltonian by applying the transformation of Eq. (2.58). In this new ‘frame’, the wavefunctions no longer obey periodic boundary conditions, as shown in Eq. (2.59). However, in the $E_J/E_C \gg 1$ limit the phase fluctuations are small (again, because this regime is analogous to a light pendulum in a strong gravitational field), meaning that the eigenfunctions $\Psi_m(\phi)$ of \hat{H} are tightly localized around the origin $\phi = 0$. This makes the wavefunctions insensitive to the boundary conditions and is the same reason why the spectrum of \hat{H} is unaffected by this ‘change of gauge’. Furthermore, if the wavefunctions are localized deep inside the cosine potential well and never see their neighboring wells, we can in fact do away with the discrete translational invariance of \hat{H} altogether and expand the $\cos \phi$ potential in a Taylor series around $\phi = 0$:

$$\hat{H} \approx 4E_C \hat{n}^2 - E_J + \frac{E_J}{2} \hat{\phi}^2 - \frac{E_J}{24} \hat{\phi}^4. \quad (2.62)$$

We can now solve this Hamiltonian in the same way we did for SQUID arrays in Section 2.2.3, writing the charge and phase operators in terms of ladder operators

$$\hat{n} = i n_{\text{zp}} (\hat{a}^\dagger - \hat{a}) \quad (2.63a)$$

$$\hat{\phi} = \phi_{\text{zp}} (\hat{a} + \hat{a}^\dagger) \quad (2.63b)$$

with $n_{\text{zp}} = (E_J/2E_C)^{1/4}/2$ and $\phi_{\text{zp}} = (2E_C/E_J)^{1/4}$. In terms of these operators, the Hamiltonian becomes

$$\hat{H} = \sqrt{8E_C E_J} \hat{a}^\dagger \hat{a} - \frac{E_C}{12} (\hat{a} + \hat{a}^\dagger)^4, \quad (2.64)$$

or expanding the quartic term, dropping photon non-conserving terms, and normal-ordering, we have

$$\hat{H} = (\sqrt{8E_C E_J}) \hat{a}^\dagger \hat{a} - \frac{E_C}{2} (\hat{a}^\dagger \hat{a}^\dagger \hat{a} \hat{a} + 2\hat{a}^\dagger \hat{a}). \quad (2.65)$$

Treating the last term as a perturbation, we can easily calculate the energy spectrum using first-order perturbation theory:

$$E_m \simeq -E_J + \sqrt{8E_C E_J} \left(m + \frac{1}{2} \right) - \frac{E_C}{12} (6m^2 + 6m + 3). \quad (2.66)$$

From this we can now read off the transition frequencies between the ground and excited states and the excited and second-excited states, ω_{ge} and ω_{ef} respectively:

$$\omega_{\text{ge}} = (\sqrt{8E_C E_J} - E_C)/\hbar \quad (2.67a)$$

$$\omega_{\text{ef}} = (\sqrt{8E_C E_J} - 2E_C)/\hbar. \quad (2.67b)$$

In particular, the difference between these two is the anharmonicity of the transmon, $\omega_{\text{ge}} - \omega_{\text{ef}} \equiv \alpha = E_C/\hbar$. One of the central questions addressed by the original transmon proposal (Ref. [60]) was whether this anharmonicity would remain sufficiently large in the transmon limit $E_J/E_C \gg 1$. The answer to this is yes. We can easily infer that the *relative* anharmonicity decreases as a weak power law in E_J/E_C :

$$\alpha_r \equiv \alpha/\omega_{\text{ge}} \simeq -(8E_J/E_C)^{-1/2}. \quad (2.68)$$

If we pick $E_J/E_C = 50$, which is sufficient to strongly suppress charge dispersion, the relative anharmonicity is still a whopping $\alpha_r = -5\%$. This amounts to $\sim 200 - 300$ MHz for typical transmons, equivalent to a timescale of a few nanoseconds. Any pulse that is used to address the qubit that is reasonably longer than this timescale will in principle keep the qubit inside of the computational subspace $\{|g\rangle, |e\rangle\}$. Still, today in an effort to push pulse lengths down to a few nanoseconds it is necessary to employ nontrivial pulse-shaping techniques.

Linear coupling to a resonator

The next aspect of transmon qubits that we will pay attention to is the mechanism through which they couple to a resonator. Understanding this is important because transmons are routinely coupled to microwave resonators for dispersive readout. Furthermore, the mathematical treatment of this type of coupling is identical to how we will analyze piezoelectric coupling to nanomechanical structures in Chapter 3.

Consider the circuit shown in Fig. 2.5, which consists of a transmon coupled to a lumped element resonator via a coupling capacitor C_g ⁹. Note that this is a minimal representation of the network that would exist on a real device, which would have more nodes, cross-capacitances, etc. However this minimal circuit is sufficient to capture the basic physics that we are interested in here.

⁹In practice we usually couple transmons to *distributed* transmission line resonators for readout. However it is always possible to ‘synthesize’ a lumped element version of the distributed device with the same properties. When the resonator is a piezoelectric mechanical system the same synthesis procedure is applicable, and this will be the point of focus in Chapter 3.

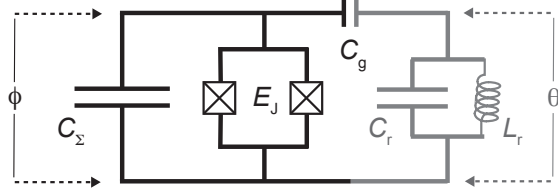


Figure 2.5: Sketch of transmon coupled to an LC resonator.

In terms of the dimensionless node fluxes labeled on Fig. 2.5, the Lagrangian for this circuit is

$$L = \frac{1}{2}C_g(\dot{\phi} - \dot{\theta})^2 + \frac{1}{2}C_r\dot{\theta}^2 + \frac{1}{2}C_\Sigma\dot{\phi}^2 + E_J \cos \phi - \frac{1}{2\mathcal{L}_r}\theta^2, \quad (2.69)$$

where again in order to have the right units we are using the notation $\mathcal{C}_i := C_i\Phi_0^2$ and $\mathcal{L}_i := L/\Phi_0^2$. From this point, arriving at a Hamiltonian is a simple derivation. This derivation is given in detail in Chapter A.1 so I will skip to the result¹⁰:

$$\hat{H} = 4E_C\hat{n}^2 - E_J \cos \hat{\phi} + \hbar\omega_r \hat{a}^\dagger \hat{a} + 2e\beta V_{zp}^{(r)} \hat{n}(\hat{a} + \hat{a}^\dagger). \quad (2.70)$$

Note that here I am adhering to a notation similar to J. Koch's in Ref. [60] rather than to my own notation in Chapter A.1. Here $V_{zp}^{(r)} = \sqrt{\hbar\omega_r/2C_r}$ are the zero-point voltage fluctuations of the resonator and $\beta = C_g/C_\Sigma$. Note that we can also write $V_{zp}^{(r)} = \omega_r \sqrt{\hbar Z_r/2}$ to make explicit the dependence of the voltage fluctuations on the resonator impedance $Z_r = \sqrt{L_r/C_r}$. We can now write \hat{H} in the basis of bare transmon eigenstates $\{|j\rangle\}$,

$$\hat{H}/\hbar = \sum_j \omega_j |j\rangle \langle j| + \omega_r \hat{a}^\dagger \hat{a} + \sum_{j,k} g_{jk} |j\rangle \langle k| (\hat{a} + \hat{a}^\dagger), \quad (2.71)$$

where $\{\hbar\omega_j\}$ are the transmon eigenenergies, and

$$g_{jk} = 2e\beta V_{zp}^{(r)} \langle j | \hat{n} | k \rangle \quad (2.72)$$

is the transition rate between the k and j transmon levels induced by the coupling to the resonator field. This last term in the Hamiltonian allows the resonator and transmon to exchange quanta when $\omega_r \approx |\omega_j - \omega_k|$ and $g_{jk} > 0$ for some pair of levels k and j . Using Eq. (2.63a) to calculate the matrix elements of the charge operator, it is easy to verify that in the transmon limit $E_J/E_C \gg 1$

¹⁰In order to simplify the final result here we are making an additional assumption that there is a hierarchy of capacitances, $C_r \gg C_\Sigma \gg C_g$. This assumption is generally valid when the resonator is a distributed transmission line resonator, but it is *not* when the resonator is a mechanical nanostructure. The general case, without making this assumption, is covered in Chapter A.1.

only certain transitions are allowed:

$$|\langle j+1|\hat{n}|j\rangle| \approx \sqrt{\frac{j+1}{2}} \left(\frac{E_J}{8E_C} \right)^{1/4} = \sqrt{j+1} n_{\text{zp}} \quad (2.73\text{a})$$

$$|\langle j+k|\hat{n}|j\rangle| \approx 0. \quad (2.73\text{b})$$

with $|k| > 1$. Only transitions between neighboring states are allowed, which is not surprising because the coupling to the resonator is a dipole-type coupling. With these selection rules the Hamiltonian simplifies to

$$\hat{H}/\hbar = \sum_j \omega_j |j\rangle\langle j| + \omega_r \hat{a}^\dagger \hat{a} + \sum_j g_{j,j+1} (|j\rangle\langle j+1|)(\hat{a} + \hat{a}^\dagger) + \text{h.c.} \quad (2.74)$$

The couplings can now be written in a nice way,

$$g_{j,j+1} = 2e\beta V_{\text{zp}}^{(\text{r})} |\langle j+1|\hat{n}|j\rangle| \quad (2.75\text{a})$$

$$= 2\sqrt{j+1} e(C_g/C_\Sigma) V_{\text{zp}}^{(\text{r})} n_{\text{zp}} \quad (2.75\text{b})$$

$$= \sqrt{j+1} C_g V_{\text{zp}}^{(\text{r})} V_{\text{zp}}^{(\text{tr})}, \quad (2.75\text{c})$$

where in the last line we have identified $V_{\text{zp}}^{(\text{tr})} = 2en_{\text{zp}}/C_\Sigma$, the transmon's zero-point voltage fluctuations.

Note that Eq. (2.74) is a generalization of the Jaynes-Cummings Hamiltonian where now the ‘atom’ has infinitely many levels. Typically we are only interested in what happens within the $\{0, 1\}$ subspace of the transmon, so we can map Eq. (2.74) to a lower-dimensional model by making the correct identifications $|0\rangle\langle 0| - |1\rangle\langle 1| = \hat{\sigma}_z$ and $|0\rangle\langle 1| + |1\rangle\langle 0| = \hat{\sigma}_x = (\hat{\sigma}_+ + \hat{\sigma}_-)/2$. This gives

$$\hat{H}/\hbar \rightarrow -\frac{\omega_q}{2} \hat{\sigma}_z + \omega_r \hat{a}^\dagger \hat{a} + g(\hat{\sigma}_+ + \hat{\sigma}_-)(\hat{a} + \hat{a}^\dagger), \quad (2.76)$$

with $\omega_q = \omega_1 - \omega_0$ the *qubit frequency* and $g := 2g_{01} = 2C_g V_{\text{zp}}^{(\text{r})} V_{\text{zp}}^{(\text{tr})}$ the coupling rate¹¹. Note also that we neglected a constant energy offset $\delta = (\omega_0 + \omega_1)/2$. We can further simplify Eq. (2.76) by going to an interaction frame $\hat{H} \rightarrow \hat{H}' = \hat{U} \hat{H} \hat{U}^\dagger + i(\partial_t \hat{U}) \hat{U}^\dagger$, with $\hat{U} = \exp(-i\omega_q t \hat{\sigma}_z/2 + \omega_r t \hat{a}^\dagger \hat{a})$. In this frame the Hamiltonian is

$$\hat{H}' = g[\hat{\sigma}_+ \hat{a}^\dagger e^{i(\omega_q + \omega_r)t} + \hat{\sigma}_- \hat{a} e^{i(\omega_q - \omega_r)t} + \text{h.c.}] \quad (2.77\text{a})$$

$$\approx g(\hat{\sigma}_+ \hat{a} + \text{h.c.}). \quad (2.77\text{b})$$

Here we have assumed $\omega_q \approx \omega_r$ and threw out the fast-rotating terms, keeping only the slow ones. This motivates doing the same thing with the original Hamiltonian, removing the terms that do not

¹¹Most of the time when we talk about “ g ” we are referring to this one.

preserve the total number of excitations $\hat{N} = \hat{\sigma}_+ \hat{\sigma}_- + \hat{a}^\dagger \hat{a}$. This finally brings us to the Jaynes-Cummings model,

$$\hat{H}/\hbar = -\frac{\omega_q}{2}\hat{\sigma}_z + \omega_r \hat{a}^\dagger \hat{a} + g(\hat{\sigma}_+ \hat{a} + \hat{\sigma}_- \hat{a}^\dagger). \quad (2.78)$$

As the reader may already know this Hamiltonian is exactly solvable, with two families of eigenstates indexed by an integer number n of excitations:

$$|n, +\rangle = \sin \theta_n |n+1, 0\rangle + \cos \theta_n |n, 1\rangle \quad (2.79a)$$

$$|n, -\rangle = \cos \theta_n |n+1, 0\rangle - \sin \theta_n |n, 1\rangle, \quad (2.79b)$$

with $\tan \theta_n = (g/\Delta)\sqrt{n+1}$ and $\Delta = \omega_q - \omega_r$. The corresponding eigenenergies are

$$E_{n,\pm}/\hbar = \omega_r n \pm \frac{\Delta}{2} \sqrt{1 + \frac{4g^2(n+1)}{\Delta^2}}. \quad (2.80)$$

When we talk about ‘avoided crossings’ in Chapter 5, we are referring precisely to the spectroscopic signature of transitions between the states $|0, -\rangle \rightarrow |1, -\rangle$ and $|0, +\rangle \rightarrow |1, +\rangle$ as ω_q is swept across ω_r . Indeed, we see that as we approach the resonance condition ($\Delta = 0$), these transition frequencies are $\omega_r \pm g$. Their splitting is $2g$, so they avoid crossing each other so long as g is much larger than their linewidth. This is known as the *strong coupling regime* of cavity/circuit QED.

Dispersive limit: Schrieffer-Wolff transformation

The Hamiltonian of Eq. (2.74) accurately models all of the physics that will be demonstrated experimentally in Chapter 5, whether we are talking about a transmon coupling to a microwave readout resonator or to a mechanical resonator. There is a very interesting limit to this Hamiltonian, called the *dispersive limit*, which is reached when the first two transmon transitions ($0 \rightarrow 1$ and $1 \rightarrow 2$) are detuned very far away from the resonator frequency:

$$|\Delta| \gg g \quad (2.81a)$$

$$|\Delta - \alpha| \gg g, \quad (2.81b)$$

with $\Delta := \omega_{01} - \omega_r$. In this limit, Eq. (2.74), while still correct, fails to elucidate what is actually happening. Because the transmon and the resonator are now far off-resonant, we expect the process of exchange of quanta modeled by the interaction term in the Hamiltonian to be severely suppressed. In other words, in the dispersive limit, we would expect the Hamiltonian of Eq. (2.74) to morph into one that not only preserves the total number of excitations $\hat{N} = \hat{a}^\dagger \hat{a} + \sum j|j\rangle\langle j|$, but also *individually* the number of excitations $\hat{N}_r = \hat{a}^\dagger \hat{a}$ and $\hat{N}_{tr} = \sum j|j\rangle\langle j|$ in the resonator and in the transmon, respectively.

As a first step towards understanding this we will take a step back and consider the simpler

Jaynes-Cummings model of Eq. (2.78). If we think of the interaction term as a perturbation, it is easy to argue that the lowest-order correction to the energies is of second order in g/Δ . To see this quickly, we can expand the eigenenergies in Eq. (2.80) to lowest order in g/Δ :

$$E_{n,\pm}/\hbar \approx \left(\omega_r \pm \frac{g^2}{\Delta} \right) n \pm \frac{\Delta}{2} \pm \frac{g^2}{\Delta}. \quad (2.82)$$

This suggests that in this limit, the resonator frequency depends on which state the qubit is in, the difference between these two cases being $2g^2/\Delta$. This turns out to be correct — the shift between these two frequencies is called the *dispersive shift* — although this crude analysis clearly needs to be refined.

In my view, the most illuminating way to understand the dispersive limit is to transform the Hamiltonian using what is called a *Schrieffer-Wolff transformation* [111, 60]. An excellent exposition of this technique (at the level of experimentalists) is given in Ref. [130], which I will paraphrase here to keep this self-contained. I will then illustrate its application to the Jaynes-Cummings model, deferring the reader to Ref. [99] for a detailed derivation with the full transmon model.

We start by writing the full Hamiltonian as

$$H = H_0 + H' = H^0 + \epsilon V, \quad (2.83)$$

composed of an unperturbed part H_0 that we know how to diagonalize and a small perturbation $H' = \epsilon V$. Notice we are now omitting operator hats to keep the notation simple. We assume that the eigenvectors of H_0 live in two separate spaces A and B which are separated by a spectral gap Δ . The perturbation H' couples A and B , but we assume it does so weakly enough so that $|\epsilon| \leq \Delta/2||V||$, i.e. the gap is not closed. The Schrieffer-Wolff technique consists of finding a unitary transformation e^{-S} such that the transformed Hamiltonian

$$\tilde{H} = e^{-S} H e^S \quad (2.84)$$

is block diagonal — decoupling the two spaces A and B — up to the desired order of ϵ . Using the Baker-Campbell-Hausdorff formula we can expand the equation above as

$$\tilde{H} = \sum_{j=0}^{\infty} \frac{1}{j!} [H, S]^{(j)}, \quad (2.85)$$

where $[H, S]^{(j)} = [[H, S]^{(j-1)}, S]$ and $[H, S]^{(0)} = H$. We now decompose the perturbation H' as

$$H' = H_1 + H_2, \quad (2.86)$$

where H_1 is block diagonal and H_2 is block off-diagonal. Because S must be anti-hermitian and

block off-diagonal, the block off-diagonal part of \tilde{H} is

$$\tilde{H}_{\text{off}} = \sum_{j=0}^{\infty} \frac{1}{(2j+1)!} [H_0 + H_1, S]^{(2j+1)} + \sum_{j=0}^{\infty} \frac{1}{(2j)!} [H_2, S]^{(2j)}, \quad (2.87)$$

which we demand must vanish. Writing S as a power series

$$S = \sum_{j=1}^{\infty} S^{(j)}, \quad (2.88)$$

where $S^{(j)}$ is of order ϵ^j and $S^{(0)} = 0$, and assuming H_1 and H_2 are first order in ϵ , we can derive the following equations by matching terms of the same order in Eq. (2.87):

$$[H_0, S^{(1)}] = -H_2 \quad (2.89a)$$

$$[H_0, S^{(2)}] = -[H_1, S^{(1)}] \quad (2.89b)$$

$$[H_0, S^{(3)}] = -[H_1, S^{(2)}] - \frac{1}{3} [[H_2, S^{(1)}], S^{(1)}]. \quad (2.89c)$$

Since S is supposed to be unique, we just need to find and S that satisfies the above equations. Once we do, the transformed Hamiltonian (up to second order in ϵ) can be found through

$$\tilde{H} = H_0 + H_1 + [H_2, S^{(1)}] + \frac{1}{2} [[H_0, S^{(1)}], S^{(1)}] \quad (2.90a)$$

$$= H_0 + H_1 + \frac{1}{2} [H_2, S^{(1)}], \quad (2.90b)$$

which should now be block diagonal.

Let us apply this technique to the Jaynes-Cummings Hamiltonian. In this case the two subspaces A and B that we want to decouple are

$$A = \{|n, \downarrow\rangle \mid n = 0, 1, \dots\} \quad (2.91a)$$

$$B = \{|n, \uparrow\rangle \mid n = 0, 1, \dots\}. \quad (2.91b)$$

In other words A consists of all states with the qubit in the ground state and B consists of all states with the qubit in the excited state. Obviously the interaction term $H' = g(\hat{\sigma}_+ \hat{a} + \text{h.c.})$ couples these two subspaces because it induces transitions between states $|n, \uparrow\rangle \leftrightarrow |n+1, \downarrow\rangle$, whose energies are separated by the gap

$$\left(\omega_r n + \frac{\omega_q}{2}\right) - \left(\omega_r(n+1) - \frac{\omega_q}{2}\right) = \omega_q - \omega_r = \Delta. \quad (2.92)$$

In the language we just introduced above, $H' = H_2 = g(\hat{\sigma}_+ \hat{a} + \text{h.c.})$ and $H_1 = 0$. We now want to remove this coupling to second order in g . To make an ansatz for $S^{(1)}$ (only this order of S is

necessary, see Eq. 2.90b) we first notice that in order for $S^{(1)}$ to satisfy Eqs. (2.89a) it must contain terms similar to H_2 , in addition to being anti-hermitian. The obvious guess is $S^{(1)} = \alpha \hat{a}^\dagger \hat{\sigma}_- - \alpha^* \hat{a} \hat{\sigma}_+$. Substituting this into Eq. (2.89a) gives

$$S^{(1)} = \frac{g}{\Delta} (\hat{a}^\dagger \hat{\sigma}_- - \alpha^* \hat{a} \hat{\sigma}_+). \quad (2.93)$$

We can now use this to calculate the first non-zero correction to H_0 :

$$\frac{1}{2}[H_2, S^{(1)}] = \frac{g^2}{2\Delta} [\hat{a}^\dagger \hat{\sigma}_- + \hat{a} \hat{\sigma}_+, \hat{a}^\dagger \hat{\sigma}_- - \hat{a} \hat{\sigma}_+] \quad (2.94a)$$

$$= -\frac{g^2}{2\Delta} (\hat{a}^\dagger \hat{a} \hat{\sigma}_- \hat{\sigma}_+ - \hat{a} \hat{a}^\dagger \hat{\sigma}_+ \hat{\sigma}_- - \hat{a} \hat{a}^\dagger \hat{\sigma}_+ \hat{\sigma}_- + \hat{a}^\dagger \hat{a} \hat{\sigma}_- \hat{\sigma}_+) \quad (2.94b)$$

$$= -\frac{g^2}{2\Delta} (2\hat{a}^\dagger \hat{a} [\hat{\sigma}_-, \hat{\sigma}_+] - 2\hat{\sigma}_+ \hat{\sigma}_-) \quad (2.94c)$$

$$= -\frac{g^2}{2\Delta} \left(2\hat{a}^\dagger \hat{a} \hat{\sigma}_z - 2\frac{\mathbb{I} - \hat{\sigma}_z}{2} \right) \quad (2.94d)$$

$$= -\frac{g^2}{2\Delta} (2\hat{a}^\dagger \hat{a} + 1)\hat{\sigma}_z + \frac{g^2}{\Delta} \mathbb{I}. \quad (2.94e)$$

Putting everything together, we now have an effective Hamiltonian

$$\hat{H}_{\text{eff}} = -\frac{1}{2} (\omega_q - \chi) \hat{\sigma}_z + (\omega_r + \chi \hat{\sigma}_z) \hat{a}^\dagger \hat{a}, \quad (2.95)$$

where $\chi := -g^2/\Delta$, the dispersive shift. As promised, this Hamiltonian now individually preserves the number of excitations $\hat{N}_q = \hat{\sigma}_+ \hat{\sigma}_-$ and $\hat{N}_r = \hat{a}^\dagger \hat{a}$ stored in the qubit and the resonator, respectively. It also has two additional features. First, the qubit frequency gets renormalized to $\omega_q - \chi$. Second, the resonator frequency now depends on which state the qubit is in, the difference between these two possibilities being 2χ . Alternatively, if we just change the grouping of terms this shift can be seen as a shift of the qubit frequency that depends on the number of excitations \hat{N}_r stored in the resonator:

$$\omega_q(\hat{N}_r) = \omega_q - \chi - 2\chi \hat{N}_r. \quad (2.96)$$

These two interpretations can be used for two different things. First, the qubit-state-dependent shift of the resonator frequency can be used to (non-destructively) measure the state of the qubit in the $\{| \downarrow \rangle, | \uparrow \rangle\}$ basis [127]. Second, the \hat{N}_r -dependent shift of the qubit frequency can be used to (non-destructively) measure the number of quanta in the resonator. This latter measurement has been done with photons for decades now [12, 112]. In Chapter 5 I will present an experimental demonstration of this technique applied to a mechanical resonator, directly observing its phonon-number states.

Finally, as alluded to earlier, the calculation of the effective Hamiltonian for the full transmon case is more involved, but the principles are the same. The Hamiltonian ends up looking nearly the

same as Eq. (2.95), with the dispersive shift given by

$$\chi = -\frac{g^2}{\Delta} \frac{\alpha}{\Delta - \alpha}. \quad (2.97)$$

Often times these shifts end up being smaller than those of the two-level case, but this is not always true. See Ref. [60] for an in-depth discussion.

2.3 Piezoelectric coupling

Now that we have built a foundation in both acoustic waves in piezoelectric media and various kinds of superconducting circuits, it is time for us to analyze their coupling. Piezoelectric coupling arises when the deformation generated by the wave induces charges on the surface of the electrodes. To get some intuition, in this section I will show how these charges are calculated for a thin-film bulk-acoustic-wave resonator (FBAR), a one-dimensional problem with an analytic solution [30, 51]. A practical technique for extracting coupling rates computationally will be deferred to Chapter 3.

2.3.1 Toy model

In Fig. 2.6 I show a schematic of the FBAR configuration. It consists of two capacitor plates (assumed to have zero thickness) that sandwich a thin slab of piezoelectric material, of thickness b . We assume that $\mathbf{u}(\mathbf{x}) = u(z)\hat{\mathbf{z}}$, i.e. the deformation only depends on z and points along the z direction, and therefore $S_{33} = \partial u / \partial z \equiv S$ is the only non-zero component of the strain tensor. We also assume that $T_{33} \equiv T = c_{3333}S_{33} \equiv cS$ is the only non-zero stress component. These assumptions make the FBAR a *scalar* problem, greatly simplifying things.

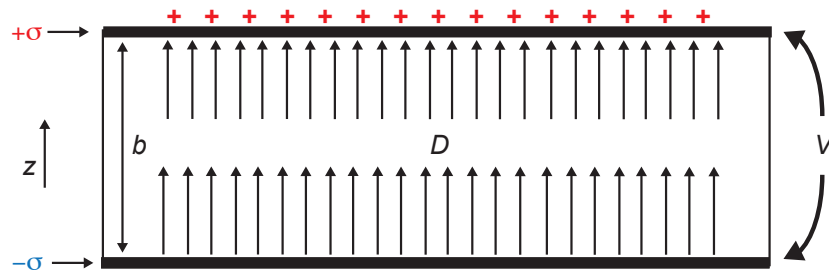


Figure 2.6: Sketch of FBAR.

Given what we know about elastic waves from Section 2.3, we can easily find the modes of this structure. In this case, the differential operator L in Eq. (2.9) is just $L = d\partial_z^2$, with $d = c + e^2/\epsilon$ (with $e := e_{333}$), and Eq. (2.9) is the simple wave equation $\rho\partial_t^2 u = d\partial_z^2 u$. The most general solution

is again the mode expansion of Eq. (2.10), and in this case the mode profiles are

$$U_n(z) = \alpha_n e^{ik_n z} + \beta_n e^{-ik_n z}, \quad (2.98)$$

i.e. linear combinations of forward- and backward-propagating waves. The frequency and wavevector are again related through the phase velocity, $\omega_n = (d/\rho)^{1/2} k_n$, and $n \in \{0, 1, \dots\}$ is a mode index.

In the case of stress-free boundaries ($\partial_z u|_{\pm b/2} = 0$), the mode functions adopt the form $U_n(z) = \alpha_n(e^{ik_n z} + (-1)^n e^{-ik_n z})/2$, with the wavevectors constrained to the discrete values $k_n = n\pi/b$. Here we are interested in the fundamental mode $n = 1$. This intuitively looks like a dilation of the film, with a node in the middle and maximum displacements at the boundaries. A more concise way to write down this solution is simply $u(z, t) = \alpha \sin(kz) \sin(\omega t)$, with $\alpha \in \mathbb{R}$ and $k = \pi/b$.

The goal is now to obtain a relationship that links the charge on the plates to the voltage and the amplitude of motion. Once we have this, we will immediately be able to calculate coupling rates. The first step is to invert the constitutive relations from Eqs. (2.1b, 2.1a), moving the electric field and stress to the left hand side as independent variables:

$$E_i = \epsilon_{ij}^{-1} D_j - h_{ijk} S_{jk} \quad (2.99a)$$

$$T_{ij} = -h_{ijk} D_k + d_{ijlm} S_{lm}, \quad (2.99b)$$

with $h_{ijk} = e_{lij} \epsilon_{lk}^{-1}$ and $d_{ijlm} = c_{ijlm} + e_{nij} \epsilon_{nk}^{-1} e_{klm}$. In one dimension they can be written succinctly as

$$\begin{pmatrix} E \\ T \end{pmatrix} = \begin{pmatrix} \epsilon^{-1} & -h \\ -h & d \end{pmatrix} \begin{pmatrix} D \\ S \end{pmatrix}, \quad (2.100)$$

with $h = e/\epsilon$ and $d = c + e^2/\epsilon$. Next we notice that the surface charge is related to the displacement field by $\sigma = -D$, and since there are no free charges in the slab ($\partial_z D = 0$), $D = -\sigma$ is constant. Using these relations we can calculate the stress and electric field profiles for the fundamental mode:

$$T = h\sigma + dk\alpha \cos kz \quad (2.101a)$$

$$E = -\sigma/\epsilon - hk\alpha \cos kz. \quad (2.101b)$$

Next, we set $T = 0$ at $z = \pm b/2$, and calculate the voltage from the electric field through $V = -\int E dz$. Putting everything together, we obtain $\sigma = \epsilon V/b - 2hk\alpha \sin(kb/2)/b$. Noticing that $\alpha \sin(kb/2) \equiv U$ is the deformation at the boundary and multiplying both sides by the plate area A , we finally obtain

$$Q = CV - 2hCU, \quad (2.102)$$

where $C = \epsilon A/b$ is the capacitance. We can also just as easily obtain the admittance function $Y(\omega) = V(\omega)/I(\omega)$, which will play a central role in Chapter 3.

Armed with Eq. (2.102) it is now straightforward to calculate the coupling rate between the fundamental FBAR mode and any external circuit that we connect it to, as done in Ref. [29].

2.3.2 General case

Even though it gives us plenty of intuition, the derivation above was only possible because we simplified the problem to its absolute simplest version. When trying to calculate couplings with arbitrary piezoelectric structures — such as phononic-crystal resonators — doing the calculation analytically is not feasible. It is of course possible to derive a formal expression for the coupling in terms of overlap integrals, e.g. as done in Ref. [133]. These expressions are only valid in a perturbative sense and their applicability to systems with very strong coupling is questionable. Finite-element solvers such as COMSOL [1] already compute the full solutions to the coupled equations of elasticity and electrostatics in arbitrary geometries; all we need to do is learn how to extract the numbers we want. This will be the topic of the next chapter.

Chapter 3

Engineering interactions between superconducting qubits and phononic nanostructures¹

Nanomechanical systems can support highly coherent microwave-frequency excitations at cryogenic temperatures. However, generating sufficient coupling between these devices and superconducting quantum circuits is challenging due to the vastly different length scales of acoustic and electromagnetic excitations. Here we demonstrate a general method for calculating piezoelectric interactions between quantum circuits and arbitrary phononic nanostructures. We illustrate our technique by studying the coupling between a transmon qubit and bulk-acoustic-wave, Lamb-wave, and phononic-crystal resonators, and show that very large coupling rates are possible in all three cases. Our results suggest a route to phononic circuits and systems that are nonlinear at the single-phonon level.

3.1 Introduction

Mechanical filters and resonators, because of their high quality factor and small size compared to electromagnetic components, have been a key part of classical high frequency circuits and systems for the last century [19, 64]. Advances in microwave-frequency quantum information processing systems have motivated experimental efforts to extend the success of acoustic devices to the quantum realm. In the last decade, a series of experiments have succeeded in coupling superconducting quantum circuits to mechanical resonators [53, 29, 63, 88, 94, 48, 65, 95, 4, 72]. These approaches have allowed explorations into new regimes of quantum optics [4] and enabled promising platforms

¹This chapter was published as: P. Arrangoiz-Arriola, A.H. Safavi-Naeini, “Engineering interactions between superconducting qubits and phononic nanostructures” *Phys. Rev. A* **94**, 063864 (2016)

for microwave-to-optical frequency conversion [107, 14, 10]. However, coupling of superconducting circuits to piezoelastic structures has only been studied in a few paradigmatic frameworks relevant to specific geometries utilizing surface- or bulk-acoustic waves. Expanding this repertoire to more complex and versatile designs has been hindered not only by technical challenges, but also due to the absence of a general theoretical framework for studying the piezoelectric coupling between these circuits and arbitrary piezoelastic structures.

A major motivation for developing such a framework stems from recent demonstrations of optically-probed microwave frequency mechanical resonators based on phononic-crystal resonators, with quality factors greater than 10^7 at milliKelvin temperatures and device footprints on the order of a few square microns [79]. Phononic crystals utilize periodicity at the acoustic wavelength scale to create a bandgap that protects localized phonons from tunnelling and Rayleigh scattering off of impurities and defects [47]. Such resonators, with orders of magnitude higher $f \times Q$ product compared to other technologies, do not fit neatly into previously studied paradigms of piezoelastic devices and approximate methods are not suited for understanding their coupling to qubits. In addition, their small effective size leads to extremely small coupling capacitances and ostensibly very small interaction rates.

Here we present a method for studying the interactions between quantum circuits and arbitrary piezoelastic structures. Our method utilizes only the linear response of the system and a microwave network synthesis technique [43, 85] to obtain the full Hamiltonian that describes the quantum dynamics of the hybrid system. We show that despite the mismatch in size and capacitance between qubit circuits and nanomechanical resonances, significant coupling rates leading to strong phonon-phonon interactions can be obtained.

To gain a better understanding of our method and of this result, in Sec. 3.2 we discuss a simplified analytical model of a quasi-1D piezoelastic resonator and derive the scaling law that relates the coupling rate to the size of the resonator. We then combine microwave network synthesis techniques [43, 85] with full-field finite-element simulations [1] of piezoelectric nanostructures to fully capture the interaction of quantum circuits with nanomechanical components. We present simulations of Lamb-wave and phononic-crystal resonances in Sec. 3.3 and Sec. 3.4, respectively, and show that the latter example can support a confined, small-mode-volume resonance that is nonlinear at the single-phonon level.

3.2 Thin-film bulk-acoustic-wave resonator

3.2.1 Model

Consider a thin-film bulk-acoustic-wave resonator coupled to a charge qubit. The mechanical element, highlighted in Fig. 3.1(a), consists of a thin film of piezoelectric material sandwiched between two electrodes. Ignoring edge effects, there is only one relevant dimension (the z direction normal to

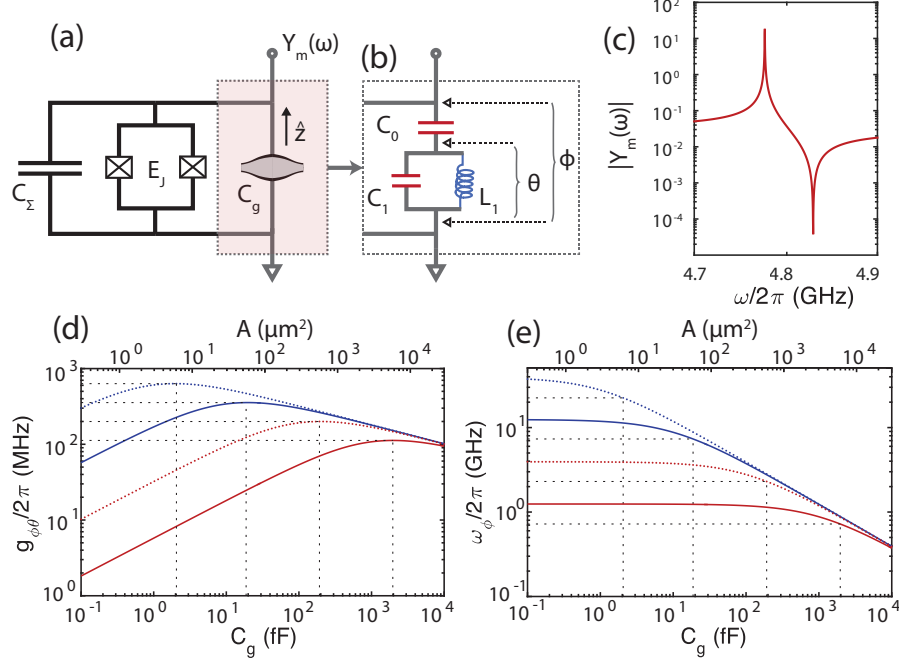


Figure 3.1: Thin-film bulk-acoustic-wave resonator. (a) A transmon with Josephson energy E_J and total capacitance C_Σ is shunted by a mechanical resonator (highlighted) described by an admittance function $Y_m(\omega)$; (b) Foster network synthesized from the electroacoustic admittance $Y_m(\omega)$ in the vicinity of the fundamental mechanical mode — units are 1/Ohm; (c) Exact admittance for a lithium niobate film of thickness $b = 750$ nm; (d) Dependence of the coupling rate $g_{\phi\theta}$ and (e) transmon frequency ω_ϕ on the gate capacitance C_g and electrode area A , with $E_J/\hbar = 2\pi \times 10$ GHz and $C_\Sigma = 10^0, 10^1, 10^2, 10^3$ fF (dotted blue, solid blue, dotted red, and solid red, respectively). C_g is changed by modifying only the capacitor area, so the mechanical frequency remains unaffected. The maxima of $g_{\phi\theta}$ occur when $C_0 \approx 2C_\Sigma$ (dashed black lines). As the mechanical resonator is shrunk to the regime $C_g \ll C_\Sigma$ the coupling rate falls off sublinearly as $g_{\phi\theta} \sim \sqrt{C_g}$.

the plates) and the system admits an analytic solution [51, 29] for the electrically coupled motional degree of freedom. The current induced on the electrodes is linearly related to the voltage across them through an admittance function

$$Y_m(\omega) = i\omega C_g \left[1 - K^2 \frac{\tan(\omega b/2\bar{v})}{\omega b/2\bar{v}} \right]^{-1}, \quad (3.1)$$

where $K^2 = e_{pz}^2/\bar{c}\epsilon$, e_{pz} is the electromechanical coupling constant in stress-charge form, $\bar{c} = c + e_{pz}^2/\epsilon$ is the stiffened elastic constant, b is the thickness of the film, and $\bar{v} = \sqrt{\bar{c}/\rho}$ is the speed of sound in the crystal. This exact admittance fully describes the response of the resonator. At frequencies much lower than the fundamental dilatational mode of the membrane, *i.e.*, time-scales longer than the time it takes sound to travel a distance b , the primary contribution to the admittance function is the static

electroelastic response, captured by the effective capacitance $C_g/(1 - K^2)$. At higher frequencies, elastic waves are excited and the linear response is modified. This is captured by the second term in Eq. (3.1), which results in a series of poles and zeros of $Y_m(\omega)$. The first zero at $\omega = 2\pi\bar{v}/2b \equiv \Omega$ corresponds to the fundamental electroacoustic mode of the system, with an associated pole at $\Omega_p < \Omega$. This pole-zero pair is shown in Fig 3.1(c). All subsequent pairs correspond to higher order excitations of the film.

3.2.2 Foster synthesis and two-mode Hamiltonian

Knowledge of $Y_m(\omega)$ is sufficient to obtain the full Hamiltonian of the system [85]. Using Foster's theorem [43], we synthesize an electrical linear lossless network that approximates the electroacoustic admittance (see Appendix A.3 for details). Restricting our attention to the fundamental mechanical mode, the Foster network becomes the three-node circuit shown in Fig. 3.1(b). The zero of the admittance is made explicit for this choice of synthesis, corresponding simply to $\Omega = 1/\sqrt{L_1 C_1}$. Here $C_1 = \lim_{\omega \rightarrow \Omega} \left\{ \frac{1}{2} \text{Im}[\partial_\omega Y_m(\omega)] \right\} = (C_g/2)(\pi/2K)^2$ is the effective mode capacitance and $C_0 = \lim_{\omega \rightarrow 0} \left\{ \text{Im}[\partial_\omega Y_m(\omega)] \right\} = C_g/(1 - K^2)$ is the electrostatic capacitance of the system, including the elastic contribution. In the limit of vanishing piezoelectric coupling ($K \rightarrow 0$), $C_1 \rightarrow \infty$ and $C_0 \rightarrow C_g$, so the network simply becomes the gate capacitance C_g — the mechanical resonator becomes invisible to the electrical terminals.

It is now straightforward to derive the Hamiltonian for the coupled transmon-resonator system. Starting from the circuit Lagrangian [36, 46] in terms of the generalized flux variables ϕ and θ , defined in Fig. 3.1(b), we arrive at the quantized Hamiltonian

$$\hat{H} = [4E_C^{(\phi)}(\hat{n}_\phi - n_g)^2 - E_J \cos \hat{\phi}] + \hbar\Omega \hat{a}^\dagger \hat{a} + 8E_C^{(\phi,\theta)} n_{\text{zp}}^\theta (\hat{a} + \hat{a}^\dagger)(\hat{n}_\phi - n_g). \quad (3.2)$$

Here \hat{a}^\dagger (\hat{a}) is the creation (annihilation) operator for the phononic mode described by the circuit variable θ and Ω is the phonon frequency, $E_C^{(\phi)}$ and E_J are the charging and Josephson energies for the transmon variable ϕ , $E_C^{(\phi,\theta)}$ is the cross-charging energy between the ϕ and θ nodes, and n_{zp}^θ is the magnitude of the zero-point charge fluctuations associated with θ . For a detailed derivation see Appendix A.1. In the transmon limit $E_J/E_C^{(\phi)} \gg 1$, the gate charge n_g can be eliminated by a gauge transformation [60]. Further, we can define operators \hat{b} , \hat{b}^\dagger for the harmonic oscillator approximating the transmon [60]. The transition frequency for the first two transmon levels is $\omega_\phi = \sqrt{8E_J E_C^{(\phi)}}/\hbar$, and the coupling term becomes

$$\hat{H}_{\text{int}} = -i\hbar g_{\phi\theta}(\hat{a} + \hat{a}^\dagger)(\hat{b} - \hat{b}^\dagger), \quad (3.3)$$

where

$$g_{\phi\theta} = 8E_C^{(\phi,\theta)} n_{\text{zp}}^\theta n_{\text{zp}}^\phi / \hbar \quad (3.4)$$

is the rate that sets the phonon-transmon interaction strength. This rate depends only on fundamental constants, the transmon parameters, and the network parameters (C_0, C_1, L_1) which can be readily computed from $Y_m(\omega)$.

3.2.3 Coupling rate

In Figs. 3.1(d) and (e), we plot the coupling rate $g_{\phi\theta}$ and the transmon frequency ω_ϕ over many orders of magnitude of the gate capacitance C_g and transmon capacitance C_Σ . Here we change C_g by changing the area of the gate capacitor while leaving the plate spacing b fixed. This changes the mass of the mechanical oscillator, whereas its frequency remains unmodified. It is interesting to first note that the coupling is maximized at $C_0 = 2C_\Sigma + \mathcal{O}(K^2)$. As we move to larger C_g , where $C_g \gg C_\Sigma$, the transducer capacitance dominates so both $g_{\phi\theta}$ and ω_ϕ lose all dependence on C_Σ and fall off to zero. Conversely, as $C_g/C_\Sigma \rightarrow 0$ the coupling vanishes and ω_ϕ limits to its uncoupled value. Finally, a salient feature of this model is that in the regime $C_g \ll C_\Sigma$, relevant to nanoscale mechanical resonators, the coupling rate scales sublinearly with the capacitances as $g_{\phi\theta} \sim (C_g^2/C_\Sigma^3)^{1/4}$. This suggests that shrinking down the resonator to a length scale of the order of the acoustic wavelength may be possible without significantly compromising the coupling rate. We remark that Eq. (3.2) is identical to a circuit QED Hamiltonian [60] with a transmon qubit, with the cavity photon operator replaced by a phonon operator.

We further note that this scaling with capacitor area is fairly general. The interaction energy between the electromagnetic and piezoelastic resonators is given by $Q_{\text{zp}}^{(\text{piezo})} V_{\text{zp}}^{(\text{qubit})}$, where $Q_{\text{zp}}^{(\text{piezo})}$ is the size of the charge fluctuations on the gate capacitance due to the zero-point motion of the mechanical system and $V_{\text{zp}}^{(\text{qubit})}$ is the size of the voltage fluctuations of the qubit in its ground state. The latter only depends on the qubit frequency and capacitance, and for a fixed E_J will scale as $(C_g + C_\Sigma)^{-3/4}$. The charge fluctuations on the gate capacitance scale as $C_g x_{\text{zp}} \propto \sqrt{C_g}$ since $x_{\text{zp}} \propto 1/\sqrt{m} \propto 1/\sqrt{C_g}$. This implies that the coupling scales as $C_g^{1/2}$ for $C_g \ll C_\Sigma$ and $C_g^{-1/4}$ for $C_g \gg C_\Sigma$, in agreement with our calculations for both the one-dimensional model presented above, and the full-field simulations of a Lamb-wave resonator presented below and shown in Fig. 3.2(e).

3.3 Lamb-wave resonator

Lamb-wave modes of films driven by interdigitated transducers (IDT) have found applications in classical information processing and sensing [134]. These devices are fabricated on suspended thin films, so all phonons are confined in two dimensions and phonon tunnelling into the bulk, which is a loss mechanism in SAW devices [48, 4], is eliminated. The system is shown in Fig. 3.2(a). When the IDT has many periods, there exists a resonance with a frequency that is nearly independent of the number of unit cells, N_{IDT} . We can therefore explore the dependence of the coupling rate $g_{\phi\theta}$ on the effective gate capacitance $C_g \propto N_{\text{IDT}}$ for this well-defined class of acoustic modes and benchmark a

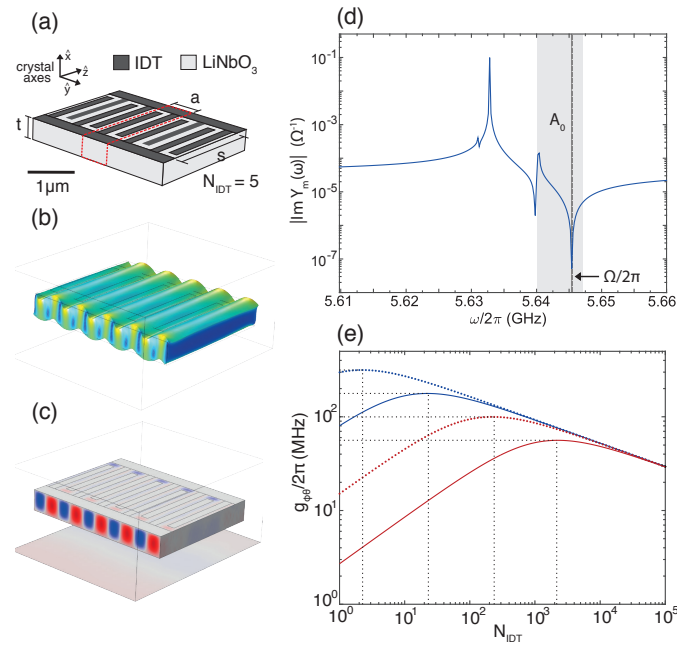


Figure 3.2: Lamb-wave resonator. (a) Simulation geometry for the resonator. An IDT with finger spacing $a = 600$ nm and $s = 1800$ nm is patterned over a thin film of lithium niobate of thickness $t = 400$ nm. The spacing a can be thought of as a lattice constant (unit cell highlighted). The IDT terminals are driven by an excitation voltage $V(\omega)$ to probe the electroacoustic admittance; (b) Deformation plot for the zeroth-order asymmetric Lamb mode (A_0) of wavelength $\lambda = a$; (c) Electrostatic potential distribution generated by the A_0 mode. The large overlap between the potential and the electrodes leads to strong piezoelectric coupling to A_0 ; (d) Simulated admittance per unit cell for frequencies near the Lamb mode resonance. The pole and zero corresponding to A_0 are shown in the shaded region. The zero located at $\Omega/2\pi = 5.645$ GHz corresponds to the phononic mode that interacts with the transmon in the single-mode model. The pole at ~ 5.63 GHz corresponds to a Lamb-like mode with spatial variation in the transverse direction that leads to an order of magnitude smaller coupling rate to the qubit; (e) Coupling rate to a transmon with $E_J/h = 20$ GHz as a function of the total number of unit cells N_{IDT} , with $C_\Sigma = 10^0, 10^1, 10^2, 10^3$ fF (dotted blue, solid blue, dotted red, and solid red, respectively). Here the gate capacitance per unit cell is ~ 1 fF — see Appendix A.3 for details.

realistic design as well as its scaling properties.

A finite-element simulation reveals the zeroth-order asymmetric Lamb-wave mode (A_0) at 5.64 GHz [Fig. 3.2(b)], with a voltage distribution mode-matched to the IDT fingers [Fig. 3.2(c)]. The mode frequency is set by the finger spacing a and the phase velocity along the y crystal axis, and is weakly dependent on the lateral resonator dimensions. In Fig. 3.2(d), we show the admittance $Y_m(\omega)$ seen by the circuit terminals at frequencies near the A_0 resonance, obtained from finite-element frequency response simulations to compute the current induced in response to an excitation voltage (see Appendix A.2 for details). Fitting $Y_m(\omega)$ to a complex rational function [49], we then synthesize the Foster network that reconstructs the Lamb mode admittance. Under a simplified model in which only the A_0 mode is relevant to the physics, the network is the same as that in Fig. 3.1(b) and the whole system is described by the two-mode Hamiltonian of Eq. (3.2). Plotting $g_{\phi\theta}$ as a function of N_{IDT} [Fig. 3.2(e)] then reveals the same scaling derived from the analytical model. In particular, even for a wavelength-scale resonator with ~ 10 unit cells, the coupling rate approaches $2\pi \times 50$ MHz for values of C_Σ typically used in transmon qubits.

3.4 Phononic-crystal-defect resonator

The fact that large coupling rates $g_{\phi\theta}$ are achievable with small gate capacitances opens the design space to study coupling to highly confined acoustic resonances. We consider a localized mode formed by engineering a defect site in a quasi-one-dimensional phononic crystal [Fig. 3.3(a) and (b)]. Such a phononic crystal can support a large mechanical bandgap [106], as shown in Fig. 3.3(c). This bandgap represents a range in frequency where propagation of all elastic waves is disallowed. By creating a defect in this structure, an acoustic mode with frequency inside the bandgap is localized. The characteristic length of this resonator is $\sim 1 \mu\text{m}$, on the order of the acoustic wavelength. Therefore its mode structure is much simpler and we can illustrate the full effect of coupling several acoustic modes to the same electrical terminals.

3.4.1 Black-box quantization

To perform the multimode analysis we proceed along the lines of black-box quantization [85]. This technique — outlined schematically in Fig. 3.4(a) — consists of lumping the linear part of the transmon into the electroacoustic admittance $Y_m(\omega)$ and synthesizing a Foster network from the total input admittance $Y_{11}(\omega)$ seen by the junction. For the choice of synthesis shown in Fig. 3.4(c), each of the LC blocks in the chain corresponds to a normal mode of the transmon-resonator system. This corresponds to diagonalizing the linear part of the total Lagrangian into polariton modes.

In terms of the normal mode coordinates $\{\psi_k\}$ and polariton frequencies $\{\tilde{\omega}_k\}$, this results in a

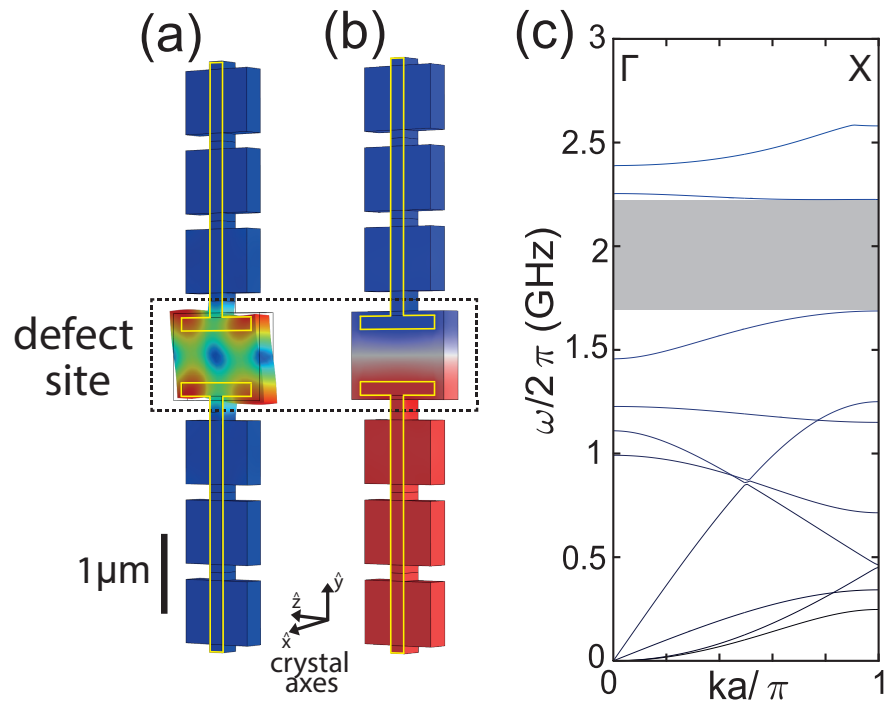


Figure 3.3: Phononic-crystal-defect resonator. (a) Deformation plot for the mode of interest at $\Omega/2\pi = 2.089$ GHz, showing a mode tightly localized to the defect region; (b) Electrostatic potential generated by the eigenmode, with a large gradient perpendicular to the symmetry plane at the center of the block. The electrodes used to drive the resonator are outlined in yellow. (c) Band diagram for the mirror region surrounding the defect site. A full bandgap centered near 2 GHz (shaded area) leads to strong confinement of any defect mode lying within this frequency band.

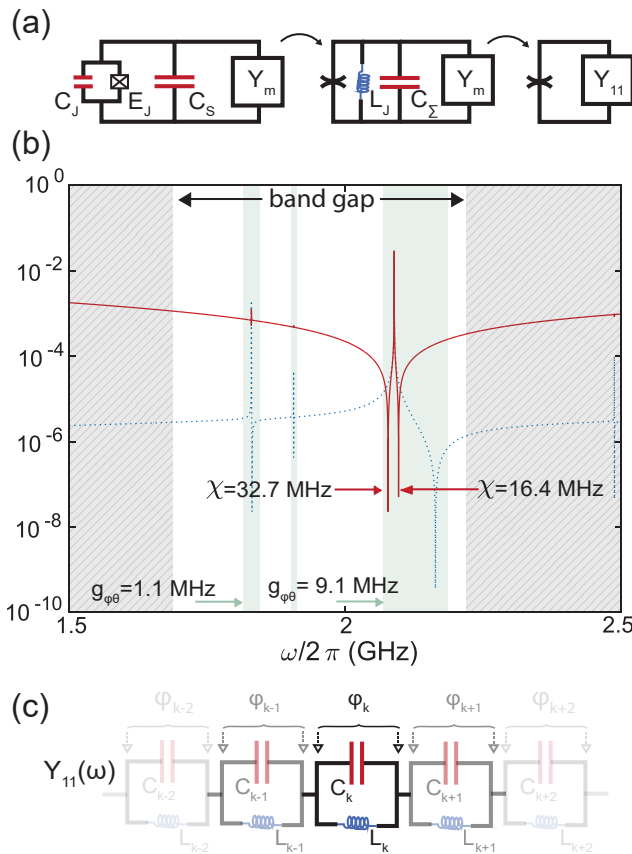


Figure 3.4: (a) In black-box quantization, a transmon with junction parameters E_J , C_J and shunt capacitance C_S is wired to a system described by an admittance function $Y_m(\omega)$. The total capacitance $C_\Sigma = C_J + C_S$ and the linear part of the junction inductance L_J are lumped into the black-box, resulting in a total input admittance $Y_{11}(\omega)$ shunting the nonlinear part of the junction (indicated by the spider symbol); (b) Bare electroacoustic admittance (dotted blue) of the defect site *only*, and total admittance $Y_{11}(\omega)$ (solid red) including the loading from a transmon with $C_\Sigma = 200$ fF, $C_J = 2.5$ fF, and frequency $\omega/2\pi = 2.1$ GHz. The strongly coupled mode with a pole at $\Omega/2\pi = 2.089$ GHz can be clearly observed in the admittance spectrum, along with other weakly coupled localized modes; (c) Foster network for $Y_{11}(\omega)$;

Lagrangian

$$L = \frac{1}{2} \sum_k C_k \left(\dot{\psi}_k^2 - \tilde{\omega}_k^2 \psi_k^2 \right) + E_J \cos \left(\sum_k \psi_k \right). \quad (3.5)$$

The Hamiltonian is

$$\hat{H} = \hbar \sum_k \omega_k \hat{a}_k^\dagger \hat{a}_k - E_J \cos \left[\sum_k \psi_k^{(\text{zp})} \left(\hat{a}_k + \hat{a}_k^\dagger \right) \right], \quad (3.6)$$

where the operators $\{\hat{a}_k^\dagger, \hat{a}_k\}$ create and annihilate the polaritonic excitations of the system [85]. In the $E_J/E_C \gg 1$ regime, the zero-point fluctuations $\psi_k^{(\text{zp})}$ for the phases are small, and Eq. 3.6 reduces to an effective Hamiltonian

$$\hat{H} = \hbar \sum_k \omega'_k \hat{a}_k^\dagger \hat{a}_k + \frac{1}{2} \hbar \sum_{kj} \chi_{kj} \hat{a}_k^\dagger \hat{a}_k \hat{a}_j^\dagger \hat{a}_j \quad (3.7)$$

capturing the two-phonon nonlinearities of the modes. Here the $\{\omega'_k\}$ are renormalized frequencies due to a Lamb-shift correction, and the $\{\chi_{kj}\}$ are the anharmonicites which can be computed from the Foster network parameters [85]. In Fig. 3.4(b), we indicate the coupling rates $g_{\phi\theta}$ for two localized acoustic modes, each computed separately using the two-mode model of Eq. (3.2). These show that one mode is indeed much more strongly coupled to the transmon, as already suggested from the admittance spectra. For this mode, we show values of χ_{kj} for the transmon-like and phonon-like polaritons for a bare transmon frequency $\omega_\phi/2\pi = 2.1$ GHz, slightly detuned from the $\Omega/2\pi = 2.089$ GHz acoustic mode. We see that the transmon-like polariton remains strongly anharmonic but also contributes a large anharmonicity to the phonon-like polariton.

3.4.2 Polariton anharmonicites

We can further study the dependence of the polariton anharmonicites on the detuning $\Delta = \omega - \Omega$, which we sweep by tuning the Josephson energy E_J . In Fig. 3.5, we show the anharmonicites of the transmon-like and phonon-like polaritons as a function of Δ . At large detunings, the phonon mode is essentially linear and the transmon mode has an anharmonicity that asymptotes to its uncoupled value $E_C \simeq e^2/2C_\Sigma$ [60] (dashed black line in figure). As the two modes become close to resonant, the coupling between the transmon and phonon causes mixing between the modes and the phonon-like mode obtains a large Kerr nonlinearity. Both the value of the self-Kerr (χ_{kk}) and cross-Kerr (χ_{jk}) nonlinearities are plotted in Fig 3.5. The maximum value of the anharmonicitiy of the phonon mode is a quarter of the maximum transmon anharmonicity, as expected from a simple hybridization model, and this leads to $\chi/2\pi \approx 24$ MHz for the phonon-like mode near $\Delta = 0$.

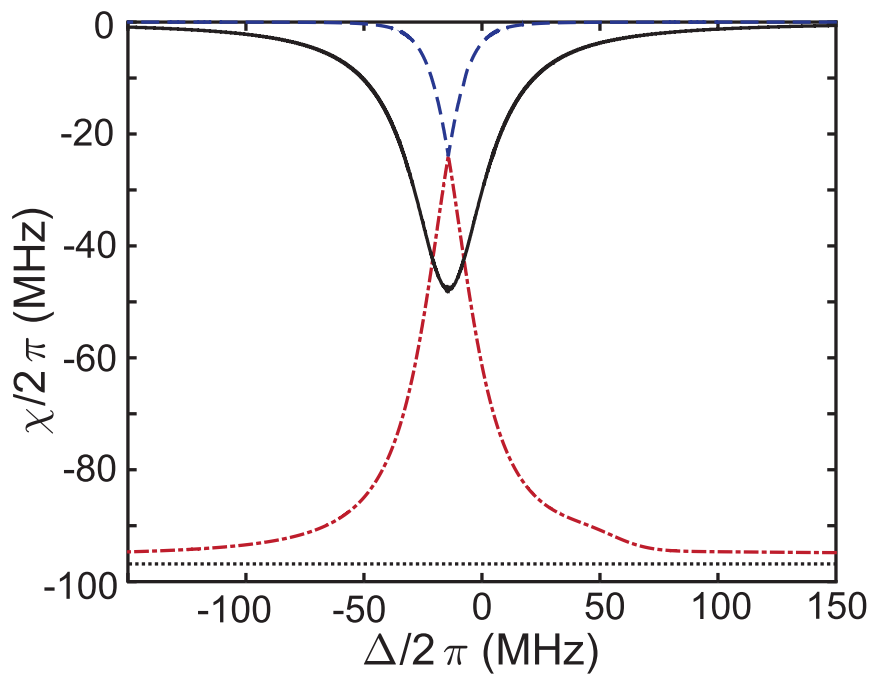


Figure 3.5: Anharmonicities of the phonon-like (dashed blue) and transmon-like (dash/dotted red) polaritons. As the detuning $\Delta = \omega - \Omega$ is tuned to zero, the phonon-like mode becomes strongly anharmonic and the cross-Kerr term (solid black) is maximized. Conversely, for large detunings the transmon anharmonicity limits to its uncoupled value (dotted black).

3.5 Conclusion

In conclusion, we have demonstrated a method for studying the coupling between arbitrary phononic structures and transmon qubits, and used it to show that large coupling rates can be achieved between thin-film, small-mode-volume piezoelastic resonators and transmon qubits despite their vastly different length scales. Our method can likely be extended to other quantum circuits, such as flux qubits. In addition to opening new ways of using acoustic elements in quantum circuits, we expect our results to be directly relevant to transducer designs for piezo-optomechanical devices currently being pursued for microwave-to-optical frequency conversion [14, 10].

Chapter 4

Coupling a superconducting quantum circuit to a phononic-crystal-defect resonator¹

Connecting nanoscale mechanical resonators to microwave quantum circuits opens new avenues for storing, processing, and transmitting quantum information. In this work, we couple a phononic-crystal resonator to a tunable superconducting quantum circuit. By fabricating a one-dimensional periodic pattern in a thin film of lithium niobate and introducing a defect in this artificial lattice, we localize a 6 gigahertz acoustic resonance to a wavelength-scale volume of less than one cubic micron. The strong piezoelectricity of lithium niobate efficiently couples the localized vibrations to the electric field of a widely tunable high-impedance Josephson junction array resonator. We measure a direct phonon-photon coupling rate $g/2\pi \approx 1.6\text{ MHz}$ and a mechanical quality factor $Q_m \approx 3 \times 10^4$ leading to a cooperativity $C \sim 4$ when the two modes are tuned into resonance. Our work has direct application to engineering hybrid quantum systems for microwave-to-optical conversion as well as emerging architectures for quantum information processing.

4.1 Introduction

Compact and low-loss acoustic wave devices that perform complex signal processing at radio frequencies are ubiquitous in classical communication systems [51]. Much like their classical counterparts, emerging quantum machines operating at microwave frequencies [35] also stand to benefit from

¹This chapter was published as: P. Arrangoiz-Arriola, E.A. Wollack, M. Pechal, J.D. Witmer, J.T. Hill, A.H. Safavi-Naeini, “Coupling a superconducting quantum circuit to a phononic crystal defect cavity” *Phys. Rev. X* **8**, 031007 (2018)

their integration with these devices. This is conditioned on the realization of sufficiently versatile *quantum phononic* technologies. Several promising approaches have emerged in the last few years. Each has its own strengths and weaknesses and they can be broadly categorized by the degree to which the acoustic waves are confined as compared to their wavelength. In a series of remarkable experiments, thin-film [88], surface [48, 73, 81, 86], and bulk-acoustic-wave resonators [26, 58] made of piezoelectric materials have coupled gigahertz phonons with varying levels of confinement to superconducting circuits. Nonetheless, smaller mode volumes, lower losses, and greater control over the mode structure are desired.

One of the most promising approaches for realizing ultra-low-loss mechanical resonators is to use phononic-crystal resonators that confine acoustic waves in all three dimensions. Wavelength-scale confinement and periodicity qualitatively alter the properties of waves and allow far greater control over the phonon density of states. Periodic patterning of a thin slab of elastic material can give rise to a phononic bandgap – a range of frequencies devoid of propagating waves. By introducing defects in such a crystal, mechanical energy is localized at the wavelength scale [40, 2, 14, 105, 10] without any “clamping” losses. The existence of a complete phononic bandgap eliminates all modes into which a phonon can be linearly scattered, leading to a significant increase in the coherence time of such resonators. For example, lifetimes on the order of one second corresponding to $Q > 10^{10}$ have been optically measured in 5 GHz phononic-crystal resonators made from silicon [70]. Moreover, the small mode volume of phononic-crystal resonators leads to a dramatic reduction in the density of spurious modes that can negatively impact performance of quantum acoustic systems, while enabling a denser packing of devices for greater scalability.

The greater confinement and control over the acoustic mode structure comes at the cost of weaker coupling. At gigahertz frequencies, the modes of phononic-crystal resonators are confined to extremely small volumes ($\lesssim 1\mu\text{m}^3$). This leads to smaller forces for a given oscillating voltage when compared to approaches with transducer dimensions of tens to hundreds of microns [6]. Up to now, it has only been possible to efficiently read out and couple to localized modes of phononic-crystal resonators with optical photons where the electromagnetic energy is similarly localized [40, 66]. Nonetheless, to connect these systems to microwave superconducting quantum circuits, efficient and tunable coupling between microwave photons and phonons is needed. In this work we demonstrate the direct coupling of a superconducting circuit to a wavelength-scale phononic nanoresonator, opening a new avenue in quantum acoustics.

4.2 Device design and fabrication

At the heart of our device lies a suspended quasi-one-dimensional phononic crystal fabricated from a 200-nanometer-thick film of lithium niobate (LiNbO_3). The crystal has a lattice constant of $1\mu\text{m}$ and has a complete phononic bandgap in the vicinity of $\nu = 6\text{ GHz}$ [Fig. 4.1(a)]. This bandgap

is used to localize the resonances of a single defect site introduced in the center of the lattice. In particular, we engineer a defect mode with a strain field S that generates a charge polarization $P_i = e_{ijk}S_{jk}$ that is predominantly aligned in-plane in the direction perpendicular to the lattice [Fig. 4.1(b)]; here e is the piezoelectric coupling tensor of LiNbO₃. We then use this polarization to couple the defect mode to the microwave-frequency electric field of a readout circuit, applied by gate electrodes placed within 200 nanometers of the defect. The readout circuit is a lumped-element microwave resonator formed from the capacitance C_r of the gate electrodes and a series of Josephson junctions in a superconducting quantum interference device (SQUID) array configuration with total Josephson inductance $L_r = \Phi_0^2/E_J(\Phi_e)$ [Fig. 4.1(c)], where $\Phi_0 = \hbar/2e$ is the reduced flux quantum. The effective Josephson energy $E_J(\Phi_0)$ of the array depends on the external flux Φ_e threading the SQUIDs, making the resonator frequency $\omega_r = 1/\sqrt{L_r C_r}$ tunable by applying a small current to an on-chip flux line. In addition, the small parasitic capacitance of the array enables us to achieve a relatively large resonator impedance $Z_r = \sqrt{L_r/C_r} \approx 580\Omega$. This is an important feature of our device, as the piezoelectric coupling strength is proportional to the zero-point voltage fluctuations of the circuit and $V_{zp} \sim \sqrt{Z_r}$. The resonator impedance is largely limited by the presence of the flux line (highlighted in red in Fig. 4.2), which is a major source of parasitic capacitance between the two nodes of the resonator. From simulations we estimate it contributes $\sim 10\text{ fF}$ to C_r .

Thin-film LiNbO₃ has recently gained prominence in the realm of classical radio frequency systems [129, 96, 124]. Here we perform the device fabrication on a 500-nm film of X-cut LiNbO₃ on a 500-μm high-resistivity ($> 3\text{ k}\Omega\cdot\text{cm}$) Si substrate and involves seven masks of lithography consisting of the following four stages [see Fig. 4.2(a)]: 1) LiNbO₃ film thinning, 2) patterning of phononic nanostructures, 3) deposition of Al layers, including all microwave circuitry and Josephson junctions, and 4) masked undercut of structures. The film is first thinned down to the target thickness (approximately 200 nm for this device) by blanket argon milling. We then pattern positive resist with a single step of electron-beam (ebeam) lithography and use it as the only masking material to etch the phononic nanostructures into the LiNbO₃ film using an optimized argon milling process. Now masking only the structures, an argon milling step is done to remove the LiNbO₃ film from the entire sample. This step allows us to place all microwave circuits on a high-resistivity silicon substrate where they are not vulnerable to acoustic radiation losses induced by the piezoelectric film. Aluminum microwave ground planes and feedlines are defined on the exposed silicon via liftoff, and the SQUID arrays are fabricated with a Dolan bridge double-angle evaporation process to grow the Al/AlOx/Al junctions [38, 115]. The gate electrodes used to address the phononic defect sites are patterned with a separate ebeam mask and normal-incidence Al evaporation, and finally a bandage process [39] is used to ensure lossless superconducting connections between all metalization layers. As a final step, we release the structures with a masked XeF₂ dry etch that etches the underlying Si with extremely high selectivity to the LiNbO₃ and the Al [96, 124], leaving all aluminum layers intact at the end of the process.

In Fig. 4.2(b) we show a set of scanning-electron micrographs of a finished device nearly identical to the one used in this experiment. The full microwave circuit is shown in the center. The charge line (highlighted blue) is capacitively coupled to the resonator and is used for driving and readout. The flux line (highlighted red) is used to apply either DC or RF magnetic fields to the SQUID array and tune the resonator frequency. The flux line is shorted to ground in a symmetric configuration in order to reduce leakage of photons through the mutual inductance between the resonator and the line. The junction array, placed $5\ \mu\text{m}$ away from the flux line, is composed of $N_{\text{SQ}} = 17$ nominally identical SQUIDs in series and has a total inductance $L_r \approx 11\ \text{nH}$ inferred by measuring the normal-state resistance of three copies of the array on the same chip. The two terminals of the SQUID array are routed to a set of electrodes used to address six independent phononic-crystal-defect resonators. These electrodes, the rest of the wiring, and the immediate environment of the resonator amount to a total capacitance of $C_r = 33\ \text{fF}$, determined from finite-element electrostatics simulations.

Each of the six resonators has the same nominal mirror cell design and therefore the same phononic band structure. As a result the modes that are supported by the resonators appear in the same frequency bands. In order to spectrally resolve these modes, we sweep the length a_{def} of the defect cells, from $1.4\ \mu\text{m}$ to $1.65\ \mu\text{m}$ in steps of $50\ \text{nm}$. Because the bandgap is quite small — only a small percentage of the center frequency — many defects do not support localized modes of the correct polarization (see Appendix B.4). By scaling the defect across the six resonators, we therefore increase the likelihood of generating and observing a localized mode.

4.3 Modeling and measurement results

We model our system as a microwave-frequency electromagnetic mode with annihilation operator \hat{a} and frequency ω_r that is linearly coupled, with a rate g , to a mechanical mode \hat{b} at frequency ω_m . This model is valid so long as we are interested in a range of frequencies sufficiently distant from other mechanical resonances in the system as compared to the relevant interaction rates. The Hamiltonian is

$$\hat{H}/\hbar = \omega_r \hat{a}^\dagger \hat{a} + \frac{\chi}{2} \hat{a}^{\dagger 2} \hat{a}^2 + \omega_m \hat{b}^\dagger \hat{b} + g(\hat{a} \hat{b}^\dagger + \hat{a}^\dagger \hat{b}), \quad (4.1)$$

where χ is the Kerr nonlinearity of the microwave mode introduced by the array. For an array of N_{SQ} identical SQUIDS this is given by $\hbar\chi = -E_C/N_{\text{SQ}}^2$, where $E_C = e^2/(2C_r)$ is the charging energy [46]. For this device $\chi/2\pi \approx -2\ \text{MHz}$, which is larger than the typical anharmonicity of parametric amplifier devices [132] but significantly smaller than that of transmon qubits [60]. We can further include the effect of a coherent drive sent into the input port by adding a drive term $\hat{H}_d/\hbar = -i\sqrt{\kappa_e}(\hat{a}^\dagger \alpha_{\text{in}}^{-i\omega_d t} - \text{h.c.})$ to the Hamiltonian, where κ_e is the extrinsic decay rate of the microwave mode into the readout channel and ω_d is the drive frequency. For sufficiently weak driving the system response is linear and the Kerr term in Eq. (4.1) can be neglected. Specifically, this is valid if $\chi\langle\hat{a}^\dagger \hat{a}\rangle \ll \kappa$, when the frequency shift induced by the drive is much smaller than the

total electromagnetic linewidth κ [41].

We perform our characterization measurements at the bottom plate of a dilution refrigerator at a temperature of $T = 7\text{ mK}$. We probe the system by measuring the reflection spectrum $S_{11}(\omega)$ through the charge port of the device (full details of the measurement setup are provided in Appendix B.5). In Fig. 4.3(a) we show a typical normalized reflection spectrum of the resonator in the linear regime, in this case tuned to a frequency of $\nu = 5.9\text{ GHz}$ far detuned from any mechanical resonance. The reflection coefficient is $S_{11}(\omega) = -1 + 2\eta_e\chi_r(\omega)$, where $\eta_e \equiv \kappa_e/\kappa$ is the coupling efficiency and $\chi_r(\omega) = [2i(\omega - \omega_r)/\kappa + 1]^{-1}$ is the dimensionless susceptibility (see Appendix B.1 for details). Fitting the data to this model, we obtain $\kappa/2\pi = 11\text{ MHz}$ and $\kappa_e/2\pi = 6.3\text{ MHz}$ at a resonator frequency of 5.9 GHz. This frequency is more than 2 GHz detuned from the flux sweet spot, leading to a broadened intrinsic linewidth $\kappa_i = \kappa - \kappa_e$ (see Appendix B.2). In Fig. 4.3(b) we show the linear spectroscopy results for a range of values of the external magnetic flux Φ_e , illustrating the DC-bias response $\omega_r(\Phi_e) = \omega_{r,\max}\sqrt{|\cos(2\pi\Phi_e/\Phi_0)|}$ of the resonator frequency. We infer $\omega_{r,\max}/2\pi = 8.31\text{ GHz}$, lying outside of our measurement band. Further, since the SQUIDs are composed of nominally identical junctions the lower frequency part of our tuning curve also lies outside of the measurement band.

We can now use the tunable response of the resonator to look for additional signatures in the spectrum. Tuning the resonance from the top of our measurement band at $\nu \approx 8\text{ GHz}$ down to $\nu \approx 5\text{ GHz}$, we find a series of resonances that anti-cross with the microwave mode, largely concentrated in the 6–6.5 GHz range. In Fig. 4.3(c) we show the anti-crossing of the most strongly coupled mechanical mode we found for this device, along with a line cut at the point of minimum detuning shown in Fig. 4.3(d). Using the entire anti-crossing dataset, we extract the parameters of the mechanical mode by fitting the spectrum to the simple linear input-output model described in Appendix B.1. In the case of a single mechanical mode coupled to the readout resonator, the reflection spectrum can be written as

$$S_{11}(\omega) = -1 + \frac{1}{1 + C\chi_m(\omega)\chi_r(\omega)} 2\eta_e\chi_r(\omega), \quad (4.2)$$

where $\chi_m(\omega) = [2i(\omega - \omega_m)/\gamma + 1]^{-1}$ is the dimensionless mechanical susceptibility and $C \equiv 4g^2/\kappa\gamma$ is the cooperativity. A least-squares fit to this model results in $\omega_m/2\pi = 5.9754\text{ GHz}$, $g/2\pi = 1.65 \pm 0.07\text{ MHz}$ and $\gamma/2\pi = 220 \pm 70\text{ kHz}$, corresponding to a mechanical quality factor $Q_m = \omega_m/\gamma \approx 3 \times 10^4$. The maximum cooperativity, i.e., the ratio of the mechanical resonator's electromagnetic read-out coupling to its intrinsic losses, approaches $C \approx 4.5$ on resonance. Crucially, our mode lies in a “quiet” region where the closest observed mechanical modes are 50 MHz and 250 MHz below and above, respectively (see Appendix B.3).

In order to better understand the measured electromechanical response, we perform finite-element

simulations of the full LiNbO₃ structure, simultaneously solving the equations of elasticity, electrostatics, and their coupling via piezoelectricity (see Appendix B.4 for details). Following a procedure described in Ref. [6], we numerically calculate the electromechanical admittance function $Y_m(\omega)$ seen at the electrical terminals of a single phononic resonator [1] and generate an effective circuit using Foster synthesis [85]. Using this technique we calculate coupling rates in the range $g/2\pi \approx 1.5 - 2.5$ MHz for the resonator geometries present in this device, in agreement with the measurement.

We measure the reflection spectra at higher drive power levels to verify the expected linearity of the mechanical resonance, and to distinguish it from other degrees of freedom, such as two-level systems (TLS) that have been observed in chip-scale devices [84]. The strong Kerr nonlinearity of the resonator allows us to calibrate the coherently-driven photon occupation. We set the resonator frequency to $\omega_r/2\pi = 5.90$ GHz, detuned from the mechanical mode, and vary the probe power. For very low powers, we can approximate the effect of the drive as a frequency shift $\delta\omega_r = \chi\langle\hat{a}^\dagger\hat{a}\rangle/2$ [Fig. 4.4(a)] and use this to extract the photon number. For low probe powers, we observe a linear dependence of the frequency shift as expected from a linearized model in which the steady-state occupation redshifts the resonance frequency seen by the probe tone. However, as the probe power is increased, a more complex nonlinear response is observed as evidenced by the deviation of the estimated $\delta\omega_r$ from the simplified linear dependence. We use the lower power points to obtain a nominal calibrated photon number $n_r = \langle\hat{a}^\dagger\hat{a}\rangle$, which is valid at low drive strengths and represents an upper bound to the occupation when extrapolated to stronger drives. This requires us to accurately estimate χ , which we do in two different ways: first using the measured resonator frequency and the normal-state junction resistance, and second by simulating the capacitance matrix of the device. Both of these methods give us nearly the same value of $\chi/2\pi = -2.0 \pm 0.1$ MHz. The uncertainty in this estimate roughly corresponds to the deviation between the two ways of obtaining it. We now place the resonator to the red side of the mechanical mode and change the driving strength while sweeping the probe frequency to obtain the traces shown in Fig. 4.4(b). We observe the microwave mode broaden and redshift as the occupation is increased to a few photons, while the mechanical mode remains unchanged. We therefore conclude that the observed resonance is not due to a TLS. Additionally, we note that the frequency and linewidth of the observed resonance remained constant over several experimental runs that involved temperature-cycling the device. Finally, measurements on a control sample with a nearly identical resonator design but without the LiNbO₃ resonators showed no coupled linear resonances in the frequency range 5 – 8 GHz, ruling out the possibility that the modes in question are spurious electromagnetic modes.

4.4 Outlook

We have demonstrated efficient coupling between a localized phononic resonator and a superconducting microwave circuit. The cooperativity $C \sim 4$ is already sufficient for efficient conversion of

microwave photons to highly localized microwave phonons that can in turn be up-converted efficiently to optical photons [66] – a promising route for microwave-to-optical conversion [106, 14, 123, 10]. We note that our approach of direct coupling to a phononic-crystal resonator differs from the “mode-conversion” scheme used in Ref [123], where interdigitated transducers generate Lamb waves that are then focused into the nanobeam from both ends. In our scheme, only one mechanical mode, the localized mode, plays a role in the coupling. This removes any loss associated with inefficient mode-conversion and scattering into spurious acoustic modes, e.g., arising from the multiple polarizations guided by the nanobeam [91]. Since there is only a single acoustic resonance present in the device at the frequency of interest, we are able to achieve efficient and tunable coupling that is robust to fabrication imperfections. From the measurements presented here, it is not clear whether the observed quality factors are limited by intrinsic material losses or by fabrication disorder and design. In the latter case, the performance of the device can be further improved by increasing the size of the bandgap to allow for higher mechanical Q . Larger phononic bandgaps lead to greater robustness to fabrication imperfections, which may currently limit the coherence time of the resonances (see Appendix B.3). Further investigation is required to understand the source of loss. In addition, optimizing the electrode placement and mode profile can lead to an increase in the coupling rate g .

For quantum acoustic structures to become competitive with the best electromagnetic cavities, higher interaction rates g and quality factors Q need to be achieved while minimizing spurious resonances to allow for fast gate operations [92]. Interestingly, due to the small capacitance of the transducer and the ability to minimize crosstalk between resonances through phonon bandgap engineering, this architecture lends itself well to engineering systems where many bosonic linear modes couple to a single qubit [83]. Whether such a quantum acoustic approach will be competitive in the realm of quantum information processing relies on improvements in the g and Q of the devices, which will be the focus of future work.

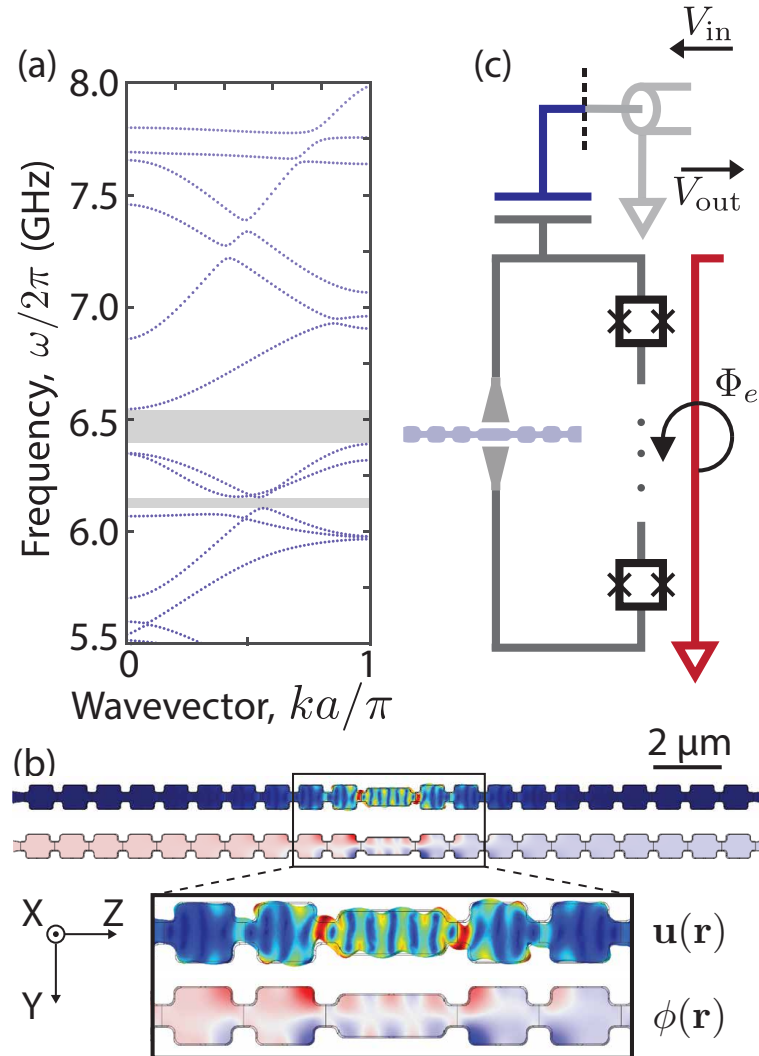


Figure 4.1: Concept and design. (a) Phononic bands of a LiNbO_3 quasi-one-dimensional phononic crystal with lattice constant $a = 1 \mu\text{m}$, showing the bands of all possible mode polarizations in the range of frequencies relevant to this work. A complete bandgap near $\nu = 6.5 \text{ GHz}$ is clearly visible, with a narrower gap also visible below. Other relevant simulation parameters (matching those of the fabricated structures) are the length and width of the connecting struts (320 nm and 240 nm, respectively), the film thickness (224 nm), and the sidewall angle (5°). (b) Deformation $\mathbf{u}(\mathbf{r})$ and electrostatic potential $\phi(\mathbf{r})$ of a mode localized at the defect site, at frequency $\nu = 6.48 \text{ GHz}$ near the center of the bandgap. Modes of this polarization can be coupled to electric fields pointing in the direction perpendicular to the crystal lattice. Here the length and width of the defect are $a_{\text{def}} = 1.6 \mu\text{m}$ and $w_{\text{def}} = 500 \text{ nm}$, respectively. (c) Schematic of the device, including the drive/readout line (blue) capacitively coupled to the resonator, the flux line (red) used to flux bias the SQUID array, and the electrodes (gray) that couple the circuit to the phononic resonator (light blue). The LiNbO_3 crystal axes are indicated.

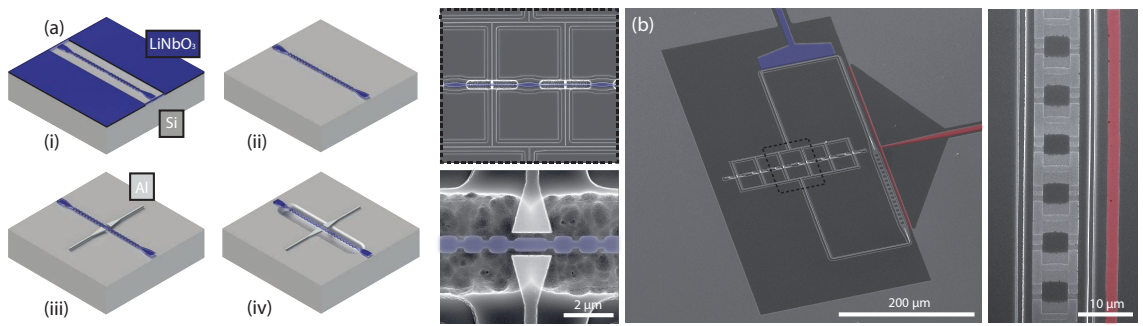


Figure 4.2: Device fabrication. (a) Schematic of the fabrication process, including (i) electron-beam patterning and argon milling of the phononic nanostructures in the LiNbO_3 film, (ii) masked removal of the film from the rest of the substrate, (iii) deposition of all metallization layers, and (iv) masked undercut of the structures. The last step suspends both the phononic resonators and the edge of the coupling electrodes over an etched Si trench. (b) False-colored scanning-electron micrographs of the final device. The charge and flux lines are highlighted in blue and red, respectively. A close-up of the SQUID array clearly shows the Al/AlO_x/Al junctions and the trenching in the Si substrate on either side of the array, produced by a deliberate gap between the electron-beam and photolithography masks used to pattern the LiNbO_3 film which results in the Si getting etched twice in those regions. To the left of the SQUID array a group of 6 phononic-crystal resonators, coupled to the array by 200 nm thick Al wires, is visible and highlighted by dashed black lines. A close-up of this region shows the LiNbO_3 structures (highlighted blue), including the bandgap regions, the defect site surrounded by the partially suspended aluminum electrodes, and the etched Si trench. The porous-like surface of the etched Si is attributed to micromasking during the XeF_2 undercut, but is likely unimportant as it is located far ($> 2\mu\text{m}$) from the region between the electrodes, where the electric fields are strongest.

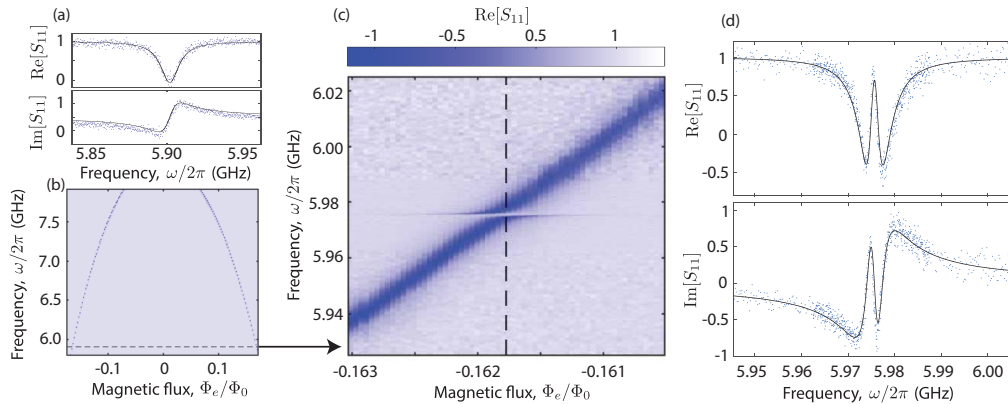


Figure 4.3: Linear spectroscopy. (a) Reflection spectrum $S_{11}(\omega)$ of the SQUID-array resonator tuned to a frequency of $\omega_r/2\pi = 5.90$ GHz, including the raw data and the fit to the model (solid lines). The data is normalized to a spectrum collected with a very large probe power ($P = 0$ dBm, nominal VNA output), where the nonlinear resonance is saturated and absent from the spectrum. At this frequency, we obtain resonator decay rates $\kappa/2\pi = 11$ MHz and $\kappa_e/2\pi = 6.3$ MHz. (b) Linear spectroscopy of the resonator with varying external flux. The resonance is observed to tune with the external flux Φ_e in the usual way and has a maximum frequency $\omega_{r,\max}/2\pi = 8.31$ GHz. (c) Close up at the frequency indicated by the black dashed line in the wider tuning plot. An anti-crossing of the microwave resonance and a mechanical mode at frequency $\omega_m/2\pi = 5.9754$ GHz is clearly observed, with the mechanical feature only visible when the resonator is tuned in close proximity. The data is collected at a higher frequency resolution within a 25 MHz band around the mechanical frequency in order to better resolve the mechanical mode away from resonance. The value of Φ_e at which the two modes are directly on resonance is marked by a black dashed line. (d) Line cut at the resonance showing the two dips observed in the reflection spectrum. A least-squares fit (solid black lines) is overlaid with the raw data, showing close agreement with the model.

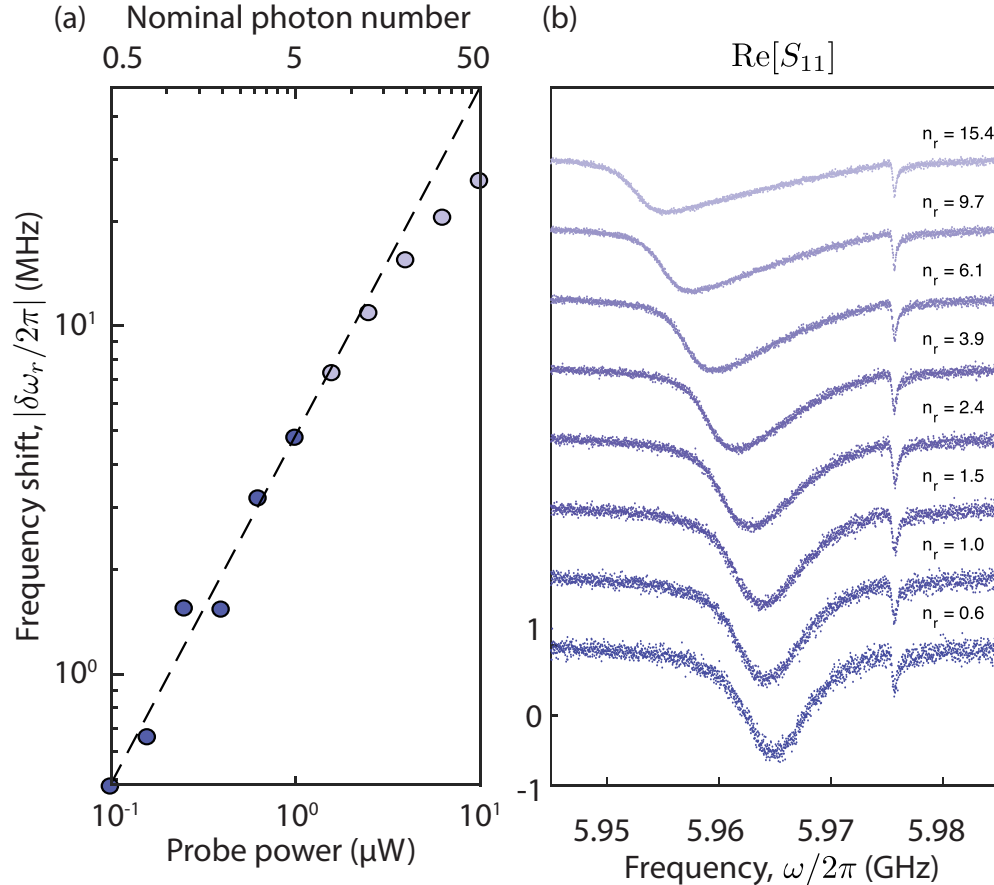


Figure 4.4: Nonlinear spectroscopy. (a) Frequency shift $\delta\omega_r \equiv \omega_r(n_r) - \omega_r(0)$ of the microwave resonance as a function of the probe tone power (at output from VNA). Since the anharmonicity χ is negative the resonator redshifts as its occupation n_r increases; here we plot the absolute value of the shift for clarity. As expected from a linearized model of a resonator with a Kerr nonlinearity, the shift has a linear dependence for weak driving strengths (dark blue points), but deviates from this trend at stronger driving (light blue points). We can calibrate the on-resonance occupation n_r by fitting $\delta\omega_r$ to a line in the weak driving regime (dashed black line), using a value of $\chi/2\pi = -2.0$ MHz for the anharmonicity. (b) Reflection spectra at various values of n_r , with the resonator placed to the red side of the mechanical mode. As the occupation increases the resonator redshifts as expected, while the mechanical mode remains unchanged.

Chapter 5

Resolving the energy levels of a nanomechanical oscillator¹

The quantum nature of an oscillating mechanical object is anything but apparent. The coherent states that describe the classical motion of a mechanical oscillator do not have well-defined energy, but are rather quantum superpositions of equally-spaced energy eigenstates. Revealing this quantized structure is only possible with an apparatus that measures energy with a precision greater than the energy of a single phonon, $\hbar\omega_m$. One way to achieve this sensitivity is by engineering a strong but nonresonant interaction between the oscillator and an atom. In a system with sufficient quantum coherence, this interaction allows one to distinguish different energy eigenstates by resolvable differences in the atom's transition frequency. For photons, such dispersive measurements have been studied in cavity [18, 12] and circuit quantum electrodynamics [112]. Here, we report an experiment where an artificial atom senses the motional energy of a driven nanomechanical oscillator with sufficient sensitivity to resolve the quantization of its energy. To realize this, we build a hybrid platform that integrates nanomechanical piezoelectric resonators with a microwave superconducting qubit on the same chip. We excite phonons with resonant pulses and probe the resulting excitation spectrum of the qubit to observe phonon-number-dependent frequency shifts ≈ 5 times larger than the qubit linewidth. Our result demonstrates a fully integrated platform for quantum acoustics that combines large couplings, considerable coherence times, and excellent control over the mechanical mode structure. With modest experimental improvements, we expect our approach will make quantum nondemolition measurements of phonons [15] an experimental reality, leading the way to new quantum sensors and information processing approaches [89] that use chip-scale nanomechanical devices.

¹This chapter was published as: P. Arrangoiz-Arriola*, E. A. Wollack*, Z. Wang, M. Pechal, W. Jiang, T. P. McKenna, J. D. Witmer, R. Van Laer, A. H. Safavi-Naeini, "Resolving the energy levels of a nanomechanical oscillator" *Nature* **571**, 537-540 (2019). *These authors contributed equally.

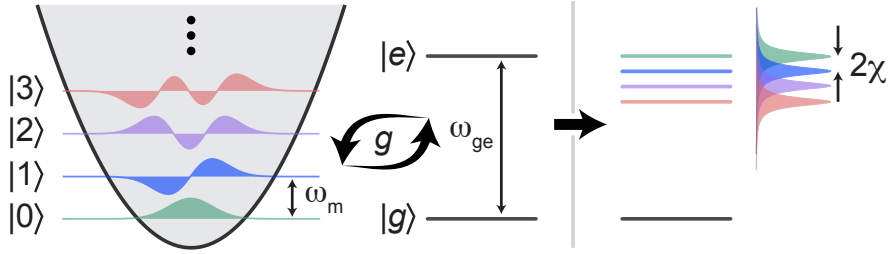


Figure 5.1: **Fig. 1 | phonon-number splitting scheme.** The state of a mechanical oscillator is described in quantum mechanics by a linear superposition of equally-spaced energy eigenstates $|n\rangle$, each representing a state of n phonons in the system. This quantized structure is normally not resolvable since the transitions between the energy levels all occur at the same frequency ω_m . By coupling the resonator to a qubit of transition frequency ω_{ge} with a rate g , we cause a splitting in the qubit spectrum parameterized by a dispersive coupling rate χ . This allows us to distinguish between the different phonon-number states that are present in the oscillator.

5.1 Introduction

In the last decade, mechanical devices have been brought squarely into the domain of quantum science through a series of remarkable experiments exploring the physics of measurement, transduction, and sensing [9, 88, 48, 33, 100, 27, 109, 125]. Two paradigms for obtaining quantum control over these systems are those of cavity optomechanics (COM), where the position \hat{x} parametrically couples to a higher-frequency electromagnetic cavity [9], and quantum acoustics (QA), where an artificial atom or qubit exchanges quanta with a mechanical oscillator. The latter is the acoustic analog of cavity or circuit QED (cQED), the archetypal playground of quantum optics that has enabled a vast range of experiments probing quantum physics [69] and led to the emergence of the superconducting approach to quantum information processing [35]. In QA systems, the exchange of quanta between a qubit and a mechanical oscillator is described by the Hamiltonian $\hat{H}_{\text{int}} = g(\hat{\sigma}_- + \hat{\sigma}_+)(\hat{b} + \hat{b}^\dagger)$, where g is the coupling rate, and $\hat{\sigma}_+$ ($\hat{\sigma}_-$) and \hat{b}^\dagger (\hat{b}) are the raising and lowering operators of the qubit and mechanical modes, respectively. Strong coupling of the system is realized for g greater than the decoherence rates of the qubit, γ , and mechanical mode, κ ; in this limit, a single excitation can be resonantly swapped multiple times before being lost to the environment. Experiments operating in this regime have demonstrated quantum control of mechanical systems at the single phonon level [88, 26, 109], as well as preparation of higher Fock states using more elaborate protocols [27].

In both COM and QA, approaches to probing the phonon-number states of a mechanical resonator invariably involve swapping phonons into a resonator or qubit acting as a meter. Alternatively, we can build a measurement apparatus that directly senses the mechanical energy stored in a resonator without the need to exchange excitations [125]. This quantum nondemolition (QND) approach to measuring motion has numerous advantages and remains an outstanding challenge in the

study of mechanical systems in the quantum regime. Cavity optomechanical approaches to QND attempt to couple the detector to the \hat{x}^2 as opposed to the \hat{x} observable of the mechanical system [120], but have required optomechanical coupling rates beyond current experimental capabilities [80, 68] to achieve phonon number resolution. In QA, detuning the qubit transition frequency $\omega_{\text{ge}} = \omega_m + \Delta$ from the mechanical frequency ω_m by $|\Delta| \gg g$ prevents the direct swap of real excitations between the two systems. Instead, it leads to an off-resonant interaction between the qubit and mechanics that results in an energy-dependent shift of the qubit frequency induced by virtual transitions. The effective Hamiltonian

$$\hat{H}_{\text{eff}} = \omega_m \hat{b}^\dagger \hat{b} + \frac{1}{2} (\omega_{\text{ge}} + 2\chi \hat{b}^\dagger \hat{b}) \hat{\sigma}_z, \quad (5.1)$$

accurately describes the system in this off-resonant regime [112]. Under \hat{H}_{eff} , the only interaction between the two systems manifests as a qubit frequency shift $2\chi \hat{n}$ dependent on the phonon number $\hat{n} = \hat{b}^\dagger \hat{b}$. For superconducting charge qubits operating in the transmon regime, the effects of the higher excited level ($|f\rangle$) must also be taken into account when calculating χ . The resulting expression for the dispersive coupling rate χ is distinct from the two-level atom case, and given by [60]

$$\chi = -\frac{g^2}{\Delta} \frac{\alpha}{\Delta - \alpha}, \quad (5.2)$$

where $\alpha = \omega_{\text{ge}} - \omega_{\text{ef}}$ is the transmon anharmonicity. Since \hat{H}_{eff} commutes with both the phonon number operator \hat{n} and $\hat{\sigma}_z$, the two systems cannot exchange energy, and so measurements of the qubit excited state population $(1 + \hat{\sigma}_z)/2$ do not perturb the phonon number. Furthermore, in the limit $\chi \gg \max\{\gamma, \kappa\}$, the frequency shift 2χ induced by the presence of a single phonon in the oscillator becomes resolvable in the qubit excitation spectrum. We call this the phonon-number splitting regime in analogy to the dispersive regime of cQED, where photons in an electromagnetic cavity [17, 112] or other bosonic excitations [61] lead to an energy-dependent atomic transition frequency. In cQED, the dispersive regime has been instrumental in implementing new approaches to quantum measurement and error correction [89].

5.2 Device

Several technical hurdles have prevented phonon-number splitting from being observed in quantum acoustics. The sub-micron wavelength of gigahertz-frequency acoustic phonons – far smaller than the scale of the electrodes comprising the qubit circuits – leads to an enormous phonon mode density accessible at the qubit transition frequency. Uncontrolled coupling to phonons is a known source of dissipation in cQED [52], and represents a major challenge in combining qubits with the strong piezoelectrics needed for phonon sensing and control. Systems designed to have large coupling rates tend to couple strongly to parasitic modes, reducing the overall coherence of the qubits as well as the availability of viable operating frequencies. Approaches to mitigating these losses have included

tunable couplers that isolate the qubit from the piezoelectric material by rapidly turning off the coupling after interaction [109], and bulk wave resonators where the participation ratio of the qubit electric field with the piezoelectric is reduced [26, 27]. Our approach avoids sacrificing coupling, while maintaining qubit coherence. We reduce the density of accessible mechanical modes that the qubit can radiate into by confining the phonons to a very small piezoelectric region where only a few mechanical modes are present at the frequencies of interest. Ordinarily, the leakage of phonons out of this region through its supporting anchors would lead to rapid decoherence of both the mechanics and the qubit. To realize leakage-free anchors, we create a periodic patterning of the elastic material that opens a phononic bandgap. Equivalently, we can view the mechanical resonator as a defect in a phononic-crystal bandgap material that is etched into a piezoelectric film.

To fabricate the chip-scale system, we integrate microwave Josephson junction qubits (aluminum on high-resistivity silicon) with piezoelectric nanomechanical devices patterned from thin-film lithium niobate (LN) (see Methods for fabrication details). As seen in Fig. 5.2, our system utilizes a transmon qubit of the type presented in Ref. [11], controlled via on-chip microwave lines and read out dispersively using a coplanar waveguide microwave readout resonator. In turn, the transmon is coupled to an array of one-dimensional phononic-crystal-defect resonators through the piezoelectricity of LN. Each mechanical structure consists of a narrow, suspended beam of patterned LN (Fig. 5.2b) with a periodicity $a = 1 \mu\text{m}$ that opens a complete bandgap in the $\sim 2 - 2.4 \text{ GHz}$ region. The defect site at the center of the phononic crystal supports highly confined mechanical modes with frequencies that lie within the bandgap (Fig. 5.2c, d). In order to address these modes, we place aluminum electrodes directly on top of the phononic crystal anchors. With one terminal grounded and another terminal contacted to the transmon, the voltage fluctuations of the qubit create an electric field in the defect site which is linearly coupled to its mechanical deformation by the piezoelectric effect. The structure is designed such that at least one of the localized modes generates a polarization that is aligned with the electric field produced by the electrodes (see Methods for design details).

5.3 Characterization via continuous-wave spectroscopy

We first probe the mechanical resonances by measuring the qubit excitation spectrum as we tune its transition frequency ω_{ge} across the phononic bandgap region. Here, frequency control is provided by a magnetic flux applied via an on-chip flux line, and the qubit is excited using a dedicated charge line. The state of the qubit is measured by using its dispersive interaction with the microwave readout resonator. We scatter a pulse off of the resonator and monitor the transmitted complex voltage (amplitude and phase) as we sweep the frequency of the spectroscopy pulse. After subtracting the voltage transmitted with the qubit in its ground state, the amplitude of the resulting signal is directly proportional to the qubit excited state population. The results of these measurements are shown in Fig. 5.3a, where we observe a series of anticrossings corresponding to various defect modes.

From this data we obtain the frequencies $\{\omega_m^{(i)}\}$ and coupling rates $\{g_i\}$ of the five most strongly coupled modes, each corresponding to an individual resonator in the array. We measure coupling rates in the range $g/2\pi = 13 - 16$ MHz, in fairly good agreement with finite-element simulations (see Methods). We also observe a set of anticrossings corresponding to a small number of additional, weakly coupled defect modes. For the phonon-number splitting measurements presented later, we use the highest-lying mechanical mode at $\omega_m^{(1)}/2\pi = 2.405$ GHz, for which we perform a ringdown measurement to find its decay rate $\kappa/2\pi = 370$ kHz. Next, in order to characterize the coherence of the qubit we tune it to $\omega_{\text{ge}}/2\pi = 2.301$ GHz, sufficiently far from all mechanical modes, and measure a qubit energy relaxation time $T_1 = 1.14\ \mu\text{s}$ and a total qubit linewidth $\gamma/2\pi \approx 600$ kHz. Finally, we extract the qubit anharmonicity $\alpha/2\pi = 138$ MHz using a two-tone spectroscopy measurement of the $|g\rangle \rightarrow |e\rangle$ and $|e\rangle \rightarrow |f\rangle$ transitions. All together, these parameters place the system deep in the strong-coupling regime ($g \gg \kappa, \gamma$), and open up the possibility of observing phonon-number splitting, with an expected dispersive shift $2\chi/2\pi \approx 3$ MHz.

5.4 Observation of phonon-number splitting

In order to observe phonon-number splitting, we perform a pump-probe measurement consisting of a short phonon excitation pulse followed by a longer qubit spectroscopy pulse (Fig. 5.4 inset), along with a readout pulse at the end to infer the qubit excited state population as described earlier. The phonon pulse is sent to the XY line of the qubit. Since the qubit and mechanics are weakly hybridized when far detuned, the pulse drives the mechanical system into an approximate coherent state. The duration τ of the spectroscopy pulse was chosen to balance two competing effects. The pulse bandwidth $\sim 1/\tau$ needs to be sufficiently small in order to resolve the narrowest spectroscopic features, which are of width $\sim \gamma$ in our system, while τ cannot be much longer than the phonon lifetime $1/\kappa$ since the mechanical mode must remain excited during measurement. Of the two requirements $\tau \gg \gamma^{-1} = 270$ ns and $\tau \lesssim \kappa^{-1} = 430$ ns, the first is necessary to observe number splitting, while the second determines the effective size of the observed mechanical state. We choose $\tau = 1.5\ \mu\text{s}$, which satisfies the first but not the second condition, in order to obtain better resolution for the phonon-number peaks. As we perform the measurement, the mechanical mode experiences significant dissipation, which limits the mean number of phonons we can observe in this experiment to $\langle \hat{n} \rangle \sim 1$. Additionally, the qubit frequency undergoes slow drift during the course of the measurement. To account for this, we periodically measure the qubit frequency with the phonon pulse turned off and use this to offset the data before averaging them (see Methods for a detailed discussion).

We use the highest-lying mechanical mode at $\omega_m^{(1)}/2\pi = 2.405$ GHz and detune the qubit by $\Delta \approx -6g$ to $\omega_{\text{ge}}/2\pi = 2.317$ GHz. By varying the amplitude of the preparation pulse, we prepare states of varying phonon occupations, resulting in the qubit spectra found in Figure 4. In addition

to the original $|g\rangle \rightarrow |e\rangle$ qubit transition, we observe a series of peaks corresponding to different phonon-number states $|n\rangle$ populated by the preparation pulse. The peaks are uniformly separated by $2\chi/2\pi \approx 3$ MHz, in close agreement with the dispersive shifts expected with our device parameters. The amplitude of the n^{th} peak is an indirect measure of the population of state $|n\rangle$, as evidenced by the fact that the relative heights of the peaks associated with $n > 0$ increase at higher excitation voltages. We also observe phonon-number-dependent linewidths for each peak, which can be understood as dephasing of the qubit due to the more rapid decay $n\kappa$ of higher-lying Fock states [44]. This broadens higher phonon-number peaks and obscures the quantization of the mechanical oscillator's energy. Therefore, at sufficiently large phonon occupations we enter a regime where the effect of the mechanical motion on the qubit spectrum is that of an ac-Stark shift induced by a coherent field [113, 125].

We numerically model our measurement using time domain master equation simulations that evolve the joint state $\hat{\rho}(t)$ of the mechanical mode and qubit over the course of the pulse sequence (see Supplementary Information). We use the full Hamiltonian to evolve the state — as opposed to the dispersive Hamiltonian of Eq. 5.1 — in order to correctly model the excitation of phonons via the transmon. The state of the system at the end of the excitation and spectroscopy pulses is given by $\hat{\rho}_f := \hat{\rho}(\tau_{\text{mech}} + \tau)$ and is used to calculate the qubit excited state populations $p_e = \text{Tr}\{\hat{\rho}_f|e\rangle\langle e|\}$. These are overlaid with the data in Fig. 5.4. The parameters used in the simulation are obtained from an independent set of calibrations as described in Methods. The only free parameter is a correction factor (on the order of 1) for the mechanical drive strength. An offset and a scaling factor are used to overlay the simulated excitation spectrum on the measurements. To provide an approximate measure of the size of the mechanical states in the resonator, we indicate the mean phonon number $\bar{n} := \text{Tr}\{\hat{\rho}(\tau_{\text{mech}} + \tau/2)\hat{b}^\dagger\hat{b}\}$ midway through the spectroscopy pulse next to each spectrum in Fig. 5.4.

5.5 Conclusion

We have demonstrated a quantum acoustic platform that combines phononic-crystal-defect modes with superconducting qubits. By using a phononic crystal bandgap, we reduce the mechanical and qubit dissipation rates while maintaining a large phonon-qubit coupling g . This enables us to dispersively resolve the phonon-number states of a mechanical resonator — a key step towards realizing QND measurements of a solid mechanical object and detecting quantum jumps of phonon number [15]. Looking forward, we expect phononic-crystal-based quantum acoustics to enable a new class of hybrid quantum technologies and provide a natural platform for integrating strongly piezoelectric materials with superconducting qubits. These types of mechanical resonators are also naturally suited for efficient optical readout due to the large mechanical mode confinement, and can provide a route for networking of microwave quantum machines [107, 14]. Moreover, very long

coherence times on the order of $300 \mu\text{s}$ have now been demonstrated on phononic-crystal devices implemented in silicon [71], suggesting that the mechanical dissipation of our devices can be improved with further investigation. Ultra-coherent mechanical resonators integrated with qubits provide a route to realizing quantum acoustic processors where phononic registers act as quantum memories that may simplify scaling of superconducting quantum machines [92]. Finally, by moving into the strong dispersive regime, our work enables further demonstrations, such as quantum nondemolition detection of single phonons [15] and generation of Schrödinger cat states of motion [126]. In this context, we would like to highlight a recent, independent observation of phonon-number splitting in a surface-acoustic-wave device [114].

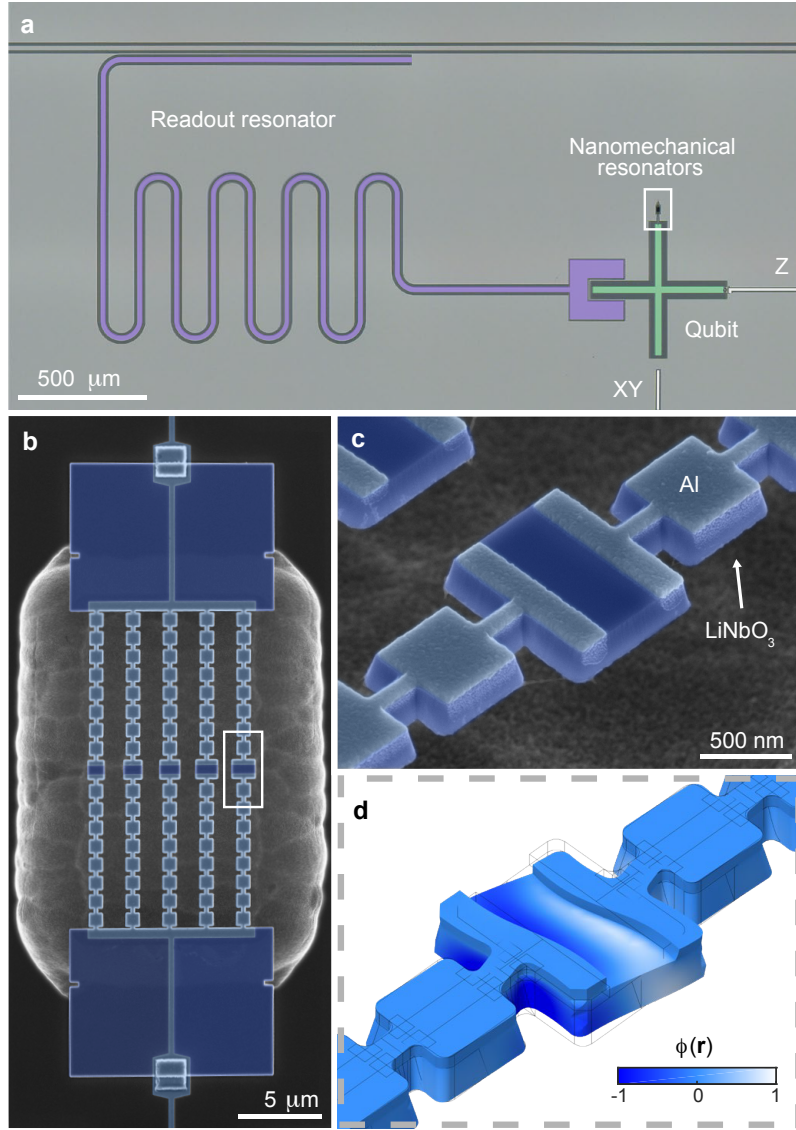


Figure 5.2: Fig. 2 | Fabricated device. **a**, False-colored optical micrograph of the device showing the readout resonator (purple), transmon qubit (green), and nanomechanical resonators (white box). The qubit flux control (Z) and excitation (XY) lines are shown in white. **b**, False-colored scanning-electron micrograph (SEM) of the suspended resonators. Each resonator consists of a defect site embedded in a phononic crystal that supports a complete phononic bandgap in the frequency range $\sim 2 - 2.4$ GHz. The structures are fabricated from a 250-nm film of lithium niobate (LN; dark blue) that is suspended above a silicon substrate, and are coupled to the qubit via thin aluminum electrodes (light blue) that address the defect modes. We form a connection between the electrodes and the qubit using superconducting bandages, which are visible as small squares at the edges of the LN supporting slabs. **c**, SEM image of a phononic crystal defect. **d**, Finite element simulation of a mechanical defect mode, showing the localized deformation of the structure and the electrostatic potential $\phi(\mathbf{r})$ (color) generated through the piezoelectricity of LN.

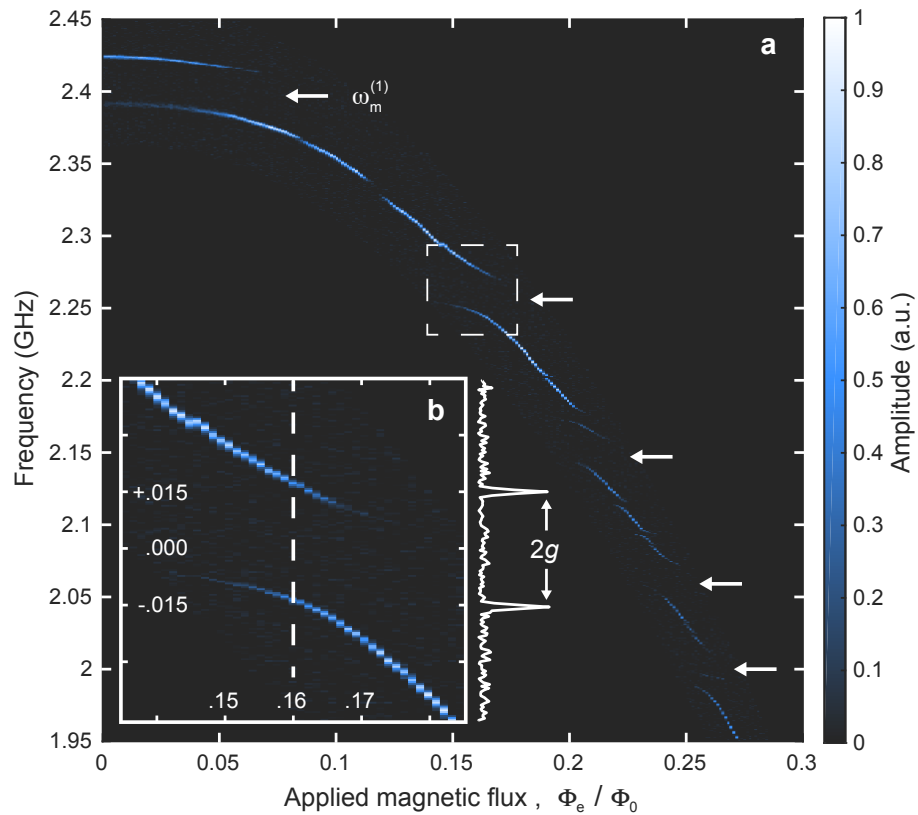


Figure 5.3: Fig. 3 | Qubit spectroscopy and mechanical mode structure. **a**, Qubit spectrum as a function of applied magnetic flux. Arrows indicate the strongly coupled mechanical modes associated with each of the five phononic-crystal-defect resonators. The qubit frequency at the flux sweet spot ($\Phi_e = 0$) is $\omega_{qe}^{(\text{max})}/2\pi = 2.417 \text{ GHz}$, in close proximity to the highest-lying mechanical mode at $\omega_m^{(1)}/2\pi = 2.405 \text{ GHz}$ which was used for the phonon-number splitting experiment. A small number of weakly coupled features are present in the spectrum, corresponding to additional localized defect modes. **b**, Close-up of the anticrossing with the mechanical mode at 2.257 GHz (dashed box in **a**). The vertical slice at zero detuning is shown in white to the right, and is used to calculate a coupling rate $g/2\pi = 15.2 \text{ MHz}$.

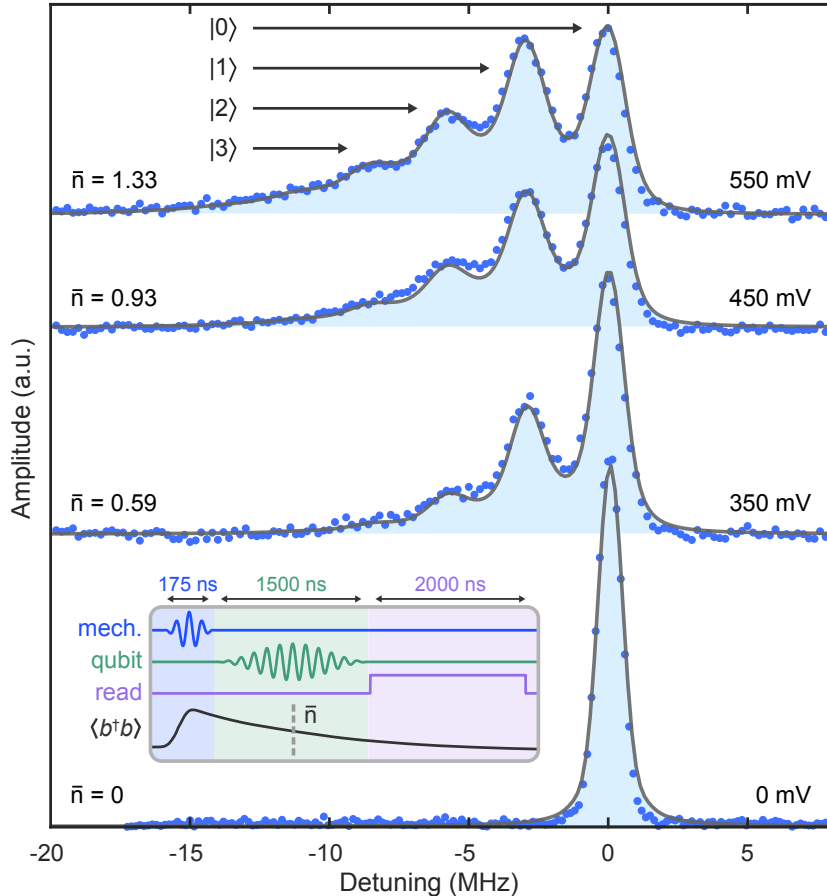


Figure 5.4: **Fig. 4 | phonon-number splitting.** The qubit excitation spectrum is measured following a phonon excitation pulse of duration $\tau_{\text{mech}} = 175 \text{ ns}$ and varying amplitude (see inset for pulse sequence). The detuning on the horizontal axis is relative to the qubit frequency $\omega_{\text{ge}}/2\pi = 2.317 \text{ GHz}$ in the absence of a phonon excitation pulse. The initial phonon populations prepared by the pulse decay over the course of the measurement, but are nevertheless visible as individual peaks split by twice the dispersive coupling rate, 2χ . At the highest drive amplitudes we are able to resolve up to the $n = 3$ phonon-number state. We fit the data (blue points) using numerical master equation simulations of the full pulse sequence (solid gray lines), with the mechanical drive strength as the only free fit parameter in the Hamiltonian. From these simulations we extract the mean phonon number $\bar{n} := \langle \hat{n}(\tau_{\text{mech}} + \tau/2) \rangle$ midway through the qubit spectroscopy pulse, which we indicate next to each spectrum.

Chapter 6

Outlook

In summary, I have introduced a powerful technique to calculate coupling rates between arbitrary piezoelectric structures and superconducting circuits. I then applied this technique to design and demonstrate a tunable SQUID array resonator coupled to a phononic-crystal-defect resonator (PCDR). Extending these methods I then presented a transmon qubit and an array of PCDRs capable of reaching not only the strong coupling regime but also the strong dispersive regime.

This avenue of research that we have started in the group is very promising and exciting, but before it can reach its full potential a number of technical milestones in device design and fabrication must be met.

On the design side, it is imperative to further reduce the exposure of the qubits to the piezoelectric material. The rationale of using phononic crystals is twofold: 1) to shrink the mechanical mode volumes to produce a clean, engineerable spectrum, and 2) to shrink the region of interaction as much as possible so as to reduce qubit decay via uncontrolled acoustic radiation. The devices here certainly meet the first point, but not yet the second. Solving this second issue is certainly a very interesting device design challenge, which may or may not be fundamentally feasible.

On the fabrication side, further systematic work must be done to elucidate the sources of mechanical decoherence. Considerable progress has already been accomplished in the group from the time of publication of Ref. [8], but there is probably plenty of room left for improvement. It will be interesting to see how far we can push the performance of lithium niobate devices at ultralow temperatures, which is certainly an unexplored frontier.

Once these improvements can be made, a large bounty of fascinating physics experiments awaits. One could start by porting over B. Johnson's 2010 experiment [56] — the first demonstration of quantum non-demolition detection of single photons in circuit QED — to the domain of acoustics. This experiment would be enabled by having good phonon number resolution in the strong dispersive regime, allowing for the interrogation of specific number states by performing conditional rotations on the qubit. Along the same lines, phonon number resolution opens up the possibility of preparing

Schrödinger cat states [126] — superpositions of coherent states — of mechanical motion, a long-held dream in the field. Finally, this also enables to monitor the parity $\hat{P} = \exp(i\pi\hat{a}^\dagger\hat{a})$ of the mechanical system and therefore track quantum jumps of phonon number in real time. This is now routine work in circuit QED [117] but remains a dream in quantum acoustics. Finally, it is interesting to wonder where these techniques will lead us in the realm of quantum sensing, an idea that I wish I had had more time to explore during my PhD.

What I did have time to explore was the possibility of using these devices for quantum computation. Inspired by our experimental progress M. Pechal wrote a nice proposal in 2018 detailing one possible way to use a transmon coupled to a large array of PCDRs for quantum computation [92], using the transmon to manipulate and entangle modes of the array in a serial fashion. And only weeks ago, C. Hann from Yale wrote another proposal to do the same thing but instead of serially, performing the gates all at the same time [50]. I sincerely hope that this enthusiasm for ‘quantum acoustic processors’ continues and that phononics makes a significant contribution to superconducting quantum computing. A mountain of technical hurdles remain before this can become a reality, but the night is young and the coffee cheap.

Appendix A

Supplementary information for Chapter 3: “Engineering interactions between superconducting circuits and phononic nanostructures”¹

A.1 Derivation of two-mode Hamiltonian

Starting with the circuit Lagrangian for a transmon coupled to a single-mode network (see Fig. 3.1 in the main text),

$$L = \frac{1}{2}C_0(\dot{\phi} - \dot{\theta})^2 + \frac{1}{2}C_1\dot{\theta}^2 + \frac{1}{2}C_\Sigma\dot{\phi}^2 + E_J \cos \phi - \frac{1}{2L_1}\theta^2, \quad (\text{A.1})$$

the canonical momenta are

$$\pi_\phi = \partial_{\dot{\phi}} L = C_0(\dot{\phi} - \dot{\theta}) + C_\Sigma\dot{\phi} \quad (\text{A.2})$$

$$\pi_\theta = \partial_{\dot{\theta}} L = -C_0(\dot{\phi} - \dot{\theta}) + C_1\dot{\theta}. \quad (\text{A.3})$$

¹This appendix is part of the following publication: P. Arrangoiz-Arriola, A.H. Safavi-Naeini, “Engineering interactions between superconducting qubits and phononic nanostructures” *Phys. Rev. A* **94**, 063864 (2016)

Writing Eqs. (A.2) & (A.3) in matrix form, we have

$$\begin{pmatrix} C_0 + C_\Sigma & -C_0 \\ -C_0 & C_0 + C_1 \end{pmatrix} \begin{pmatrix} \dot{\phi} \\ \dot{\theta} \end{pmatrix} = \begin{pmatrix} \pi_\phi \\ \pi_\theta \end{pmatrix}. \quad (\text{A.4})$$

Inverting the matrix, we obtain the time derivatives in terms of the momenta

$$\dot{\phi} = \frac{C_0 + C_1}{C_d^2} \pi_\phi + \frac{C_0}{C_d^2} \pi_\theta \quad (\text{A.5})$$

$$\dot{\theta} = \frac{C_0}{C_d^2} \pi_\phi + \frac{C_0 + C_\Sigma}{C_d^2} \pi_\theta, \quad (\text{A.6})$$

where $C_1 C_0 + C_\Sigma C_0 + C_\Sigma C_1 \equiv C_d^2$ is the determinant of the matrix. Substituting these relations into Eq. (A.1), and taking the Legendre transform $H = \pi_\phi \dot{\phi} + \pi_\theta \dot{\theta} - L$, we obtain

$$H = \frac{1}{2C_{01}^\Sigma} \pi_\phi^2 + \frac{1}{2C_{0\Sigma}^1} \pi_\theta^2 - \frac{\beta}{C_{1\Sigma}^0} \pi_\theta \pi_\phi - E_J \cos \phi + \frac{1}{2L_1} \theta^2. \quad (\text{A.7})$$

Here we introduced the notation $C_i + (C_j^{-1} + C_k^{-1})^{-1} \equiv C_{jk}^i$ for the equivalent capacitance formed by capacitances j and k in series, in parallel with i ; $\beta = C_0/C_1^\Sigma$ (in our notation, $C_1^\Sigma = C_1 + C_\Sigma$) is a participation ratio that will determine the phonon-transmon coupling.

To write down the Hamiltonian in the more familiar circuit QED notation, we define the dimensionless charges $n_\phi = \pi_\phi/2e$, $n_\theta = \pi_\theta/2e$, the charging energies $E_C^{(\phi)} = e^2/2C_{01}^\Sigma$, $E_C^{(\theta)} = e^2/2C_{0\Sigma}^1$, $E_C^{(\phi,\theta)} = \beta e^2/2C_{1\Sigma}^0$, and the inductive energy $E_L = \Phi_0^2/L_1$, where $\Phi_0 = \hbar/2e$ is the reduced flux quantum. Finally, we quantize the degrees of freedom and obtain

$$\hat{H} = 4E_C^{(\phi)}(\hat{n}_\phi - n_g)^2 - E_J \cos \hat{\phi} + 4E_C^{(\theta)}\hat{n}_\theta^2 + \frac{1}{2}E_L\hat{\theta}^2 + 8E_C^{(\phi,\theta)}(\hat{n}_\phi - n_g)\hat{n}_\theta, \quad (\text{A.8})$$

where we have introduced an additional gate charge n_g because, due to the topology of the circuit, the spectrum of \hat{n}_ϕ is discrete [60]. We can write the Hamiltonian in a more familiar form by defining the harmonic oscillator quadratures

$$\hat{n}_\theta = n_{\text{zp}}^\theta (\hat{a} + \hat{a}^\dagger) \quad (\text{A.9})$$

$$\hat{\theta} = i\theta_{\text{zp}}(\hat{a}^\dagger - \hat{a}), \quad (\text{A.10})$$

with

$$n_{\text{zp}}^\theta = \frac{1}{2} \left(\frac{E_L}{2E_C^{(\theta)}} \right)^{1/4} \quad (\text{A.11})$$

$$\theta_{\text{zp}} = \left(\frac{2E_C^{(\theta)}}{E_L} \right)^{1/4}, \quad (\text{A.12})$$

so that

$$\hat{H} = [4E_C^{(\phi)}(\hat{n}_\phi - n_g)^2 - E_J \cos \hat{\phi}] + \hbar\Omega \hat{a}^\dagger \hat{a} + 8E_C^{(\phi,\theta)} n_{\text{zp}}^\theta (\hat{a} + \hat{a}^\dagger)(\hat{n}_\phi - n_g). \quad (\text{A.13})$$

The term in brackets is nothing more than the transmon Hamiltonian, the second term describes a harmonic oscillator with frequency $\Omega = (L_1 C_{0\Sigma}^1)^{-\frac{1}{2}} \approx (L_1 C_1)^{-\frac{1}{2}}$, and the third term is a coupling between the oscillator position and the transmon charge. We therefore identify the circuit variable ϕ as the transmon degree of freedom, and the θ variable as the phonon degree of freedom. Going to the transmon limit $E_J/E_C^{(\phi)} \gg 1$, where the zero-point fluctuations of $\hat{\phi}$ are small, we can expand the $\cos \hat{\phi}$ term in Eq. (A.13) to quartic order and define the approximate transmon quadratures [60]

$$\hat{n}_\phi = i n_{\text{zp}}^\phi (\hat{b}^\dagger - \hat{b}) \quad (\text{A.14})$$

$$\hat{\phi} = \phi_{\text{zp}} (\hat{b} + \hat{b}^\dagger), \quad (\text{A.15})$$

with

$$n_{\text{zp}}^\phi = \frac{1}{2} \left(\frac{E_J}{2E_C^{(\phi)}} \right)^{1/4} \quad (\text{A.16})$$

$$\phi_{\text{zp}} = \left(\frac{2E_C^{(\phi)}}{E_J} \right)^{1/4}, \quad (\text{A.17})$$

yielding

$$\hat{H} \simeq [\hbar\omega_\phi \hat{b}^\dagger \hat{b} - \frac{E_C^{(\phi)}}{12} (\hat{b} + \hat{b}^\dagger)^4] + \hbar\Omega \hat{a}^\dagger \hat{a} - i\hbar g_{\phi\theta} (\hat{a} + \hat{a}^\dagger)(\hat{b} - \hat{b}^\dagger), \quad (\text{A.18})$$

where

$$\omega_\phi = \sqrt{8E_C^{(\phi)} E_J / \hbar} \quad (\text{A.19})$$

is the transmon frequency and

$$\hbar g_{\phi\theta} = 8E_C^{(\phi,\theta)} n_{\text{zp}}^\theta n_{\text{zp}}^\phi \quad (\text{A.20})$$

is the coupling energy that sets the phonon-transmon interaction strength.

A.2 Finite element simulations

In order to study resonator designs of arbitrary geometries, we perform full-field finite element method (FEM) simulations to obtain the electroacoustic admittance $Y_m(\omega)$. Using COMSOL Multiphysics [1], we simultaneously solve the equations of elasticity, electrostatics, and their coupling via the piezoelectric constitutive relations

$$D_i = \epsilon_{ij}E_j + e_{ijk}S_{jk} \quad (\text{A.21})$$

$$T_{ij} = c_{ijlm}S_{lm} - e_{lij}E_l, \quad (\text{A.22})$$

written in stress-charge form. All repeated indices are summed over. Here D is the electric displacement field, E is the electric field, T is the stress tensor, S is the strain tensor, and ϵ , c , and e are the permittivity, stiffness, and piezoelectric coupling tensors, respectively. We can either solve for the eigenmodes of the structure, or perform a frequency response simulation in which an oscillating voltage with amplitude $V(\omega)$ is set on the electrodes as a boundary condition and the field solutions are used to compute the current $I(\omega)$ induced on the electrodes, thereby extracting the admittance

$$Y_m(\omega) = \frac{I(\omega)}{V(\omega)}. \quad (\text{A.23})$$

This is conceptually identical to the calculation of $Y_m(\omega)$ in Eq. (3.1) in the main text, but is otherwise intractable without numerical tools.

Lamb-wave resonator. The simulation geometry for the Lamb-wave resonator consists of a thin layer of X-cut lithium niobate crystal of thickness $t = 400$ nm. The X-cut crystal orientation is implemented by introducing a rotated coordinate system in the simulations (crystal axes labeled in Fig. 3.2 in the main text). An interdigitated (IDT) capacitor is used to selectively transduce the asymmetric zeroth-order Lamb mode (A_0) with a wavelength equal to the IDT finger spacing $a = 600$ nm (see Fig. 3.2). In the example discussed in this work, the IDT spans a width $s = 1800$ nm. The terminals are treated solely as voltage boundary conditions on the surface of the LN — performing more realistic simulations where the terminals are treated as compliant metallic films only slightly modifies the results. Further, the domain of the simulation extends beyond the structure in order to take into account the effect of the fields in vacuum.

Before calculating $Y_m(\omega)$, we perform eigenmode simulations for rapid characterization of the spectrum and identification of the A_0 mode. We also verify the weak dependence of the frequency of A_0 on the lateral dimension s and the number of unit cells N_{IDT} .

In order to simplify the scaling calculations (*i.e.* the calculation of $g_{\phi\theta}$ as a function of N_{IDT}), we impose Floquet boundary conditions (with $k = 0$) on the boundaries of the structure perpendicular to the direction of propagation of the A_0 mode. This is equivalent to setting a cyclic boundary

condition on a finite one-dimensional crystal — it eliminates edge effects and guarantees that the frequency of A_0 is independent of the total number of unit cells, as independently verified through eigenmode simulations. Due to the periodicity of the structure, the admittance $Y_m^{(N)}(\omega)$ of a resonator with N unit cells is $Y_m^{(N)}(\omega) = NY_m^{(1)}(\omega)$, where $Y_m^{(1)}(\omega)$ is the admittance of a single unit cell. In circuit language, the periodicity allows us to partition the N_{IDT} unit cells into N_{IDT} parallel networks. This drastically simplifies the calculation, effectively reducing the problem to a numerical simulation of a single unit cell.

Phononic-crystal-defect resonator. The first step in the design flow for the defect resonator is to fully characterize the band structure of the mirror region that supports the bandgap. To this end, we perform eigenmode simulations of a single unit cell with Floquet boundary conditions and sweep the k vector over the one-dimensional Brillouin zone. For a unit cell with dimensions as shown in Fig. A.1, this generates the band diagram shown in Fig. 3.3 in the main text. We then design a defect cell with an eigenmode deep inside the bandgap and verify its confinement by simulating the full structure as shown in Figs. 3.3(a) and (b). The defect cell dimensions are indicated in Fig. A.1, and we again use an X-cut crystal orientation (crystal axes labeled in Fig. 3.3). The electrostatic potential generated by the eigenmode has a large gradient perpendicular to the symmetry plane at the center of the block. This motivates placing two electrical terminals that overlap with the blue and red regions in the plot in order to maximize coupling. We then test the mode remains bound after placing voltage terminals that run along the tethers.

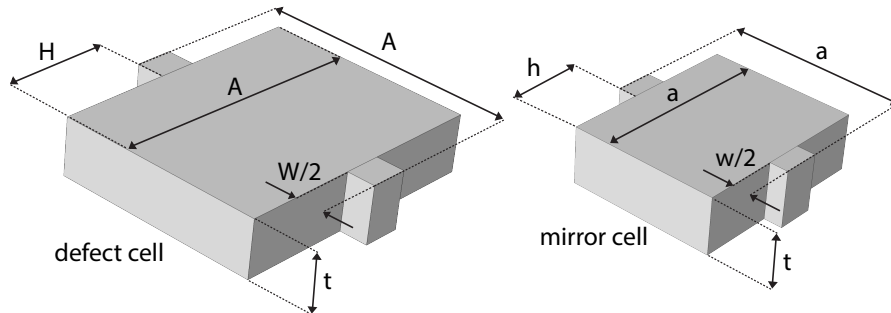


Figure A.1: Simulation geometry for the phononic defect resonator. The defect cell and mirror cell dimensions are $(A, H, W, t) = (1400, 600, 300, 300)$ nm and $(a, h, w, t) = (1000, 400, 200, 300)$ nm respectively.

Next we probe the acoustic admittance of the bound mode by simulating the defect site *only*, using fixed boundary conditions at its tethers. For the results shown in Fig. 3.3(f) in the main text, we set the resolution Δf of the frequency scans to 200 kHz in order to fully capture all the eigenmodes within the band of interest.

A.3 Foster synthesis for acoustic systems

A mechanical system with piezoelectric properties, when probed through electrical terminals, is indistinguishable from an ordinary microwave network — it can be fully described by an admittance function $Y(\omega)$. This has enabled the widespread adoption of mechanical devices as effective circuit elements in classical applications [19, 64, 51]. In this work, we use this insight to abstract away the mechanical aspect of the system and formulate a unified description *at the circuit level*, where calculating coupling rates and other quantities of interest is straightforward.

More precisely, given a linear lossless microwave network with known input admittance $Y_{11}(\omega)$, we would like to explicitly construct a network of capacitances and inductances that is described by the same admittance. Foster synthesis is a well-established technique [43] to do this construction. We begin by calculating the acoustic admittance function $Y_m(\omega)$ either analytically or numerically. For a passive, lossless network $Y_m(\omega)$ is a purely imaginary, monotonically increasing function [43]. This latter property implies that in general $Y_m(\omega)$ has an alternating sequence of poles and zeros, each corresponding to a resonance and anti-resonance of the network, respectively. A function of this kind can be written as a partial fraction expansion of the form

$$Y(s) = \sum_k \frac{R_k}{s - s_k} + Cs + D, \quad (\text{A.24})$$

where $s = i\omega + \kappa$ is a complex frequency, $\{s_k\}$ are the poles of $Y(s)$, and $\{R_k\}$ are the associated residues. We fit $Y_m(\omega)$ to a function of this kind using a well-established fitting routine [49] (see Fig. A.2 for an example of this procedure for the Lamb-wave resonator of Fig. 3.2).

The choice of synthesis is in general not unique. In this work, it is convenient to synthesize $Y_m(\omega)$ as a series combination of parallel inductances and capacitances, such as those shown in Figs. 3.1 and 3.3 in the main text. The self-resonance ω_k of each LC block then corresponds to a zero of $Y_m(\omega)$, and the capacitance C_k can be extracted through

$$C_k = \lim_{\omega \rightarrow \omega_k} \left\{ \frac{1}{2} \text{Im} [\partial_\omega Y_m(\omega)] \right\}, \quad (\text{A.25})$$

from which it follows that

$$L_k = \frac{1}{\omega_k^2 C_k}. \quad (\text{A.26})$$

For the two-mode analysis of the analytical model and the Lamb-wave resonator, there is an LC block with $L = \infty$ and $C = C_0$, the dc capacitance of the system (see Fig. 3.1 in the main text). This is absent in the black-box analysis [85] of multimode systems, because there the transmon inductance L_J is lumped into the network as well. To extract C_0 , we probe the dc response of the system by simulating the admittance spectrum from dc up to 50 MHz (Fig. A.2), where $\text{Im} [Y_m(\omega)]$

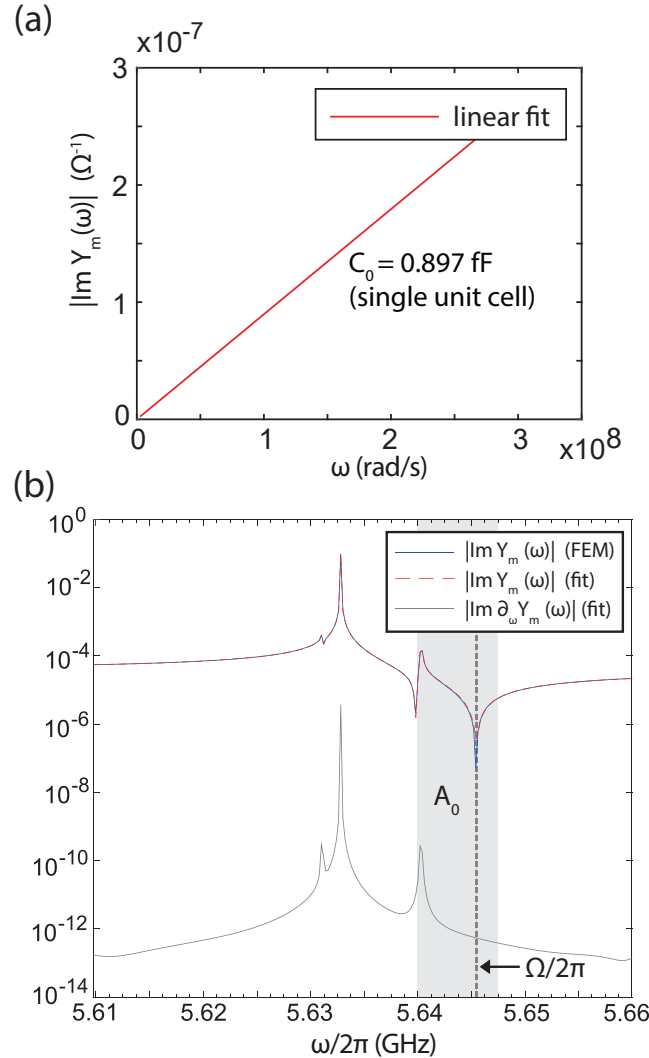


Figure A.2: Foster synthesis for the Lamb-wave resonator. (a) Low-frequency electroacoustic admittance, shown in the band $\omega/2\pi \in [0, 50]$ MHz. The slope of the line is the C_0 parameter of the network; (b) Admittance near the A_0 mode for $N_{\text{IDT}} = 1$ (also shown in Fig. 3.2(d) in the main text), including the fit to a rational function and its frequency derivative used to the extract network capacitances.

has a featureless linear dependence $\text{Im}[Y_m(\omega)] \sim i\omega C_0$ and C_0 is simply the slope,

$$C_0 = \lim_{\omega \rightarrow 0} \{\text{Im}[\partial_\omega Y_m(\omega)]\}. \quad (\text{A.27})$$

Appendix B

Supplementary information for Chapter 4: “Coupling a superconducting quantum circuit to a phononic-crystal-defect resonator”¹

B.1 Reflection spectra

We model the mechanical system as a collection of harmonic modes $\{\hat{b}_i\}$ linearly coupled to a Kerr oscillator, which in turn is coupled to a single input/output channel for driving and readout.

The Hamiltonian of the system is

$$\begin{aligned} \hat{H}/\hbar = & \omega_r \hat{a}^\dagger \hat{a} + \frac{\chi}{2} \hat{a}^{\dagger 2} \hat{a}^2 + \sum_k \omega_m^{(k)} \hat{b}_k^\dagger \hat{b}_k + \\ & \sum_k g_k (\hat{a} + \hat{a}^\dagger) (\hat{b}_k + \hat{b}_k^\dagger) - i\sqrt{\kappa_e} (\hat{a}^\dagger \alpha_{in} e^{-i\omega_d t} - h.c.) + \hat{H}_B, \end{aligned} \quad (B.1)$$

where ω_r is the frequency of the microwave mode, χ is the anharmonicity, $\{\omega_m^{(k)}\}$ are the frequencies of the mechanical modes, and $\{g_k\}$ are their coupling rates to the microwave mode. We have

¹This appendix is part of the following publication: P. Arrangoiz-Arriola, E.A. Wollack, M. Pechal, J.D. Witmer, J.T. Hill, A.H. Safavi-Naeini, “Coupling a superconducting quantum circuit to a phononic crystal defect cavity” *Phys. Rev. X* **8**, 031007 (2018)

explicitly included a coherent driving field at frequency ω_d (which couples to the system at rate κ_e) and bundled all other bath terms into \hat{H}_B — following a standard input-output treatment, these terms simply generate additional decay terms in the Heisenberg equations. We can eliminate the time dependence in \hat{H} by going into an interaction frame with respect to $\hat{H}_0/\hbar \equiv \omega_d (\hat{a}^\dagger \hat{a} + \sum_k \hat{b}_k^\dagger \hat{b}_k)$. The transformed Hamiltonian (now omitting the bath terms) becomes

$$\hat{H}/\hbar = -\Delta_r \hat{a}^\dagger \hat{a} + \frac{\chi}{2} \hat{a}^{\dagger 2} \hat{a}^2 - \sum_k \Delta_m^{(k)} \hat{b}_k^\dagger \hat{b}_k + \sum_k g_k (\hat{a} \hat{b}_k^\dagger + \hat{a}^\dagger \hat{b}_k) - i\sqrt{\kappa_e} (\hat{a}^\dagger \alpha_{in} - h.c.) , \quad (B.2)$$

where $\Delta_j \equiv \omega_d - \omega_j$.

We can neglect the nonlinear term in the weak-drive regime where $\chi |\alpha_{in}|^2 \ll \kappa^2$. Our experiment only measures the average output field amplitudes in steady state, given by $\langle \hat{a} \rangle \equiv \alpha$ and $\langle \hat{b}_k \rangle \equiv \beta_k$. These obey the Heisenberg equations of motion

$$\dot{\alpha} = \left(i\Delta_r - \frac{\kappa}{2} \right) \alpha - i \sum_k g_k \beta_k + \sqrt{\kappa_e} \alpha_{in} \quad (B.3)$$

$$\dot{\beta}_k = \left(i\Delta_m^{(k)} - \frac{\gamma_k}{2} \right) \beta_k - ig_k \alpha, \quad (B.4)$$

which can be written in the Fourier domain as

$$\frac{\kappa}{2} \chi_r^{-1}(\omega) \alpha = -i \sum_k g_k \beta_k + \sqrt{\kappa_e} \alpha_{in} \quad (B.5)$$

$$\frac{\gamma_k}{2} \chi_{m,k}^{-1}(\omega) \beta_k = -ig_k \alpha. \quad (B.6)$$

We define the bare dimensionless susceptibilities

$$\chi_r(\omega) = [-2i(\omega + \Delta_r)/\kappa + 1]^{-1} \quad (B.7)$$

$$\chi_{m,k}(\omega) = \left[-2i(\omega + \Delta_m^{(k)})/\gamma_k + 1 \right]^{-1}, \quad (B.8)$$

where $\kappa = \kappa_e + \kappa_i$ and $\{\gamma_k\}$ are the total decay rates of the microwave and mechanical modes, respectively. Together with the input-output boundary condition $\alpha_{out} = -\alpha_{in} + \sqrt{\kappa_e} \alpha$, we can then directly solve for the reflection coefficient $S_{11} \equiv \alpha_{out}/\alpha_{in}$, and obtain

$$S_{11}(\omega) = -1 + \frac{2\kappa_e/\kappa}{1 + \sum_k C_k \chi_{m,k}(\omega) \chi_r(\omega)} \chi_r(\omega), \quad (B.9)$$

where $C_k \equiv 4g_k^2/\kappa\gamma_k$ is the cooperativity (or readout efficiency) for mode k . We can finally assume that a single mechanical mode $\hat{b}_k \equiv \hat{b}$ is relevant at a given resonator frequency ω_r , in the sense that it is the only mode that imprints a measurable signature in the reflection signal. Some

algebraic manipulation leads us to the expression for $S_{11}(\omega)$

$$S_{11}(\omega) = -1 + \frac{2\kappa_e/\kappa}{1 + C\chi_m(\omega)\chi_r(\omega)}\chi_r(\omega), \quad (\text{B.10})$$

shown in the main text and used for fitting the data.

B.2 Wide-band characterization of SQUID array resonator

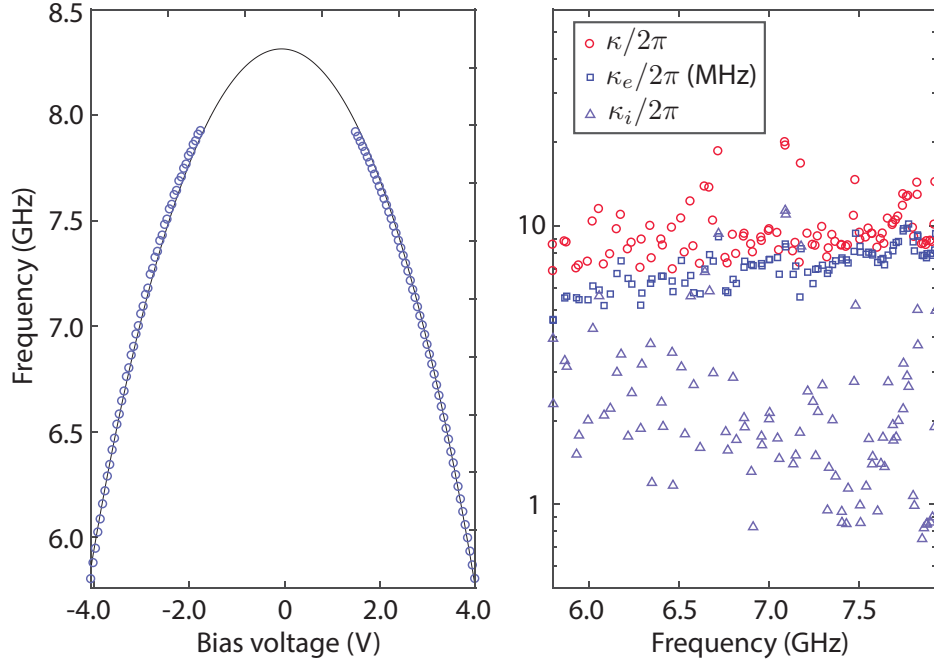


Figure B.1: Wide band resonator characterization. Calibration of the external flux as a function of the applied bias voltage (left), including data points (circles) and fit to theory. The flux sweet spot at $\omega_{r,\max} = 8.31$ GHz lies outside our measurement band. The total, extrinsic, and intrinsic linewidths (κ , κ_e , and κ_i , respectively) are also plotted as a function of frequency. A monotonic decrease in κ_i as the resonator is tuned towards the flux sweet spot may be due to a reduction in the flux noise contribution to the linewidth.

The center frequency of the SQUID array resonator is widely tunable, allowing us to probe the mechanical mode spectrum over a large range of frequencies. In Fig. B.1 we plot the resonator frequency $\omega_r/2\pi$ as a function of the bias voltage applied to run a current through the on-chip flux line (see Appendix B.5 for details) along with a fit to the function $\omega_r(V) = \omega_{r,\max}\sqrt{|\cos(GV + \phi_{\text{offset}})|}$, giving us a calibration of the external flux Φ_e threading the SQUIDs. We infer that the flux-insensitive point is at $\omega_{r,\max}/2\pi = 8.31$ GHz and lies outside of our measurement band. At every

bias point, we fit the reflection spectrum $S_{11}(\omega)$ to the model derived in Appendix B.1 (Eq. 4.2 with $g = 0$) in order to extract the total and extrinsic resonator linewidths (κ and κ_e , respectively), also shown in Fig. B.1. We also define an intrinsic linewidth $\kappa_i \equiv \kappa - \kappa_e$, which contains contributions from both energy relaxation and pure dephasing. Since our scattering parameter measurement uses only mean field amplitudes, we do not have the ability to separate these two contributions, but we can still look at the frequency dependence of κ_i in order to gain insight into the decoherence mechanisms affecting this device. We find that κ_e increases with frequency as expected from capacitive coupling to the feedline, whereas κ_i decreases as ω_r approaches the flux-insensitive point. This may be attributed to flux-noise dephasing. In fact, we see that at the mechanical frequency $\omega_m/2\pi \approx 6$ GHz the intrinsic linewidth is larger than it is at the flux sweet spot, suggesting that the coherence times in future experiments can be improved by operating the tunable circuits near this point.

B.3 Complete mechanical spectrum of the system

In addition to the mode at $\omega_m/2\pi = 5.9754$ GHz presented in the main text, we observe other modes distributed over a wide range of frequencies. In Fig. B.2 we show the complete mechanical spectrum of this device. The positions of all observed modes are indicated with vertical lines, and we plot the quality factor Q_m and coupling rate g of nine modes with sufficiently strong signatures in S_{11} to be fit reliably to the model. The mode presented in the main text is indicated in red. Interestingly, we find that *all* modes have quality factors on the order of 10^4 . This may be attributed to a combination of acoustic radiation, or “clamping loss”, and intrinsic material losses; more detailed studies of these devices will be needed in order to elucidate the relaxation mechanisms. However, it is possible that clamping loss is indeed dominant in these resonators as these measurements are consistent with previous studies of losses in phononic-crystal resonators made from silicon that lack complete phononic bandgaps [24]. The size of the bandgap in this work is not very large (< 5% of its center frequency according to our finite element simulations), which is of comparable magnitude to the fabrication-induced disorder in the phononic crystals. This allows trapped phonons to tunnel out of the defect region and irreversibly escape through the clamping points [24]. In order to suppress this loss channel, future devices will require larger bandgaps, which can be achieved through further improvements to the design and fabrication. We also observe that with the exception of mode presented in the main text — indicated by the red point at $g/2\pi \approx 1.6$ MHz — all modes have coupling rates on the order of 100 kHz. This reduction in the coupling rate has been observed in silicon optomechanical crystals as the modes are tuned outside of a bandgap region [2], and is supported by the numerical simulations presented in Appendix B.4. In our case, finite element simulations of all six resonator geometries present in this device predict rates in the range 1.5 – 2.5 MHz for localized modes of the “correct” polarization, leading us to conclude that only one resonance in the spectrum has such properties. The coupling rates can therefore be improved by

engineering resonators with larger bandgaps, optimizing the geometry of the defect, or changing the placement of the electrodes.

B.4 Finite-element simulations

In order to better understand the dense mechanical spectrum measured in this device, we perform finite-element simulations of the full phononic resonators, including their clamping to the Si substrate [1]. We include the effect of acoustic radiation by appropriate incorporation of perfectly matched layers at the clamping points. For the set of defect site lengths $a_{\text{def}} = \{1400, 1425, \dots, 1650\}$ nm, we solve for all the eigenmodes of these resonators in the approximate frequency range 6 - 6.6 GHz and calculate the mechanical energy stored in the defect site and normalize it to the total energy stored in the mode. This quantity gives a simple measure of the extent to which a mode is localized and is plotted as a function of mode frequency in Fig. B.3(a). The positions of complete and partial phononic bandgaps are indicated by dark grey and light grey shaded regions, respectively. Unsurprisingly, we see that as the defect length increases several modes shift to lower frequencies and enter the gap, becoming localized. Further, we note that modes entering the gap have different polarizations, so we mark with a filled square those with the “correct” polarization for this coupling electrode configuration. In these simulations, only two such modes become localized for the fabricated defect designs, one for $a_{\text{def}} = 1400$ nm and one for $a_{\text{def}} = 1600$ nm.

It is also helpful to understand how various kinds of modes present in these simulated spectra couple to the microwave resonator via the electrodes. The coupling rate g depends on the extent to which the driving electric field and the polarization field in the crystal overlap. Therefore modes that lie outside of the bandgap and are not well localized to the defect will tend to have a smaller g than highly localized modes. For the same reason modes of different polarization will have different g , even if they are localized to a similar region. We illustrate this in Fig. B.3(b), where we show the mode profiles (electrostatic potential) of the three modes indicated in Fig. B.3(a): (1) a localized mode with the wrong polarization, (2) a localized mode with the correct polarization, and (3) a delocalized mode with the correct polarization. We also indicate their simulated coupling rates for this particular resonator design, which were calculated using the technique discussed in Ref. [6]. Together with the simulated mode distributions of Fig. B.3(a), these numerical results help explain why we observe a dense mechanical spectrum in our device but only a single mode with a large g .

B.5 Experimental setup

Our sample is packaged in a copper enclosure to protect it from stray radiation and limit spurious modes. The package is placed inside a multi-layer magnetic shield anchored to the mixing-chamber plate ($T \approx 7$ mK) of a cryogen-free dilution refrigerator. A Rhode & Schwartz ZNB20 vector network

analyzer (VNA) generates a probe tone that is sent down to the input port of the device through a cascade of attenuators thermalized to various temperature stages of the refrigerator. A circulator (QuinStar QCY-060400C000) separates the input and output signals and an additional isolator (QuinStar QCY-060400C000) protects the device from hot ($T \sim 3\text{ K}$) radiation in the output line. The output signal is routed up to the 3 K stage through superconducting NbTi cables, where it is amplified by a high-electron mobility transistor (HEMT) amplifier (Caltech CITCRYO1-12A). The signal is further amplified at room temperature by two low-noise amplifiers (Miteq AFS4-02001800-24-10P-4 & AFS4-00100800-14-10P-4) with a 4-8 GHz bandpass filter (Keenlion KBF-4/8-Q7S) between them before being detected at the VNA.

Flux biasing is provided by a programmable voltage source (SRS SIM928). The DC voltage passes through a cold low-pass filter (Aivon Therma-24G) at the 3 K stage and enters the DC port of a bias tee (Anritsu K250) mounted at the mixing-chamber plate. In addition an AC flux can be applied with a microwave generator (Keysight E8257D), which sends a tone to the RF port of the bias tee through an additional attenuated line, though this capability is not used in this experiment. Finally, the DC+RF output of the tee is sent directly to the flux port of the device.

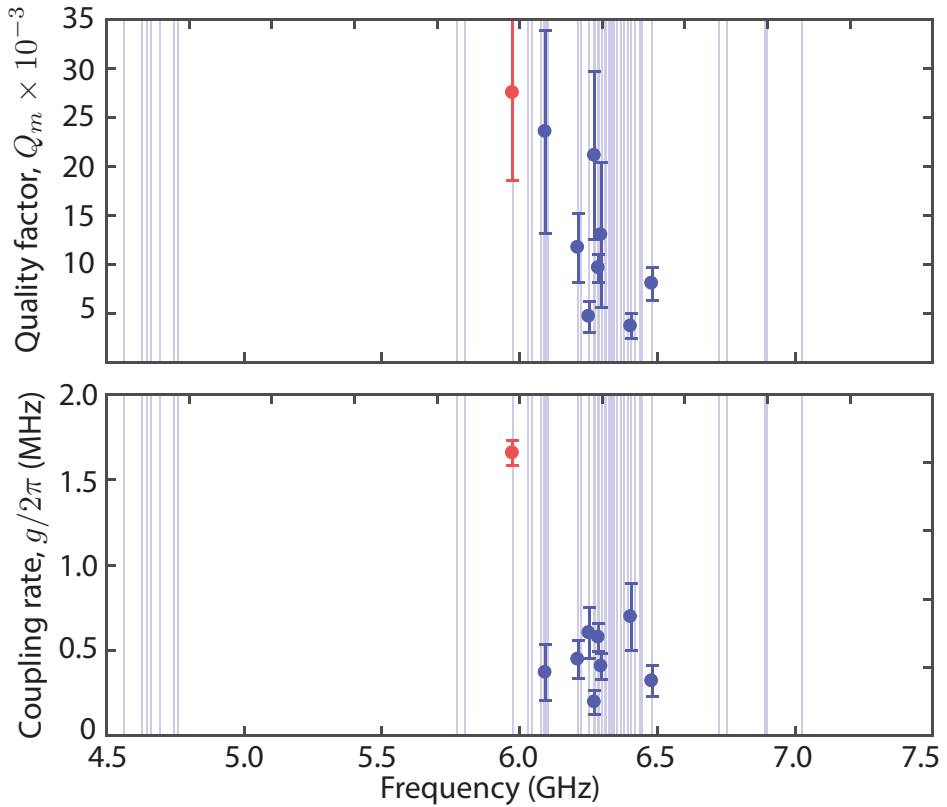


Figure B.2: Mechanical spectrum. Quality factors Q_m (top) and coupling rates g (bottom) of various modes are plotted as a function of frequency. The position of all modes observed in this device are indicated by vertical blue lines, clearly showing that the resonances tend to tightly cluster within certain regions. All of these resonances were verified to be linear in the same way as the mode presented in the main text, ruling out TLS resonances. In both plots, the resonance at $\omega_m/2\pi = 5.975$ GHz presented in the main text is indicated by the red point. The quality factors and coupling rates are obtained through reflection spectra collected at various detunings $\Delta = \omega_r - \omega_m$ around each mechanical mode and fitting them to Eq. 4.2; error bars indicate the standard deviation of the parameter estimates for these fits.

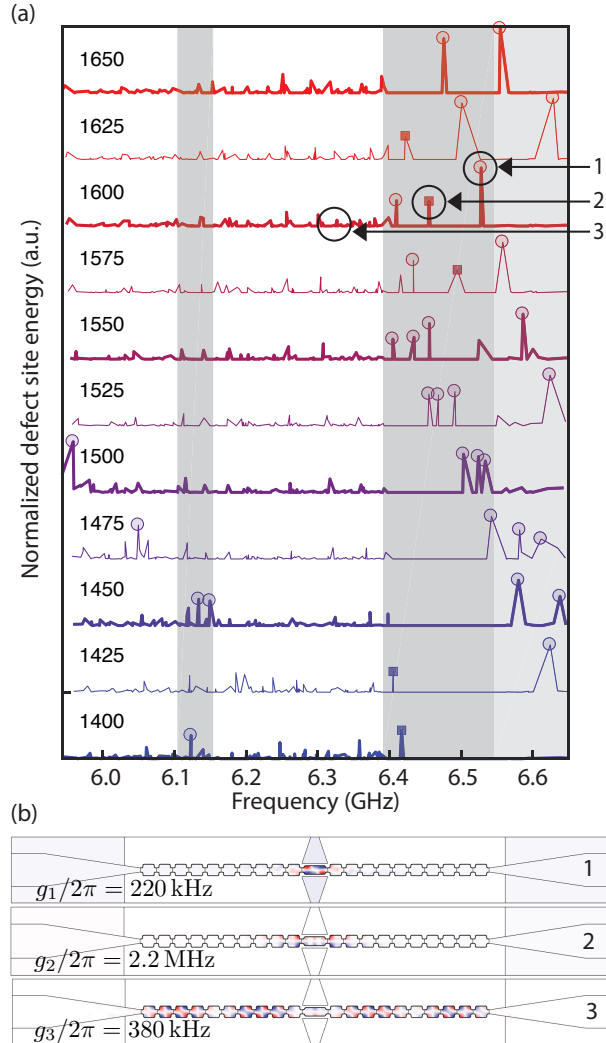


Figure B.3: Simulated mechanical spectra. (a) Eigenfrequency simulation results for resonators with defect lengths $a_{\text{def}} = \{1400, 1425, \dots, 1650\}$ nm. The normalized defect site energies (which are unitless and range from 0 to 1) are plotted for all the modes in the frequency range 6 - 6.6 GHz, with the bold lines corresponding to the fabricated defect lengths. The mirror cell design is the same as that used for the band diagram of Fig. 4.1(a); here the position of the complete and partial phononic bandgaps are indicated with dark grey and light grey regions. Modes with defect energy > 0.3 are considered ‘localized’ and are marked with a circle, and localized modes with the correct polarization are marked with a filled square. We see that as the defect length is increased several modes shift into the bandgap and become localized, but only a small fraction of them have the correct polarization. (b) Electrostatic potential of the three modes labeled in (a), which have distinct profiles and coupling rates. Only modes that have the right polarization and are localized have simulated coupling rates that exceed 1 MHz.

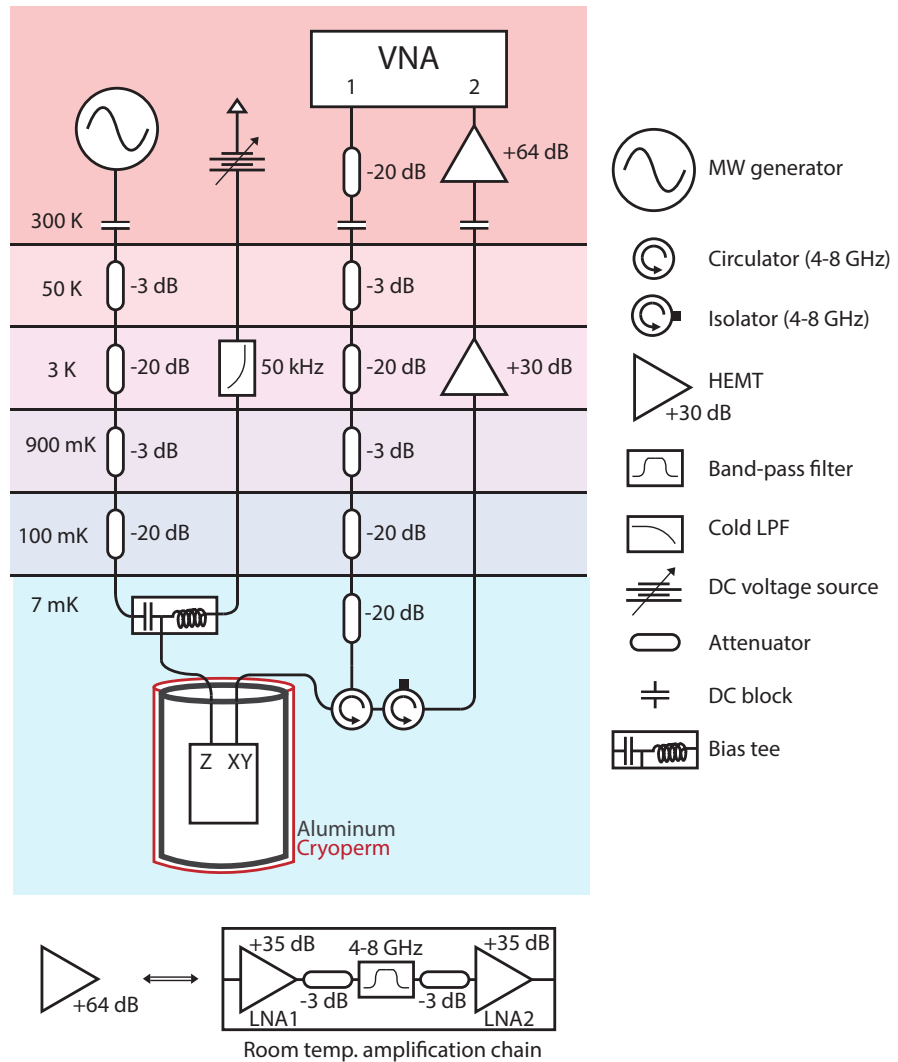


Figure B.4: Experimental setup schematic. The sample is placed inside a multilayer magnetic shield (2.5 mm-thick aluminum and 1 mm-thick Cryoperm [MuShield, Inc.]) at the mixing chamber plate of a dilution refrigerator with base temperature $T \approx 7\text{ mK}$. The measurement and control electronics for probing the scattering parameters and applying a flux bias are illustrated.

Appendix C

Supplementary information for Chapter 5: “Resolving the energy levels of a nanomechanical oscillator”¹

C.1 Device fabrication

Our fabrication process begins with a 500-nm film of lithium niobate (LN) on a 500- μm high-resistivity ($\rho > 3 \text{ k}\Omega \cdot \text{cm}$) silicon substrate. The LN film is first thinned to approximately 250 nm by blanket argon milling. We then pattern a mask on negative resist (HSQ) with electron-beam (e-beam) lithography and transfer it to the LN with an angled argon milling step [128]. After stripping the resist, we perform a thorough acid clean in order to remove re-deposited amorphous LN. This is critical, as any remaining residue significantly lowers the quality of the electrodes deposited in a later step. Next, we define the aluminum ground plane, feedlines, and transmon capacitor on the exposed silicon substrate with photolithography, electron beam evaporation, and liftoff. The Al/AlO_x/Al Josephson junctions are then formed using a standard Dolan bridge technique and double-angle evaporation [38, 57]. Following junction growth, we deposit 50-nm aluminum electrodes directly on top of the phononic crystals in order to couple the defect modes to the qubit. This liftoff mask is patterned using e-beam lithography with \sim 10-nm alignment precision to the existing LN structures.

¹This appendix is part of the following publication: P. Arrangoiz-Ariola*, E. A. Wollack*, Z. Wang, M. Pechal, W. Jiang, T. P. McKenna, J. D. Witmer, R. Van Laer, A. H. Safavi-Naeini, “Resolving the energy levels of a nanomechanical oscillator” *Nature* **571**, 537-540 (2019). *These authors contributed equally.

Parameter(s)	Value(s)
$\omega_{\text{ge}}^{(\text{max})} / 2\pi$	2.417 GHz
$\alpha / 2\pi$	138 MHz
T_1	1.0 - 1.4 μ s
$\gamma / 2\pi$	600 kHz
$\{\omega_m^{(i)}\} / 2\pi$	2.405, 2.257, 2.153, 2.065, 2.002 GHz
$\{g_i\} / 2\pi$	15.7, 15.2, ~14, 14.2, ~13 MHz
$\kappa / 2\pi$	370 kHz
$\chi / 2\pi$	-1.56 MHz
$\omega_r / 2\pi$	3.026 GHz
$\kappa_r / 2\pi$	1.3 MHz

Figure C.1: **Device parameters.** Parameters of the qubit, strongly coupled mechanical modes, and readout resonator.

In the final metallization step, we evaporate aluminum bandages which form superconducting connections between the qubit capacitor, electrodes, junctions and ground plane [39]. The bandages are 500 nm thick in order to smoothly connect the phononic crystal electrodes — resting on the 250-nm LN film — with the qubit capacitor and ground plane below. After dicing the sample into individual chips, the LN structures are released with a masked XeF_2 dry etch that attacks the underlying silicon with high selectivity [124]. Finally, the release mask is stripped in solvents and individual chips are packaged for low-temperature measurement.

C.2 Device parameters

Table C.1 gives device parameters for the qubit, the five strongly coupled mechanical modes, and the coplanar waveguide readout resonator. The maximum qubit frequency $\omega_{\text{ge}}^{(\text{max})}$ is extracted from a fit to the flux tuning curve, $\omega_{\text{ge}}(\Phi_e) = \omega_{\text{ge}}^{(\text{max})} \sqrt{|\cos(\pi\Phi_e/\Phi_0)|}$, where Φ_e is the externally applied magnetic flux and Φ_0 is the magnetic flux quantum. The transmon anharmonicity $\alpha = \omega_{\text{ge}} - \omega_{\text{ef}}$ can also be extracted from the flux tuning curve, and we confirm this value with a separate two-tone measurement of the $|g\rangle \rightarrow |e\rangle$ and $|e\rangle \rightarrow |f\rangle$ transitions. Additionally, the qubit is characterized by its energy relaxation time, T_1 , and its total linewidth, γ . These parameters were measured using techniques described in Methods, from which we obtain an estimate for the dephasing time T_ϕ through $\gamma = 1/2T_1 + 1/T_\phi$. The five strongly coupled mechanical modes are characterized by

their resonant frequencies $\{\omega_m^{(i)}\}$ and their coupling rates $\{g_i\}$ to the qubit, which are obtained by measuring the normal mode splittings in the flux tuning dataset (Fig. 3a of the main text). We note that the extraction of g_3 and g_5 is complicated by the presence of additional weakly coupled modes. The decay rate κ of the mechanical mode $\omega_m^{(1)}$ (used for the number splitting experiment) was obtained via a ringdown measurement similar to a qubit T_1 measurement (see Methods). Finally, χ is the dispersive coupling rate between the transmon and the mechanical mode at the detuning $\Delta = \omega_{ge} - \omega_m^{(1)}$ used in the experiment, $\Delta/2\pi = -88$ MHz. We also list the frequency ω_r and linewidth κ_r of the readout resonator.

C.3 Qubit and mechanical oscillator control

The experimental setup is shown in Fig. C.2. In these experiments, we generate all qubit and phonon excitation pulses using a 5 GS/s arbitrary waveform generator (AWG) (Tektronix series 5200). Because the qubit has a relatively low transition frequency ($\omega_{ge}/2\pi \approx 2.4$ GHz), the pulses are produced directly using the instrument's built-in digital IQ mixer without further need for upconversion. The AWG output is then low-pass filtered at room temperature to remove Nyquist images, spurious intermodulation signals, and clock bleedthrough. We use a separate AWG channel to generate the phonon excitation pulses, which are then combined with the qubit pulses at room temperature. Once in the cryostat, the signals are attenuated and filtered at various temperature stages before being routed to the qubit through a dedicated charge line on the device (labeled *XY* in Fig. C.2). Flux biasing is performed using a programmable voltage source (SRS SIM928), which is low-pass filtered at the 3 K stage (Aivon Therma-24G) and at the 7 mK stage; the DC signal is then sent to an on-chip flux line (labeled *Z* in Fig. C.2).

C.4 Qubit readout

The qubit state is read out dispersively via a superconducting coplanar waveguide resonator [127]. Square-envelope readout pulses are generated directly by the AWG with a carrier frequency of $\omega_r/2\pi = 3.026$ GHz, roughly matching the resonance frequency of the readout resonator. One end of the resonator is capacitively coupled to the qubit, while the other end is inductively coupled to a through-feedline with a coupling rate $\kappa_r/2\pi = 1.3$ MHz. After passing through two isolators (Quinstar QCY-030150S000), the signal is amplified at 3 K by a high electron mobility transistor (HEMT) amplifier (Caltech CITCRYO1-12A), and at room temperature by two low-noise amplifiers (Miteq AFS4-02001800-24-10P-4 and AFS4-00100800-14-10P-4). Next, the signal is down-converted to an intermediate frequency (IF) of 125 MHz using a separate local oscillator (Keysight E8257D), and a double-balanced mixer (Marki ML1-0220I). Finally, the IF signal is amplified, low-pass filtered, and digitized by an acquisition card (AlazarTech ATS9350) with 12-bit resolution and a 500 MS/s

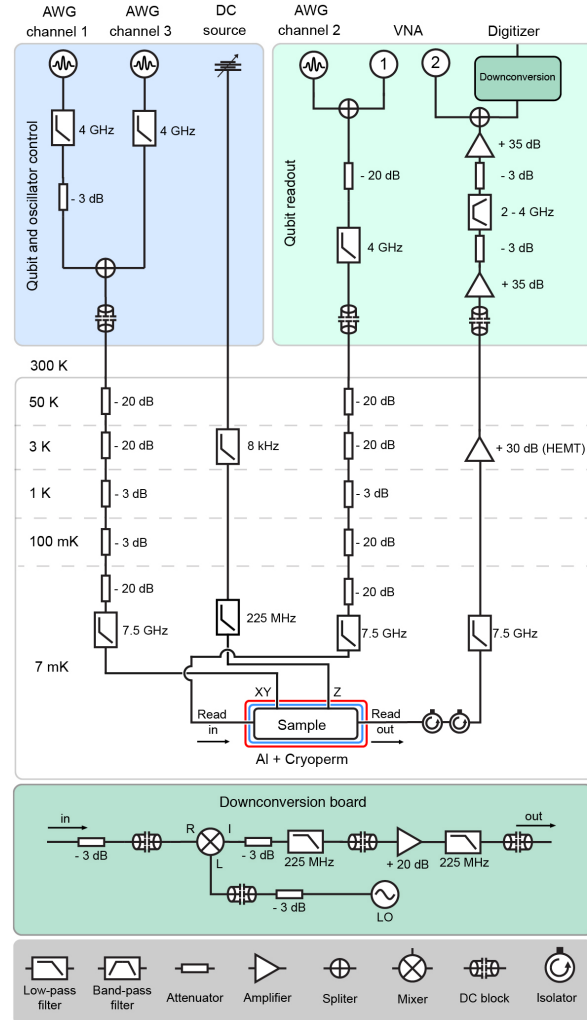


Figure C.2: **Fig. C.2 | Experimental setup.** The sample is located at the mixing-chamber plate of a dilution refrigerator, packaged in a microwave PCB and copper enclosure, and surrounded by cryogenic magnetic shielding. All instruments are phase-locked by a 10 MHz rubidium frequency standard (SRS SIM940).

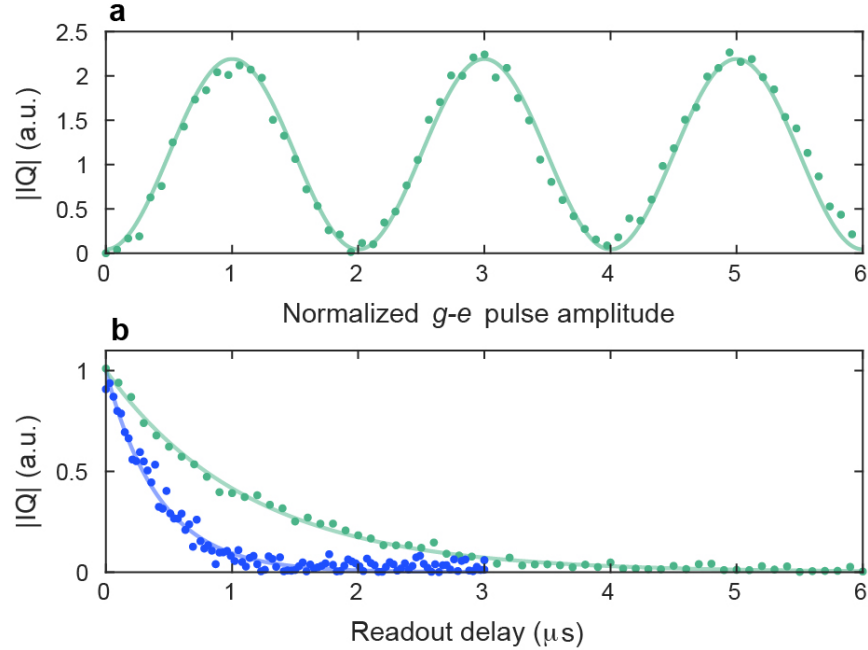


Figure C.3: **Characterization of qubit and mechanical modes.** **a**, Rabi oscillation measurement used to calibrate the qubit excitation pulses. **b**, Energy relaxation of qubit (green) and mechanics (blue), with lifetimes $T_1 = 1.14 \mu\text{s}$ and 430 ns, respectively. This measurement of the qubit T_1 time was obtained at $\omega_{\text{ge}}/2\pi = 2.301 \text{ GHz}$. At this same frequency, we perform the ringdown measurement of the mechanical mode at $\omega_m^{(1)}/2\pi = 2.405 \text{ GHz}$.

sampling rate. The data is first stored on-board and then transferred to a GPU for real-time processing. Additionally, a vector network analyzer (Rhode & Schwarz ZNB20) is used in the readout chain in order to calibrate the frequency of the readout pulses.

C.5 Characterization of qubit and mechanics

As described in Methods, the system is driven through the transmon XY line at a time-dependent Rabi rate $\Omega(t) = \Omega_0 f(t)$, where $f(t)$ is a normalized pulse envelope and $\Omega_0 = A_k V_d$ is directly proportional to the drive voltage V_d . The conversion factor A_k , with $k = 1, 3$ depends on which AWG channel is used to drive the qubit (see Fig. C.2), and varies with frequency. We first calibrate the qubit excitation pulses through a Rabi oscillation measurement with the qubit at $\omega_{\text{ge}}/2\pi = 2.318 \text{ GHz}$, the frequency at which we performed the number splitting measurements (see Fig. C.3a). Here we use gaussian pulses $f(t) = \exp(-t^2/2\sigma_t^2)$ of width $\sigma_t = 50 \text{ ns}$ and varying amplitude $\Omega_0(V_d) = A_1 V_d$. From this data, we extract $A_1 = 2\pi \times 93.9 \text{ MHz/V}$. We infer $A_3 \approx \sqrt{2}A_1$ from the presence of the extra 3 dB attenuator.

In order to measure the qubit energy relaxation time, T_1 , we use the calibration to choose an appropriate π -pulse amplitude and approximately prepare the qubit in the excited state, $|e\rangle$. We then measure the excited state population (Fig. C.3b) as we vary the delay between preparation and readout. The resulting data is fit to an exponential to extract T_1 . We perform this measurement at a variety of qubit frequencies, all sufficiently separated from the strongly coupled mechanical modes, and measure relaxation times in the range $T_1 = 1.0 - 1.4 \mu\text{s}$. In addition, we perform steady-state spectroscopy with the qubit at the frequency of the number splitting experiment in order to extract the total qubit linewidth, $\gamma/2\pi \approx 600 \text{ kHz}$.

We perform a ringdown measurement to extract the decay rate κ of the mechanical mode used for the phonon-number splitting experiment. Here, the qubit is first detuned by an amount $\Delta \gg g$ in order to avoid hybridizing the modes (see Supplementary Information), and we then send a nearly resonant pulse at frequency $\omega_d \approx \omega_m^{(1)}$ in order to excite the mechanical mode. The mean mechanical occupation $\langle \hat{b}^\dagger \hat{b} \rangle$ shifts the readout resonator through a small cross-Kerr interaction induced by the qubit. We therefore use this shift as an approximate measure of the occupation in the same way the excited state population of the qubit is measured. Sweeping the delay between excitation and readout produces the ringdown curve shown in Fig. C.3b, with a decay rate $\kappa/2\pi = 370 \text{ kHz}$ corresponding to an energy relaxation time $\kappa^{-1} = 430 \text{ ns}$.

All the parameter estimates obtained from these characterization measurements are later used in the numerical simulations of the pulse sequence, discussed in Supplementary Information.

C.6 Pulse sequence

The phonon-number splitting data was obtained using a pump-probe scheme in which a short phonon excitation pulse is sent at the mechanical frequency ω_m and is immediately followed by a weak spectroscopy pulse. These pulses are generated with separate AWG channels and are later combined before entering the cryostat (see Methods). Both pulses have cosine-shaped envelopes of the form $V(t) = V_0[1 - \cos(2\pi t/\tau)]/2$, which are synthesized at a baseband frequency of $\nu_{\text{IF}} = 125 \text{ MHz}$ and then digitally upconverted to their final carrier frequencies. For all the number splitting measurements, the length of the phonon excitation pulse is held fixed at $\tau_{\text{mech}} = 175 \text{ ns}$, while its voltage is varied to prepare states with different mean phonon numbers $\langle \hat{b}^\dagger \hat{b} \rangle$. The length and voltage of the qubit spectroscopy pulse are respectively set to $\tau = 1.5 \mu\text{s}$ and $V_0 = 7.5 \text{ mV}$, corresponding to a Rabi rate $\Omega_0/2\pi \approx 700 \text{ kHz}$ (see Methods for details on pulse calibration). We separately verified that these pulse settings do not result in power broadening of the qubit line. Immediately following the spectroscopy pulse, a $2-\mu\text{s}$ square-envelope pulse is sent to the readout port of the device. We measure the I and Q quadratures of the scattered pulse and subtract the reference values I_0 and Q_0 recorded with the system in the ground state. The resulting signal is then an indirect measure of the excited state population.

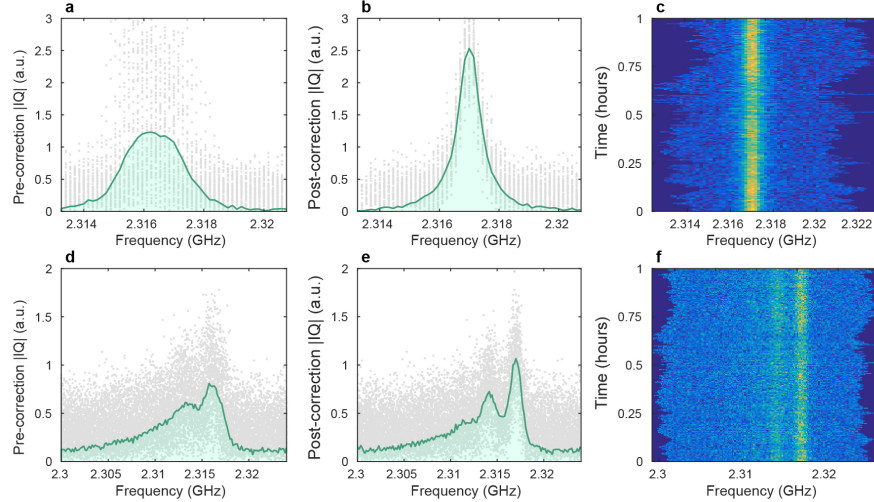


Figure C.4: Qubit frequency tracking. **a**, Raw qubit tracking spectrum, 1 hour elapsed time. First, the bare qubit spectrum is averaged over a 20 s interval, with a full spectral measurement performed every ~ 1 ms; all of the raw 20 s tracking spectra taken during the hour-long experiment are overlaid (gray circles). Then these spectra are averaged without post-processing to obtain the effective bare qubit spectrum (green curve), resulting in an effective linewidth ~ 2.8 MHz. **b**, Qubit tracking spectrum with post-processing. Here, we show the same qubit spectra as found in (a), but each 20 s tracking spectrum is aligned to the average qubit frequency using post-processing peak detection. The effective qubit linewidth is now improved to ~ 1.1 MHz. **c**, Alignment of bare qubit spectra through time. Each horizontal slice represents a 20 s tracking spectrum, showing that the qubit drifts by ± 1.5 MHz during the experiment. **d**, Raw phonon-number splitting spectrum. We interleave number splitting measurements between the tracking spectra taken in (a), alternating between the two every ~ 0.5 ms. When all of the raw spectra (grey points) are averaged without frequency correction (green curve), number splitting is visible but the peaks are poorly resolved. **e**, Post-processed phonon-number splitting spectrum. Using the frequency corrections calculated in (b), we adjust the frequencies of each slice of (d) and improve the resolution of the peaks. **f**, Alignment of phonon-number splitting spectra through time. The zero- and one-phonon peaks are easily visible with a splitting $2\chi \approx 3$ MHz.

C.7 Flux drift correction and qubit tracking

Our experiment uses a frequency-tunable transmon qubit that is tuned away from its flux sweet spot, making it susceptible to flux noise and drift. We take several precautions to reduce drift in the qubit frequency induced by variations in the environmental magnetic field. These include low-temperature magnetic shielding, vibrational isolation, and low-pass filtering the DC flux bias. Nonetheless, some of the data presented took more than one hour of averaging to record. The slow drift in the qubit frequency, on the order of the linewidth of the qubit over one hour, smears out the peaks, which we correct for in post-processing.

The drift correction scheme is accomplished by alternating between measurements of the qubit

frequency and the number splitting spectrum (Fig. C.4), and using the qubit frequency as a reference to align the number splitting data for averaging. This is done by creating a two-part AWG sequence: in the first part of the sequence, we measure the qubit spectroscopic line in a narrow window around the expected (noise-less) qubit frequency while the mechanical system is left unexcited. The next part of the sequence performs the number splitting measurement, i.e. phonon excitation followed by qubit spectroscopy. The resulting IQ averages are returned for data collection every 20 s. In post-processing, the frequency drift is extracted from the qubit tracking spectrum, then used to offset the number splitting data. This scheme is able to reduce the apparent qubit linewidth from 2.8 MHz to 1.1 MHz during an hour-long measurement, allowing us to compensate for slow (sub-Hz) flux drift and improve resolution of the phonon-number states (Fig. C.4).

We note that fluctuations in the qubit frequency cause small ($\sim 1.5\%$) changes in the qubit-phonon detuning $\Delta = \omega_{\text{ge}} - \omega_{\text{m}}$, which in turn cause dispersion in χ . Namely, for small changes $\delta\Delta$ in the detuning, we expect variations $\delta\chi$ in the dispersive shift per phonon of order

$$\frac{\delta\chi}{\chi} \simeq - \left(\frac{2\Delta - \alpha}{\Delta - \alpha} \right) \frac{\delta\Delta}{\Delta}. \quad (\text{C.1})$$

Over the duration of the number splitting measurements, we estimate that the peak-to-peak splitting varies by up to 75 kHz ($\delta\chi/\chi \approx 2.5\%$) given our operating parameters. Although this effect is small, it is preferable to reduce flux noise by more direct measures — post-processing can only improve the spectral clarity of phonon-number peaks to the extent that $\delta\chi \ll \gamma, \kappa$. One solution is to move to fixed-frequency qubits and use the ac-Stark shift for frequency control as done in other quantum acoustics experiments [27].

C.8 Phononic-crystal resonator design

As described in the main text, the mechanical resonators used in this work are one-dimensional phononic-crystal resonators; each resonator is formed by introducing a single defect site to an artificial lattice that is patterned onto the LN. This localizes a set of vibrational modes at the defect site, provided the modes lie within the bandgap of the surrounding lattice. More practically, this configuration can be thought of as a wavelength-scale resonator surrounded by acoustic “Bragg mirrors”. Each unit cell of the mirror region is comprised of a square-shaped block of LN uniformly covered by a 50-nm aluminum layer. As shown in Fig. C.5a, the mirror cell is parameterized by its lattice constant a , strut length s_l , and strut width s_w . Additionally, there are other geometric parameters which we cannot tightly control during fabrication, such as the LN thickness t_{LN} , sidewall angle θ_{sw} , and corner fillet radius R . We numerically simulate [1] the eigenmodes of the mirror cell using Floquet boundary conditions, sweeping the wavevector k over the first Brillouin zone $k \in [0, \pi/a]$. This produces a band diagram such as the one shown in Fig. C.5b, where we used the same set of

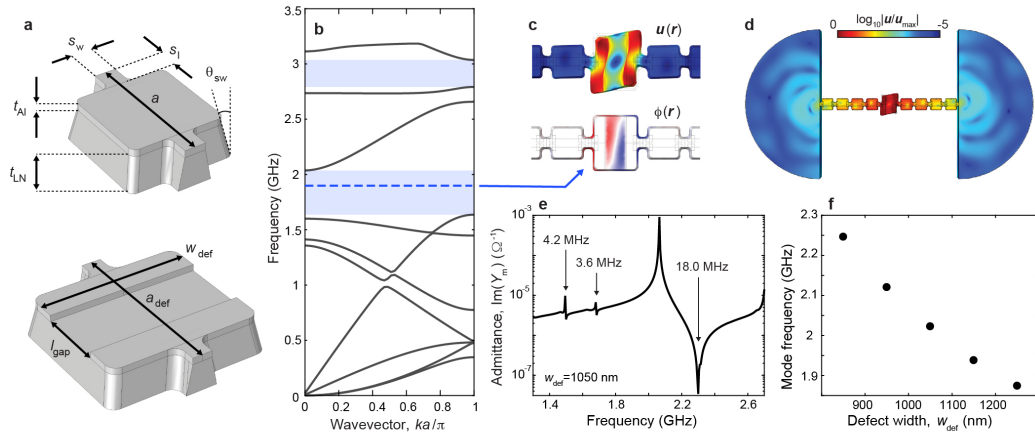


Figure C.5: Phononic-crystal resonator design. **a**, Simulation geometries of the mirror cell (top) and defect cell (bottom). **b**, Complete band diagram (including all polarizations and symmetries) of the mirror regions. A bandgap over the range $\sim [1.6, 2.0]$ GHz is clearly visible. For these simulations we use the same mirror cell parameters as those of the fabricated devices: $a = 1 \mu\text{m}$, $s_l = 330 \text{ nm}$, $s_w = 150 \text{ nm}$, $t_{\text{Al}} = 50 \text{ nm}$, $t_{\text{LN}} = 230 \text{ nm}$, and $\theta_{\text{sw}} = 11^\circ$. The discrepancy between the observed and simulated bandgap positions is not understood and could be attributed to a number of factors, including possible differences in the material constants of our LN films and those used for the simulations. **c**, Deformation $\mathbf{u}(\mathbf{r})$ (top) and electrostatic potential $\phi(\mathbf{r})$ (bottom) of a localized defect mode at $\nu \approx 1.9$ GHz. Here we use $a_{\text{def}} = 1.3 \mu\text{m}$, $w_{\text{def}} = 1.25 \mu\text{m}$, and $l_{\text{gap}} = 500 \text{ nm}$. The mode deformation is predominantly polarized in the plane of the phononic crystal, and the polarization generated by the piezoelectricity in LN is predominantly aligned along the direction of the electric field produced by the electrodes, as is evident by the electrostatic potential. **d**, Deformation of the same mode as that in (c), with a view of the entire resonator. The color indicates $\log_{10} |\mathbf{u}(\mathbf{r})|/|\mathbf{u}_{\max}|$, illustrating that even with $N = 4$ mirror cells the mode is tightly localized to the defect region. In the measured devices, $N = 8$. **e**, Imaginary part of the electromechanical admittance $Y_m(\omega)$, obtained from finite-element simulations of the structure shown in **d**. Using Foster synthesis we extract the coupling rates g of each of the modes associated with the pole/zero pairs that are visible in the response. **f**, Frequency of the strongly coupled modes, as a function of w_{def} . Their distribution (though not their absolute values) agrees fairly well with that of the observed modes.

mirror cell parameters as those of the fabricated device. The diagram shows all possible bands of the structure within the frequency range of interest — including all polarizations and symmetries — and exhibits a clear phononic bandgap over the range $\sim [1.6, 2.0]$ GHz. This gap is similar in size to that observed in the experiment (~ 400 MHz) but is centered at a lower frequency, which could be due to differences in the material properties of our films and those used for the simulations. As a final step, we verify the robustness of the phononic bandgap to variations in the mirror cell parameters in order to ensure that fabrication-induced fluctuations will not drastically alter the size or position of the gap.

The defect cell is created by stretching the local lattice constant to a larger value $a_{\text{def}} > a$ and introducing a break in the aluminum metallization, effectively forming a pair of electrodes separated by a gap l_{gap} (Fig. C.5a). This configuration supports modes that lie within the phononic bandgap and are therefore localized to the defect site (Fig. C.5c, d). Through the piezoelectric effect, the strain S_{jk} associated with each mode induces a polarization $P_i = e_{ijk}S_{jk}$ in the crystal, where e_{ijk} is the piezoelectric coupling tensor. The modes of the structure can couple strongly to the qubit if the polarization field P overlaps with the electric field of the electrodes and is predominantly aligned along the same direction. Our devices are fabricated on X-cut LN, with the direction of propagation of the phononic crystals pointing along the Y crystal axis. This orientation allows for defect modes that have the ‘correct’ polarization, as shown in Fig. C.5c. Using the techniques outlined in Ref. [6], we calculate coupling rates $g/2\pi \approx 20 - 22$ MHz for the fabricated defect geometries, in modest ($\delta \sim 30\%$) agreement with our measurements (Fig. C.5e). In addition, the defects generally support other localized modes which do not couple as strongly ($g/2\pi \lesssim 5$ MHz).

The device used in this experiment contains an array of five resonators that have the same mirror design, but different values of the defect width w_{def} . As discussed earlier, each resonator supports a small number of localized modes (Fig. C.5e), but only one of them has the correct polarization. In Fig. C.5f we show the simulated frequencies of such modes for the values of w_{def} used in our device. These simulation results clearly show that the five strongly coupled modes we observe each correspond to a separate resonator in the array, and also explain the origin of additional weakly coupled modes present in the spectrum.

C.9 Supplementary data

We made another set of phonon-number splitting measurements, the results of which are shown in Supplementary Figure S1. These measurements were done with the same mechanical resonator.

C.10 Numerical simulations of qubit spectra

C.10.1 System Hamiltonian

We model the transmon as a nonlinear mode at frequency ω_{ge} with anharmonicity α , and the mechanical oscillator as a linear mode at frequency ω_{m} . The two systems are coupled linearly at a rate g and are driven via the transmon at a time-dependent Rabi rate $\Omega(t)$. In a frame rotating at the drive frequency ω_{d} , the total Hamiltonian can be written as $\hat{H} = \hat{H}_0 + \hat{H}_{\text{d}}$, with

$$\hat{H}_0 = \Delta_{\text{ge}} \hat{a}^\dagger \hat{a} - \frac{\alpha}{2} \hat{a}^\dagger \hat{a}^\dagger \hat{a} \hat{a} + \Delta_{\text{m}} \hat{b}^\dagger \hat{b} + g(\hat{a} \hat{b}^\dagger + \hat{a}^\dagger \hat{b}), \quad (\text{C.2})$$

$$\hat{H}_{\text{d}} = \frac{1}{2}(\Omega(t) \hat{a} + \Omega^*(t) \hat{a}^\dagger), \quad (\text{C.3})$$

where \hat{a} and \hat{b} are the annihilation operators for the transmon and mechanical modes, respectively, and $\Delta_i := \omega_i - \omega_{\text{d}}$. While transforming to this frame, counter-rotating terms of the form $\hat{a} \hat{b} e^{-2i\omega_{\text{d}} t}$ are neglected. In the dispersive limit, where both $g/|\Delta| \ll 1$ and $g/|\Delta - \alpha| \ll 1$, with $\Delta := \omega_{\text{ge}} - \omega_{\text{m}}$, Eq. C.2 reduces to an effective Hamiltonian

$$\hat{H}_{0,\text{eff}} = \Delta_{\text{ge}} \hat{a}^\dagger \hat{a} + \Delta_{\text{m}} \hat{b}^\dagger \hat{b} + 2\chi \hat{a}^\dagger \hat{a} \hat{b}^\dagger \hat{b} \quad (\text{C.4})$$

that is diagonal in the number basis of both systems [60]. The dispersive coupling rate χ is related to the original system parameters through

$$\chi = -\frac{g^2}{\Delta} \frac{\alpha}{\Delta - \alpha}. \quad (\text{C.5})$$

This effective Hamiltonian explicitly reveals the dependence of the qubit frequency on the number of phonons $\hat{n} = \hat{b}^\dagger \hat{b}$, with $\omega_{\text{ge}}(\hat{n}) = \omega_{\text{ge}} + 2\chi \hat{n}$. In particular, we expect to observe phonon-number splitting of the qubit spectroscopic line if $|2\chi| \gg \max\{\gamma, \kappa\}$, when the splitting exceeds the largest of the qubit and mechanical linewidths (γ and κ , respectively). In our system $2\chi/2\pi = -3.12$ MHz, $\gamma/2\pi \approx 600$ kHz, $\kappa/2\pi = 370$ kHz, and $(g/\Delta)^2 \approx 0.03$.

C.10.2 Master equation simulations

We model our experiment by performing time-domain master equation simulations of all the known dynamics of the system including the full pulse sequence using the QuTip package [55]. At zero temperature, the state of the system $\hat{\rho}(t)$ evolves in time according to the master equation

$$\dot{\hat{\rho}} = i[\hat{\rho}, \hat{H}] + \frac{\gamma_\phi}{2} D[\hat{a}^\dagger \hat{a}] \hat{\rho} + \gamma_1 D[\hat{a}] \hat{\rho} + \kappa D[\hat{b}] \hat{\rho}. \quad (\text{C.6})$$

Here γ_1 and γ_ϕ are the energy relaxation and pure dephasing rates of the qubit, respectively, κ is the relaxation rate of the mechanical oscillator, and $D[\hat{A}]$ is the Lindblad superoperator:

$$D[\hat{A}]\hat{\rho} := \hat{A}\hat{\rho}\hat{A}^\dagger - \frac{1}{2}\hat{A}^\dagger\hat{A}\hat{\rho} - \frac{1}{2}\hat{\rho}\hat{A}^\dagger\hat{A}. \quad (\text{C.7})$$

We initialize the system in the ground state $\hat{\rho}(0) = |g\rangle\langle g| \otimes |0\rangle\langle 0|$ and evolve the state by numerically integrating Eq. C.6 using the *full* Hamiltonian of Eqs. C.2, C.3. We use the full Hamiltonian as opposed to the effective dispersive Hamiltonian (Eq. C.4) for two reasons: first, Eq. C.4 is only correct in the dispersive limit. More importantly, since we can only drive the mechanical system through the transmon, the only way to model the excitation of phonons in our device is by using the full Hamiltonian, as the dispersive Hamiltonian does not allow the two systems to exchange energy.

We first evolve the state $\hat{\rho}(t)$ over the course of the phonon excitation pulse of duration $\tau_{\text{mech}} = 175$ ns, setting $\omega_d = \omega_m$ as the drive frequency — the exact choice of ω_d is not important because the short pulse has a bandwidth on the order of several MHz. Here, the time-dependent Rabi rate of Eq. C.3 is $\Omega(t) = \Omega_0[1 - \cos(2\pi t/\tau_{\text{mech}})]/2$ (see Methods for details about the pulse sequence). We use the calibration factor A_3 described in Methods as an initial estimate for the Rabi rate $\Omega_0(V)$ at a given drive voltage V . We then fine-tune A_3 in order to better match the measurements and simulations, effectively treating it as a free fit parameter.

At the end of the phonon pulse simulation, the mechanical oscillator is left approximately in a coherent state while the qubit is close to its ground state $|g\rangle$. Due to the small residual entanglement between them, the state of the system $\hat{\rho}(\tau_{\text{mech}})$ is in general non-separable. We use $\hat{\rho}(\tau_{\text{mech}})$ as the initial state for a subsequent simulation of the spectroscopy pulse. Here the pulse length is $\tau = 1.5$ μ s, and the Rabi rate $\Omega_0(V)$ is determined using the calibration factor A_1 . For this simulation, the drive frequency $\omega_d = \omega'_{\text{ge}} + \delta$ is swept over a range of detunings $\delta/2\pi \in [-20, 10]$ MHz in the vicinity of the (renormalized) qubit frequency, $\omega'_{\text{ge}} = \omega_{\text{ge}} + g^2/\Delta$. For each detuning δ , we calculate the excited state population $p_e(\tau_{\text{mech}} + \tau) = \text{Tr}\{\hat{\rho}_f|e\rangle\langle e|\}$, where $\hat{\rho}_f := \hat{\rho}(\tau_{\text{mech}} + \tau)$ is the final state at the end of the spectroscopy pulse. Noticeably, the excited state population $p_e(t)$ exhibits rapid oscillation during the qubit readout. This is caused by the strong coupling between the qubit and the mechanics in our system. However, in the actual experiment, the fast oscillations in $p_e(t)$ are filtered out due to the finite bandwidth of the readout resonator. To approximate the experimental readout, we freely evolve the system with \hat{H}_0 and calculate $p_e(t)$ over a time range $[\tau_{\text{mech}} + \tau, \tau_{\text{mech}} + \tau + \delta\tau]$ (with $\delta\tau = 100$ ns) after the end of spectroscopy pulse and record the time-averaged value $\overline{p_e(t)}$ as the actual measurement result. Repeating this simulation over a range of detunings produces the simulated qubit excitation spectra $p_e(\delta)$ in Fig. 4 of the main text. We remark that all parameters used in these simulations except A_3 were directly measured (see Table C.1) — no free parameters were used to model the data, with the exception of an overall scaling factor and an offset.

C.10.3 Excitation of phonons through the transmon

In this experiment, the mechanical system can only be driven through the transmon’s charge line (see Eq. C.3). Despite the fact that the transmon is a highly nonlinear system, it is still possible to excite many phonons at a time and prepare the mechanical oscillator in states that closely approximate coherent states. This is because in the dispersive limit, the polaritons (the eigenvectors of the full Hamiltonian of Eq. C.2) are well-separated into transmon-like and phonon-like modes. More precisely, we can diagonalize the linear part of Eq. C.2 through the polaron transformation [46]

$$\begin{pmatrix} \hat{c}_+ \\ \hat{c}_- \end{pmatrix} = \begin{pmatrix} \cos(\theta/2) & \sin(\theta/2) \\ -\sin(\theta/2) & \cos(\theta/2) \end{pmatrix} \begin{pmatrix} \hat{a} \\ \hat{b} \end{pmatrix}, \quad (\text{C.8})$$

with $\tan(\theta) = 2g/\Delta$. In the dispersive limit, the polaritons can be written approximately as $\hat{c}_+ \approx \hat{a} + (g/\Delta)\hat{b}$ and $\hat{c}_- \approx \hat{b} - (g/\Delta)\hat{a}$, or alternatively the original modes can be written as $\hat{a} \approx \hat{c}_+ - (g/\Delta)\hat{c}_-$ and $\hat{b} \approx \hat{c}_- + (g/\Delta)\hat{c}_+$. The linear part of the diagonalized Hamiltonian (including the drive) is therefore

$$\hat{H}'_{\text{linear}} = \Delta_+ \hat{c}_+^\dagger \hat{c}_+ + \Delta_- \hat{c}_-^\dagger \hat{c}_- + \frac{1}{2} [\Omega(t)(\hat{c}_+ - (g/\Delta)\hat{c}_-) + \text{h.c.}], \quad (\text{C.9})$$

where $\Delta_\pm := \omega_\pm - \omega_d$, and $\omega_\pm = (\omega_{\text{ge}} + \omega_m)/2 \pm \sqrt{\Delta^2/4 + g^2}$ are the polariton frequencies. If we set $\omega_d = \omega_-$, we are left with

$$\hat{H}'_{\text{linear}} = \Delta_+ \hat{c}_+^\dagger \hat{c}_+ + \frac{1}{2} [\Omega(t)(\hat{c}_+ - (g/\Delta)\hat{c}_-) + \text{h.c.}]. \quad (\text{C.10})$$

In this frame, the transmon-like polariton is a high-energy excitation that adiabatically follows the time-dependent drive $\Omega(t)$ if $\tau_{\text{mech}} \gg \Delta_+^{-1}$ — that is, if the pulse length is much larger than the timescale associated with the transmon transition — and the phonon-like polariton is driven directly at a suppressed rate $(g/\Delta)\Omega(t)$. In this experiment $\tau_{\text{mech}} = 175$ ns and $\Delta_+^{-1} \approx 11$ ns, so the transmon rapidly responds to the drive and efficiently transfers its energy to the mechanical system.

C.11 Optimization of the dispersive coupling χ

In addition to designing phononic-crystal-defect resonators with large piezoelectric coupling (see Methods), we took great care to maximize the dispersive coupling $|\chi|$ between the transmon and the mechanical oscillators by choosing an appropriate set of transmon parameters. The transmon qubit used in this work is of the ‘Xmon’ style, with all aspects of its design (including capacitor shape, SQUID loop, charge line, flux line, and resonator coupling capacitor) closely following those outlined in Ref. [11]. Since χ is a function of the coupling rate g , the anharmonicity $\alpha = \omega_{\text{ge}} - \omega_{\text{ef}}$, and the detuning $\Delta = \omega_{\text{ge}} - \omega_m$ (see Eq. C.5), it may seem that in order to maximize $|\chi|$, we must do so by varying all three parameters (g, α, Δ). However, once we constrain the transmon frequency

(to a value in the region where we expect to see mechanical modes, $\sim 2.0 - 2.4$ GHz) and the defect resonator design is fixed, g is no longer a free parameter — rather it is determined entirely by α . To see this, we write g in terms of the Josephson energy E_J and charging energy E_C of the transmon, as well as the Foster circuit values (C_0, C_1, L_1) that encode the properties of the defect resonator (see Ref. [6] for details):

$$\hbar g = 8E_C^{\phi,\theta} n_{\text{zp}}^\theta n_{\text{zp}}^\phi, \quad (\text{C.11})$$

where

$$E_C^{\phi,\theta} = \frac{C_0}{C_1 + C_\Sigma} \frac{e^2}{2[C_0 + (C_1^{-1} + C_\Sigma^{-1})^{-1}]}, \quad (\text{C.12})$$

$$n_{\text{zp}}^\phi = \frac{1}{2} \left(\frac{E_J}{2E_C} \right)^{1/4}, \quad (\text{C.13})$$

$$n_{\text{zp}}^\theta \approx \frac{1}{2} \left(\frac{C_0 + C_1}{L_1} \frac{\Phi_0^2}{e^2} \right)^{1/4}, \quad (\text{C.14})$$

$C_\Sigma = e^2/2E_C$ is the transmon capacitance, and $\Phi_0 = \hbar/2e$ is the reduced flux quantum. After some algebra, we obtain $\hbar g = \xi(8E_J E_C^3)^{1/4}$, where

$$\xi = \frac{C_0}{C_0 + C_1} \left(\frac{C_0 + C_1}{L_1} \frac{\Phi_0^2}{e^2} \right)^{1/4} = \text{const.} \quad (\text{C.15})$$

The value of the dimensionless coupling constant ξ is determined entirely by the defect resonator design and is independent of the transmon parameters. For our system $\xi \approx 0.037$ — see Methods for details on how the Foster circuit values were calculated. The final constraint comes from the transmon energy-level spacing [60]

$$\hbar\omega_{\text{ge}} = \sqrt{8E_J E_C} - E_C. \quad (\text{C.16})$$

From this equation, if ω_{ge} and E_C are both fixed, then E_J is constrained to obey $E_J = (\hbar\omega_{\text{ge}} + E_C)^2/8E_C$. Therefore, we obtain an expression for g in terms of the only remaining free design parameter, $\alpha = E_C/\hbar$:

$$g(\alpha) = \xi \sqrt{\alpha(\omega_{\text{ge}} + \alpha)}. \quad (\text{C.17})$$

The optimization problem can then be written as

$$\arg \max |\chi(\alpha, \Delta)| \quad (\text{C.18})$$

$$\text{s.t. } |\Delta| \geq 5g(\alpha), \quad (\text{C.19})$$

$$|\Delta - \alpha| \geq 5g(\alpha), \quad (\text{C.20})$$

$$\frac{(\omega_{\text{ge}} + \alpha)^2}{8\alpha^2} \geq 50. \quad (\text{C.21})$$

The first two constraints (Eqs. C.19, C.20) are imposed to ensure the system is in the dispersive limit ($g/|\Delta| \ll 1$ and $g/|\Delta - \alpha| \ll 1$, with $\Delta := \omega_{\text{ge}} - \omega_{\text{m}}$), while the third constraint (Eq. C.21) is imposed to ensure the qubit is in the transmon limit ($E_J/E_C \gg 1$). Solving this optimization problem numerically (with $\omega_{\text{ge}}/2\pi = 2.3$ GHz) we obtain the optimal values $\alpha_{\text{opt}}/2\pi \approx 120$ MHz and $\Delta_{\text{opt}} = -5g$ (or alternatively $\Delta_{\text{opt}} - \alpha = 5g$), with $g(\alpha_{\text{opt}})/2\pi \approx 22$ MHz. It is interesting to note that the coupling constant ξ is so large in our system that — under the imposed constraints — the straddling regime $0 < \Delta < \alpha$ is not accessible (where $|\chi|$ would be much larger). This is because within the allowed range of α values, $g(\alpha)$ is so large that the entire straddling region violates the dispersive constraints (Eqs. C.19, C.20). Since $g(\alpha)$ grows sub-linearly, it is possible to choose a sufficiently large value of α such that these constraints are no longer violated, but then we violate the transmon limit constraint (Eq. C.21). See Supplementary Figure S2 for a visual explanation.

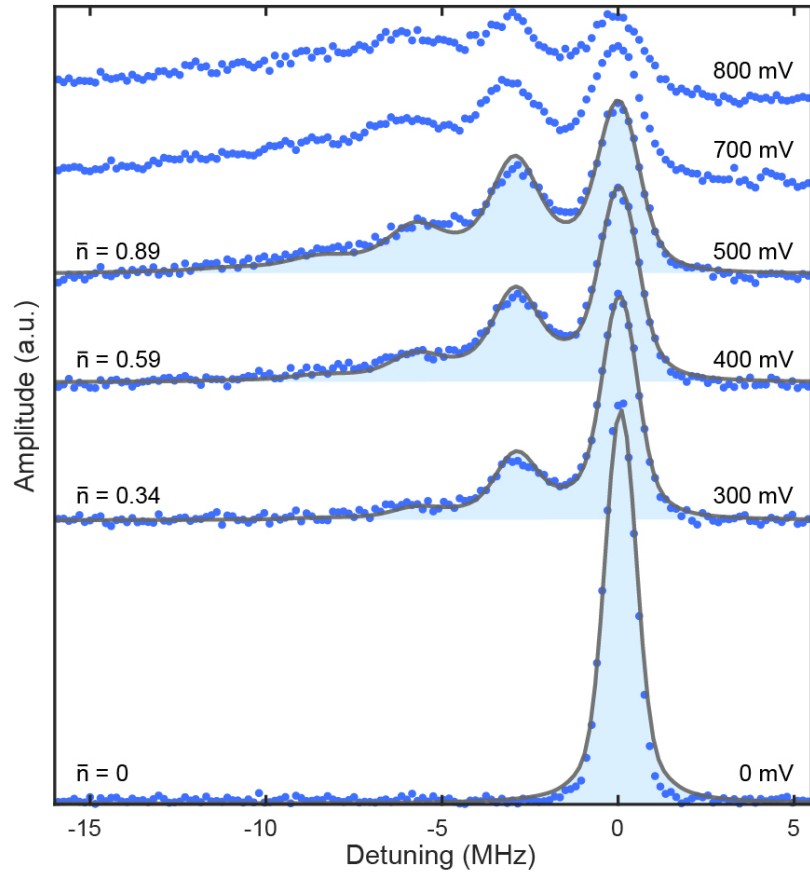


Figure C.6: **Supplementary Figure S1 | phonon-number splitting.** Additional dataset collected using the same mechanical mode as the one presented in the main text, at frequency $\omega_m/2\pi = 2.405 \text{ GHz}$. As before, the horizontal axis represents detuning with respect to the qubit frequency $\omega_{\text{ge}}/2\pi = 2.317 \text{ GHz}$, and the shown fits have only one fit parameter, the correction factor for the mechanical drive amplitude. For this dataset, we found that for the first four drive amplitudes, a correction factor of 1.0 led to curves that fit our observation. The higher voltage data fit better to a correction factor of 0.78 (not shown). The cause of this discrepancy is unknown, and it may have arisen from some change in the experimental setup.

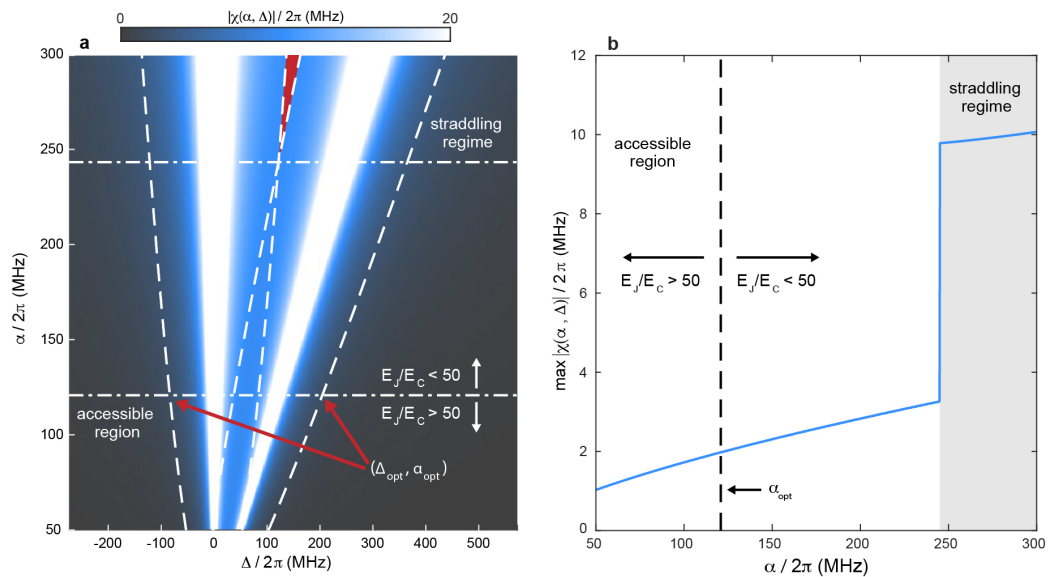


Figure C.7: Supplementary Figure S2 | Dispersive coupling optimization. **a**, Dispersive coupling rate $|\chi(\alpha, \Delta)|$ as a function of the detuning $\Delta = \omega_{\text{ge}} - \omega_{\text{m}}$ and the anharmonicity $\alpha = \omega_{\text{ge}} - \omega_{\text{ef}}$. The plotted values are bounded above at $|\chi|/2\pi = 20$ MHz, which artificially saturates the color near the poles at $\Delta = 0$ and $\Delta = \alpha$. The boundaries that define the forbidden regions $|\Delta| < 5g$ and $|\Delta - \alpha| < 5g$ around each pole are indicated by dashed lines. We also indicate the value of α above which the transmon limit condition $E_J/E_C > 50$ is violated (dash-dotted line), as well as the value of α above which the straddling regime $0 < \Delta < \alpha$ (shaded red) becomes accessible due to the poles becoming sufficiently separated. The optimal points $(\Delta_{\text{opt}}, \alpha_{\text{opt}})$ for our device are indicated. **b**, Maximum value of $|\chi(\alpha, \Delta)|$ over all possible detunings Δ , plotted as a function of α . This value increases sublinearly for small α until a threshold is reached and the straddling regime becomes accessible. Above this threshold the dispersive coupling becomes much larger ($\chi/2\pi \approx 10$ MHz), but this region is not accessible in our device as it violates the constraint $E_J/E_C > 50$.

Appendix D

Device fabrication

I will finish with a detailed description of the real research: the fabrication of the devices. This will be restricted to the first generation of devices (“LNOS01”), which included the one presented in Chapter 4. The more advanced techniques used in later generations (including batch “LNOS04”, where the device from Chapter 5 came from) will be discussed in future theses from the group.

D.1 Process flow

Here is a summary of the full process flow, with pointers to each of the subsections below. Each subsection contains a list of processing steps and images with comments. Processing steps surrounded by color boxes are linked to the picture boxed with the same color.

- **D.4.1 Film thinning**
Blanket argon milling to thin LN film from 500 nm to 200 nm
- **D.4.2 Small-scale LN patterning**
E-beam lithography and argon milling to etch LN phononic crystals
- **D.4.3 Large-scale LN patterning**
Optical lithography and argon milling to etch remaining LN
- **D.4.4 Microwave base layer deposition**
Optical lithography, Al evaporation, and liftoff (ground planes, feedlines, etc.)
- **D.4.5 Josephson junction growth**
E-beam lithography and double-angle Al evaporation with oxidation step in between
- **D.4.6 PCDR electrode deposition**
E-beam lithography, Al evaporation, and liftoff (PCDR electrodes)
- **D.4.7 Bandage deposition**
E-beam lithography, in-situ argon milling, Al evaporation, and liftoff
- **D.4.8 Release mask**

E-beam lithography to pattern release mask (windows expose PCDRs only)

- **D.4.9 Dice and release**

Dice quadrant into chips; XeF₂ undercut of PCDRs, strip release mask

D.2 List of abbreviations

Chemicals

- DI H₂O = distilled water
- ACT = Acetone
- IPA = Isopropyl alcohol
- NMP = N-Methyl-2-pyrrolidone
- MIBK = Methyl isobutyl ketone
- Piranha = 3:1 H₂SO₄:H₂O₂ (sulfuric acid and hydrogen peroxide)
- BOE = buffered oxide etch
- XF₂ = XeF₂ (xenon difluoride)

Resists

- PMMA = Poly(methyl methacrylate)
- MMA = methyl methacrylate
- SPR = Shipley photoresist

Processes

- OL = optical lithography
- EBL = electron beam lithography
- EBE = electron beam evaporation
- ArM = argon milling
- LO = liftoff
- N₂BD = nitrogen blow-dry
- DB = dehydration bake
- PB = pre-bake
- HB = hard bake
- RB = reversal bake
- SC = spin-coat
- DEV = develop
- RT = room temperature

Diagnostics & characterization

- BFM = bright field microscopy
- DFM = dark field microscopy

- SEM = scanning electron microscopy
- PFM = profilometry
- ELM = ellipsometry

D.3 List of tools

- Electron beam lithography: JEOL 6300-FS 100 keV
- Optical lithography: Heidelberg MLA150
- Electron beam evaporation, oxidation, and argon milling: Plassys MEB550S
- Argom milling: Intlvac Nanoquest
- Ellipsometry: Woollam M2000
- Scanning electron microscopy: FEI Nova
- Optical microscopy: Keyence VK-X
- Resistance measurements: Keysight B1500A
- Profilometry: Dektak XT-S
- Wafer dicing: DISCO DAD3240
- XF2 etching: Xacix e-1

D.4 Details

D.4.1 Film thinning

We begin the fabrication process with a 4-inch wafer of X-cut lithium niobate on silicon (LNOS) purchased from a manufacturer. The silicon is $500\text{ }\mu\text{m}$ thick and the LN film is nominally 500 nm, with an rms variation of $\sim 100\text{ nm}$ across the wafer. We dice the wafer into four quadrants each with dimensions 32 mm x 36 mm. From now on each quadrant is processed individually. Usually one quadrant can be used to fabricate a batch of 30 chips.

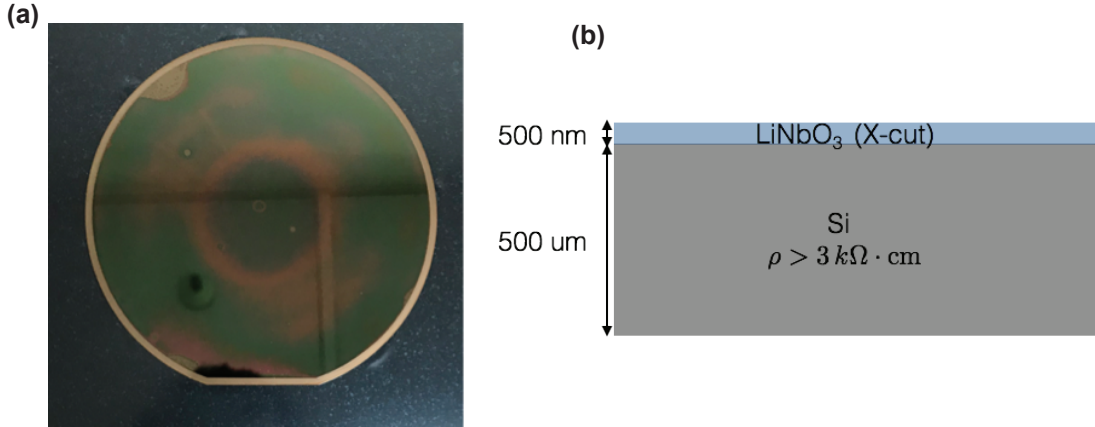


Figure D.1: **LNOS wafer.** (a) Image of 4-inch LNOS wafer as shipped by manufacturer. The nonuniformity of the LN film is as apparent from the fringes. (b) Diagram of wafer cross-section, including 500-nm X-cut LN over 500- μm high-resistivity silicon substrate.

For this and all other argon milling steps, we use an Intlvac Nanoquest tool equipped with a Kaufman ion source. The source voltage is 750 V, and the beam voltage and current are 150 V and 50 mA. The chuck is angled such that the beam hits the sample at 12° with respect to the normal, and the chuck rotates at a rate of ~ 1 Hz. The non-zero beam angle is supposed to reduce re-deposition of material on the sidewalls.

- Sonicate in ACT 20 min
- Sonicate in IPA 5 min, N2BD
- Cleanliness check: BFM & DFM
- LN thickness mapping: ELM
- Mount quadrant to clean Si carrier wafer: PMMA 950K, bake 10 min @ 80C
- Timed ArM to desired thickness (12 nm/min)
- Etch check: BFM & DFM
- Remove from carrier: sonicate in ACT 20 min
- Quadrant now separated: sonicate in ACT 5 min
- Sonicate in IPA 5 min
- LN thickness mapping: ELM

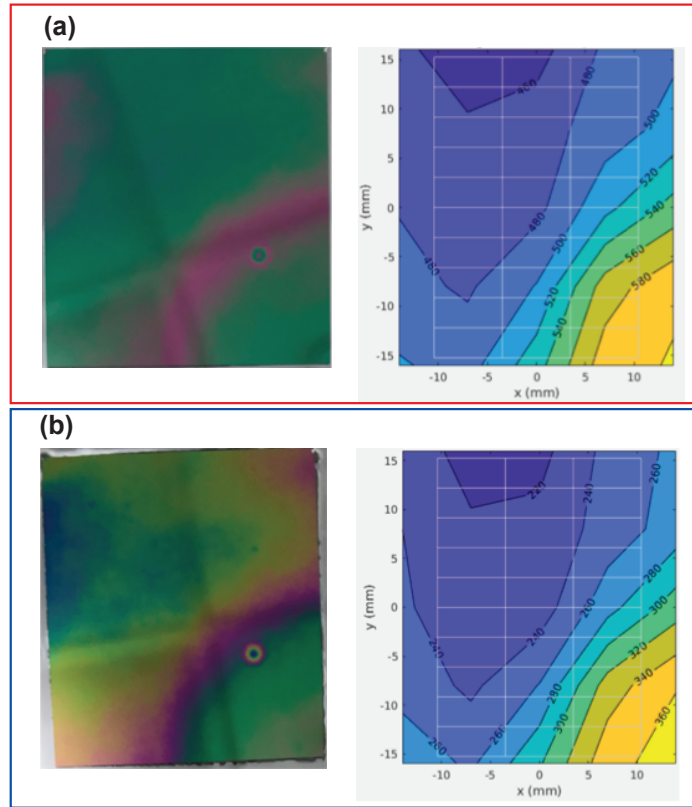


Figure D.2: LN film thinning. (a) (left) Photograph of clean 32 mm x 36 mm quadrant immediately before thinning step; (right) film thickness map as measured by ellipsometry. (b) (left) Photograph of quadrant immediately after thinning step. The change in thickness is obvious from the change in colors; (right) film thickness map.

D.4.2 Small-scale LN patterning

At this stage the average LN thickness over the usable area of the quadrant is now approximately the same as the value targeted in the phononic crystal design. We now proceed to pattern the phononic crystal structures in the LN. This is done by first writing a mask on positive e-beam resist (CSAR 6200.13) and then transferring it to the film with an argon milling step (same recipe as used in the preceding step). The CSAR gets severely damaged by the milling step and is difficult to remove, necessitating a sequence of plasma and wet cleans that are progressively more aggressive. At the scale of the nanostructures, the CSAR also gets significantly distorted in two predominant ways: 1) its thickness is reduced by the etch, and 2) its lateral dimensions are also reduced, similar to shrink

wrap when heated. This results in rather poor pattern transfer and feature fidelity — see Fig. D.3¹.

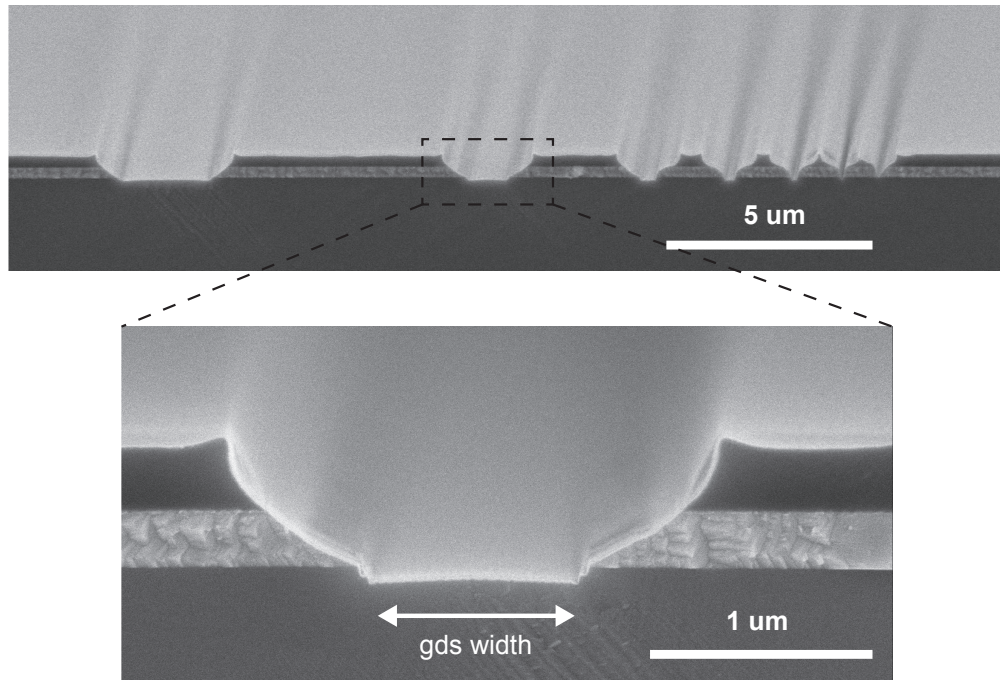


Figure D.3: Test trenches. (top) Trenches of various widths transferred from a CSAR mask to the LN film; (bottom) Close-up of 1- μm trenches, clearly showing the mask distortion, the LN sidewall angle, and the overetching into the Si substrate.

Here are the processing steps:

- DB 2 min @ 180 C
- EBE 5 nm Al @ 0.3 nm/s (buffer layer)
- EBE 5 nm Ti @ 0.2 nm/s (adhesion layer)
- SC CSAR 6200.13 @ 2000 rpm for 60s (positive ebeam resist)
- PB 2 min @ 150 C
- EBL, beam current = 1000 pA, dose = 275 uC/cm²
- DEV Xylenes 90 s @ RT

¹A significant improvement to all of this can be accomplished by using negative resist (HSQ), as done in later generations of devices.

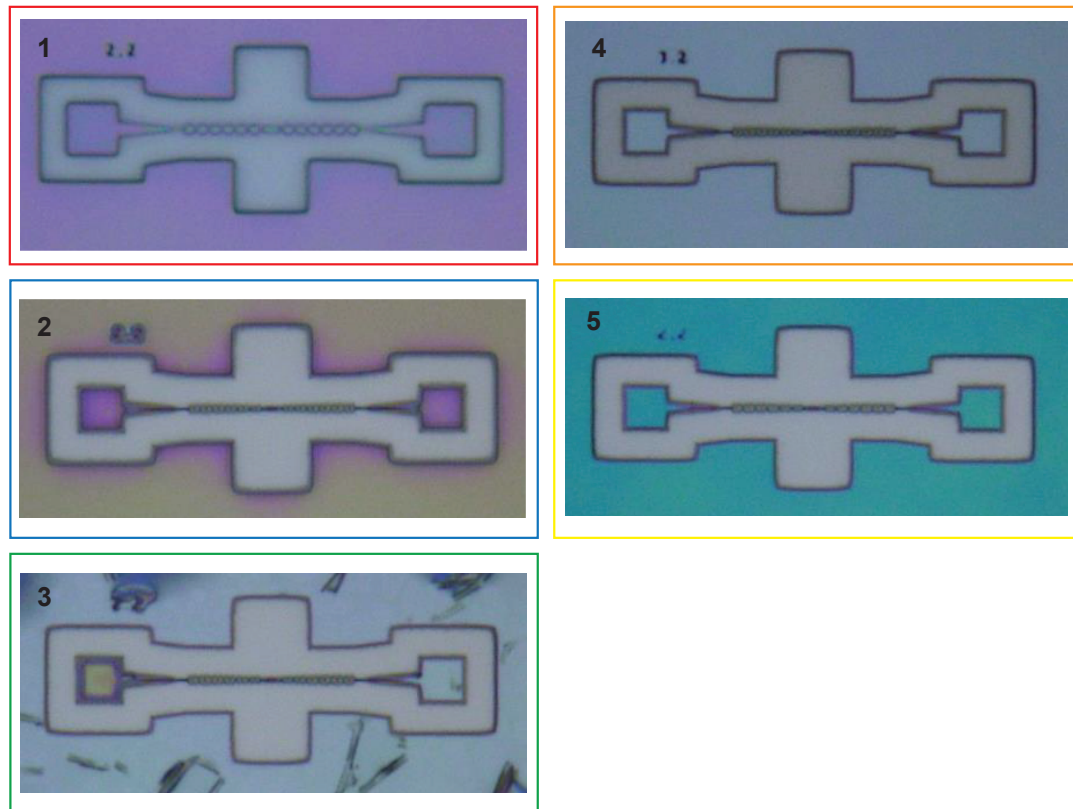


Figure D.4: Processing and cleaning stages. Optical micrographs of a test structure throughout the various processing stages.

- IPA 10 s, N2BD
- Exposure check: BFM
- HB 30 min @ 130 C
- Mount quadrant to clean Si carrier wafer: PMMA 950K, bake 10 min @ 80 C
- Stack measurement: PFM
- Timed ArM to desired thickness (12 nm/min)
- Etch check: BFM
- Stack measurement: PFM
- Remove from carrier: sonicate in ACT 20 min
- Quadrant now separated: sonicate in ACT 5 min
- Sonicate in IPA 5 min
- Check: BFM
- O₂ descum 5 min

- Strip resist: NMP 60 min @ 80 C
- Soak in ACT 5 min
- Soack in IPA 5 min
- Strip check: BFM
- Stack measurement: PFM
- Clean: piranha 10 min @ 70 C, 30+30 s DI H₂O rinse
- Stack measurement: PFM
- Clean check: BFM

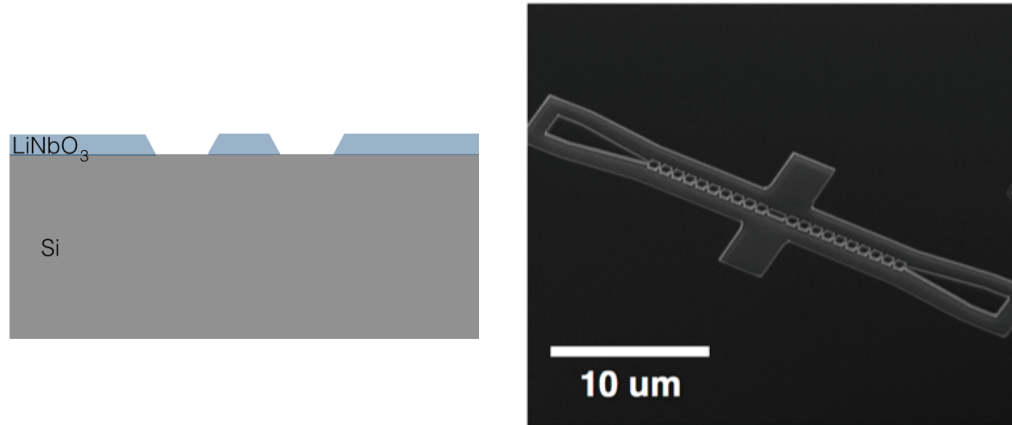


Figure D.5: **Patterned structure.** (left) Diagram of structure cross-section; (right) SEM of finished test structure.

D.4.3 Large-scale LN patterning

The nanostructures are now etched all the way down to the silicon substrate, but because we used positive resist, only a tiny outline around the structures was etched. The vast majority of the quadrant still has LN on top. This LN must be removed, because fabricating high-Q microwave circuits directly on top of it is a very bad idea as it introduces significant damping in the form of acoustic radiation. To remove the remaining LN we use optical lithography to mask the structures, etching away the LN again with the same argon milling step. The photoresist gets damaged, but not as much as the CSAR. Still, we aggressively clean the sample after etching because this is our last chance to use chemicals such as piranha, as later on there will be aluminum on the sample.

- DB 10 min @115 C
- SC SPR-3612 5 s 300 rpm, 40 s 5500 rpm, 5 s 300 pm
- PB 60 s @ 90 C

- OL, dose = 90 mJ/cm², defocus = 0
- DEV MF-26A 40 s @ RT, 10 s DI H₂O rinse, N2BD

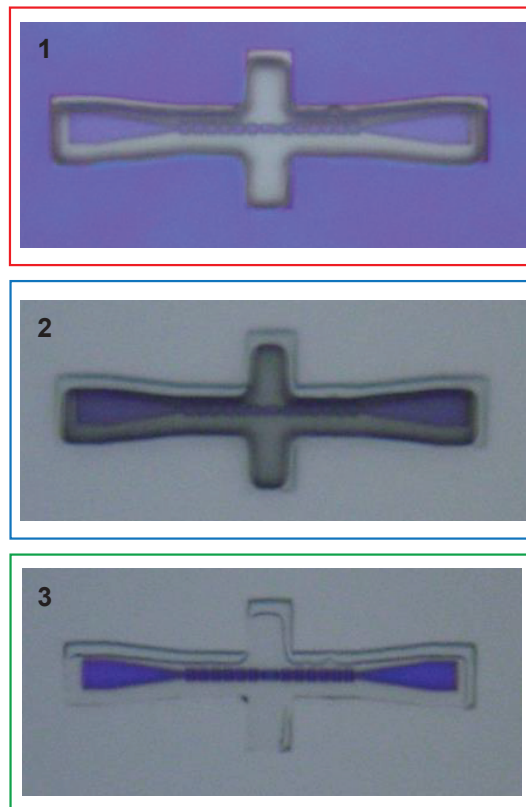


Figure D.6: **Processing and cleaning stages.** Optical micrographs of test structure throughout the various processing stages.

- Exposure check: BFM
- HB 60 s @ 115 C
- Mount quadrant to clean Si carrier wafer: PMMA 950K, bake 10 min @ 80C
- Stack measurement: PFM
- Timed ArM to desired thickness (12 nm/min)
- Etch check: BFM
- Stack measurement: PFM
- Remove from carrier: sonicate in ACT 20 min
- Quadrant now separated: sonicate in ACT 5 min
- Sonicate in IPA 5 min

- Strip resist: NMP 60 min @ 80C
- Soak in ACT 5 min
- Soack in IPA 5 min
- Strip check: BFM
- Stack measurement: PFM
- Clean #1: piranha 10 min @ 70C, 30+30 s DI H₂O rinse
- Stack measurement: PFM
- Clean check: BFM
- Clean #2: 6:1 BOE 30 s @ RT, 30+30 s DI H₂O rinse
- Stack measurement: PFM
- Check structures: SEM

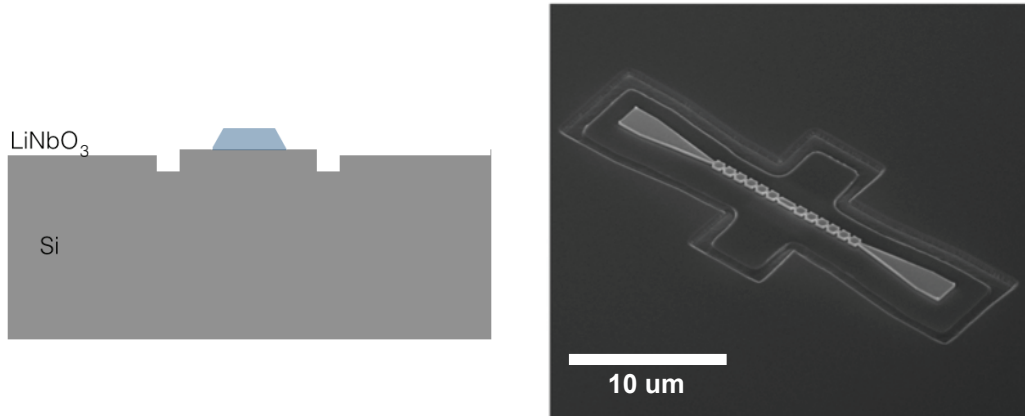


Figure D.7: **Patterned structure.** (left) Diagram of structure cross-section; (right) SEM of finished test structure.

D.4.4 Microwave base layer deposition

This is regular liftoff using image-reversal resist AZ-5214. Things to pay attention to are the reversal bake temperature and the cleanliness of the sample after liftoff.

- DB 5 min @11 5C
- SC AZ-5214 5 s 300 rpm, 40 s 4000 rpm, 5 s 300 rpm
- PB 2 min @90 C
- OL dose = 15 mJ/cm², defocus = 0
- RB 120 s @ 120 C
- Flood exposure 20 s
- DEV MF-26A 2 min @ RT, 20 s DI H₂O rinse, N2BD

- HB 2 min @ 90 C
- Exposure check: BFM
- EBE 2 min Ti @ 0.2 nm/s (Ti getter)
- EBE 100 nm Al @ 0.3 nm/s
- Flow 10 Torr 9:1 Ar:O₂, 1 Torr/min ramp, hold 10 min (passivation)
- LO: NMP 60 min @ 80 C
- Clean: NMP 20 min @ 80 C
- Soak in ACT 5 min
- Soak in IPA 5 min
- LO check: BFM

D.4.5 Josephson junction growth

Next we grow junctions using the Dolan bridge technique. First we perform EBL on a MMA/PMMA bilayer. The PMMA bridges are formed by exposing the stack with two doses: : a “base” dose to clear the entire stack, and a “ghost” dose to clear only the underlying MMA. With a bridge, we can now grow a junction by first doing an aluminum evaporation at an angle of -45°, followed by an oxidation using a 9:1 Ar:O₂ mixture, and finally a second evaporation at +45°. See Fig. D.8 for illustrations.

- DB 2 min @ 180 C
- SC MMA (8.5) MAA EL 13, 90 s 3000 rpm
- PB 5 min @ 180 C
- SC PMMA 950K A3, 90 s 2000 rpm
- PB 5 min @ 180 C
- EBL, beam current = 1000 pA, dose = 2200 uC/cm² (base), 500 uC/cm² (ghost)
- DEV 3:1 IPA:MIBK 32 s @ RT, 10 s IPA rinse, N2BD
- Exposure check: BFM
- EBE 2 min Ti @ 0.2 nm/s (Ti getter)
- EBE 42 nm Al @ 0.3 nm/s, +45 deg (Al #1)
- Flow 10 Torr 9:1 Ar:O₂, 1 Torr/min ramp, hold 10 min (oxidation)
- EBE 71 nm Al @ 0.3 nm/s, -45 deg (Al #2)
- Flow 10 Torr 9:1 Ar:O₂, 1 Torr/min ramp, hold 10 min (passivation)
- LO: NMP 60 min @ 80 C
- Clean: NMP 20 min @ 80 C
- Soak in ACT 5 min
- Soack in IPA 5 min
- LO check: BFM
- Resistance check

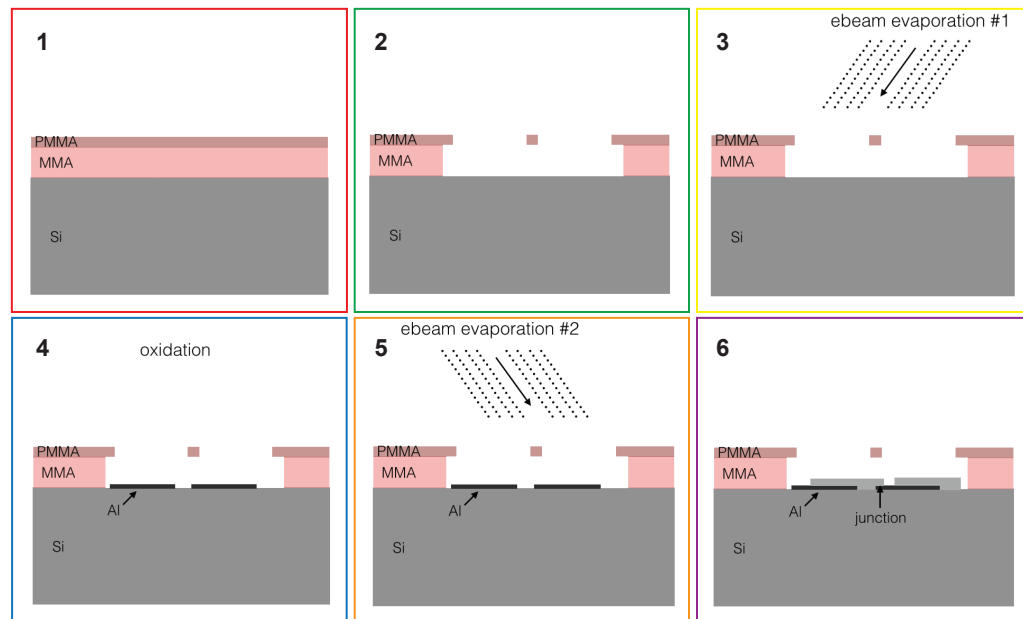


Figure D.8: **Junction fabrication.** Illustration of various processing stages.

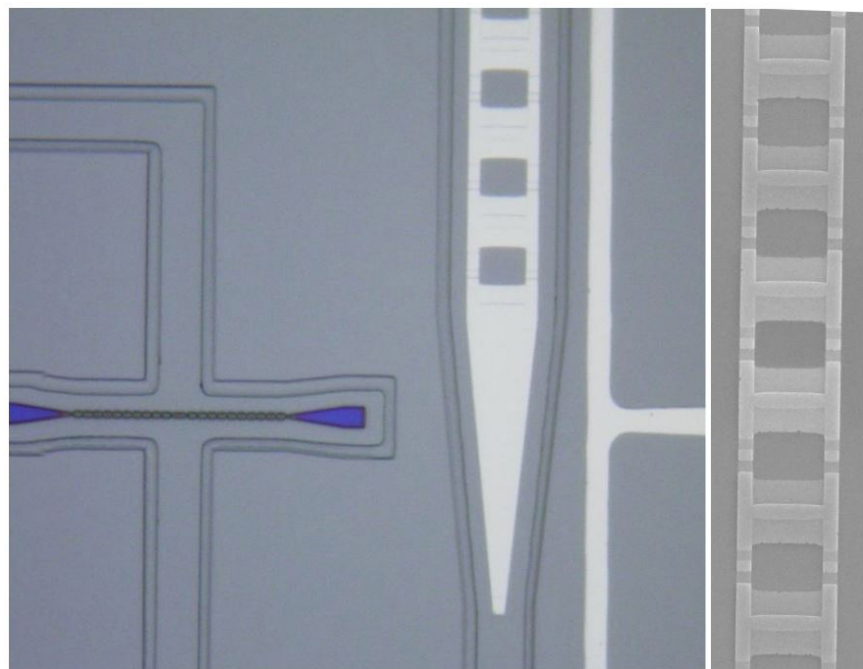


Figure D.9: **SQUID array.** (left) Optical micrograph and (right) SEM of SQUID array after liftoff.

D.4.6 PCDR electrode deposition

We fabricate the PCDR electrodes using a separate mask, as the double-angle evaporation technique used for junctions is not well suited for placing liftoff features with very high precision (10's of nm positioning error). High overlay precision is critical for this step, as the electrodes approach very near the phononic-crystal structures (~ 200 nm).

- Remove dust: N2BD
- Cleanliness check: BFM & DFM
- DB 2 min @ 180 C
- SC MMA (8.5) MAA EL 13, 90 s 3000 rpm
- PB 5 min @ 180 C
- SC PMMA 950K A3, 90 s 2000 rpm
- PB 5 min @ 180 C
- EBL, beam current = 1000 pA, dose = 2200 uC/cm²
- DEV 3:1 IPA:MIBK 40 s @ RT, 10 s IPA rinse, N2BD
- Exposure check: BFM
- EBE 2 min Ti @ 0.2 nm/s (Ti getter)
- EBE 200 nm Al @ 0.3 nm/s
- Flow 10 Torr 9:1 Ar:O₂, 1 Torr/min ramp, hold 10 min (passivation)
- LO: NMP 60 min @ 80 C
- Clean: NMP 20 min @ 80 C
- Soak in ACT 5 min
- Soack in IPA 5 min
- LO check: BFM

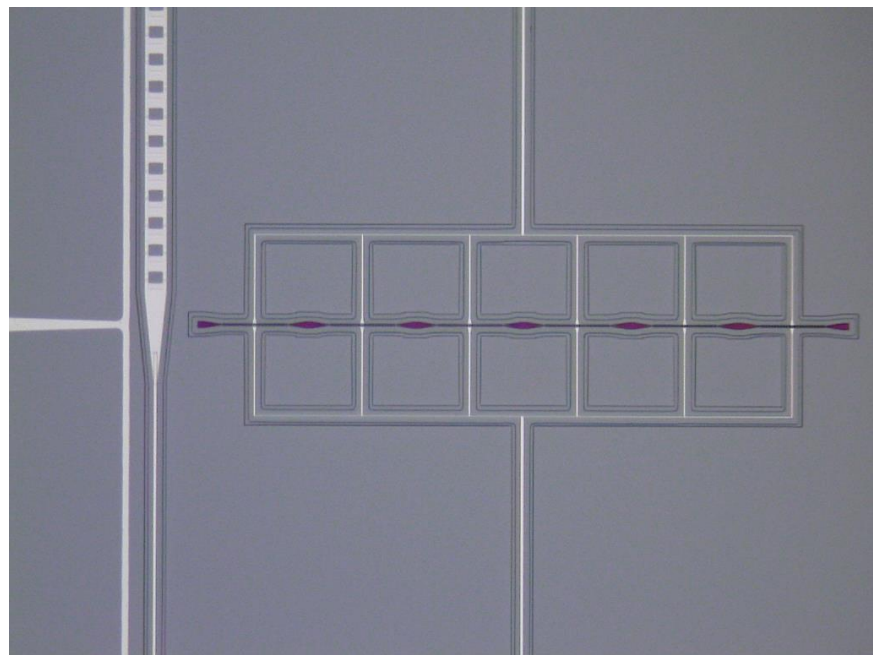


Figure D.10: **PCDR electrodes.** Optical micrograph of PCDR electrodes after liftoff.

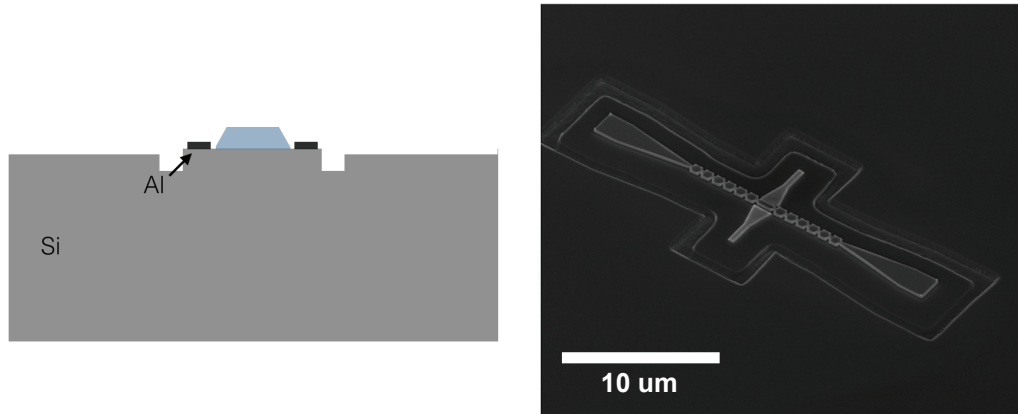


Figure D.11: **Test structure electrodes.** (left) Cross-section schematic; (right) test structure with finished electrodes.

D.4.7 Bandage deposition

In order to join all existing metal layers with lossless (oxide-free) superconducting connections, we perform a bandaging step similar to Ref. [39]. These bandages form connections between the PCDR electrodes and the SQUID array, and between bond pads and test SQUIDs for resistance measurements.

- DB 2 min @ 180 C
- SC MMA (8.5) MAA EL 13, 90 s 3000 rpm
- PB 5 min @ 180 C
- SC PMMA 950K A3, 90 s 2000 rpm
- PB 5 min @ 180 C
- EBL, beam current = 1000 pA, dose = 2200 uC/cm²
- DEV 3:1 IPA:MIBK 40 s @ RT, 10 s IPA rinse, N2BD
- Exposure check: BFM
- ArM 70 s -20 deg, 70 s 0 deg, 70 s +20 deg
- EBE 2 min Ti @ 0.2 nm/s (Ti getter)
- EBE 250 nm Al @ 0.3 nm/s
- Flow 10 Torr 9:1 Ar:O₂, 1 Torr/min ramp, hold 10 min (passivation)
- LO: NMP 60 min @ 80 C
- Clean: NMP 20 min @ 80 C
- Soak in ACT 5 min
- Soack in IPA 5 min
- LO check: BFM
- Resistance check

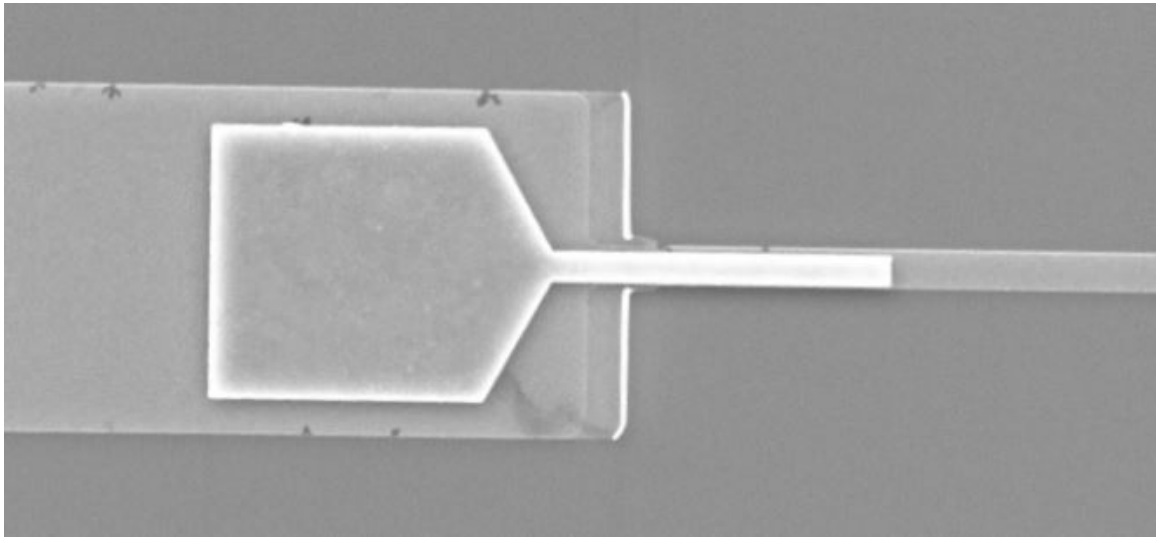


Figure D.12: **Bandage.** SEM of finished bandage connecting a set of contact pads to a test SQUID array.

D.4.8 Release mask

Before we can release the structures it is necessary to put down a mask, because the XeF_2 etch attacks silicon and we do not want to undercut the microwave circuits. The good news is that virtually any resist can mask XeF_2 effectively. The bad news is that we still have to dice the quadrant into chips, and we cannot dice after release because that endangers the fragile suspended structures. We have two options. One is to dice the quadrant and then make a release mask by performing lithography on individual chips before undercutting. The other option is to make a release mask on the whole quadrant, spin a protective layer, dice into chips, remove the protective layer, and then undercut chips one by one before a final wet clean. The former option is of course not practical so we opted for the latter. We use LOR-5B as the release mask because it is immune to acetone, so we can spin regular SPR as a protective layer and clean it off with acetone without affecting the underlying mask.

- DB 2 min @ 180 C
- SC LOR-5B 60 s 3000 rpm
- PB 5 min @ 180 C
- SC PMMA 950 A3 60 s 4000 rpm
- PB 5 min @ 180 C
- EBL, beam current = 1000 pA, dose = 2200 uC/cm²
- DEV 3:1 IPA:MIBK 40 s @ RT, 10 s IPA rinse, N2BD
- Exposure check: BFM

- LOR etch: MF-319 4 s, 10+10 s DI H₂O rinse, 10 s IPA dip, N2BD
- Etch check: BFM
- PMMA strip: soak in ACT 2 min, 5 s spray
- Rinse: IPA spray 5 say, IPA dunk 5 s, N2BD
- Strip check: BFM

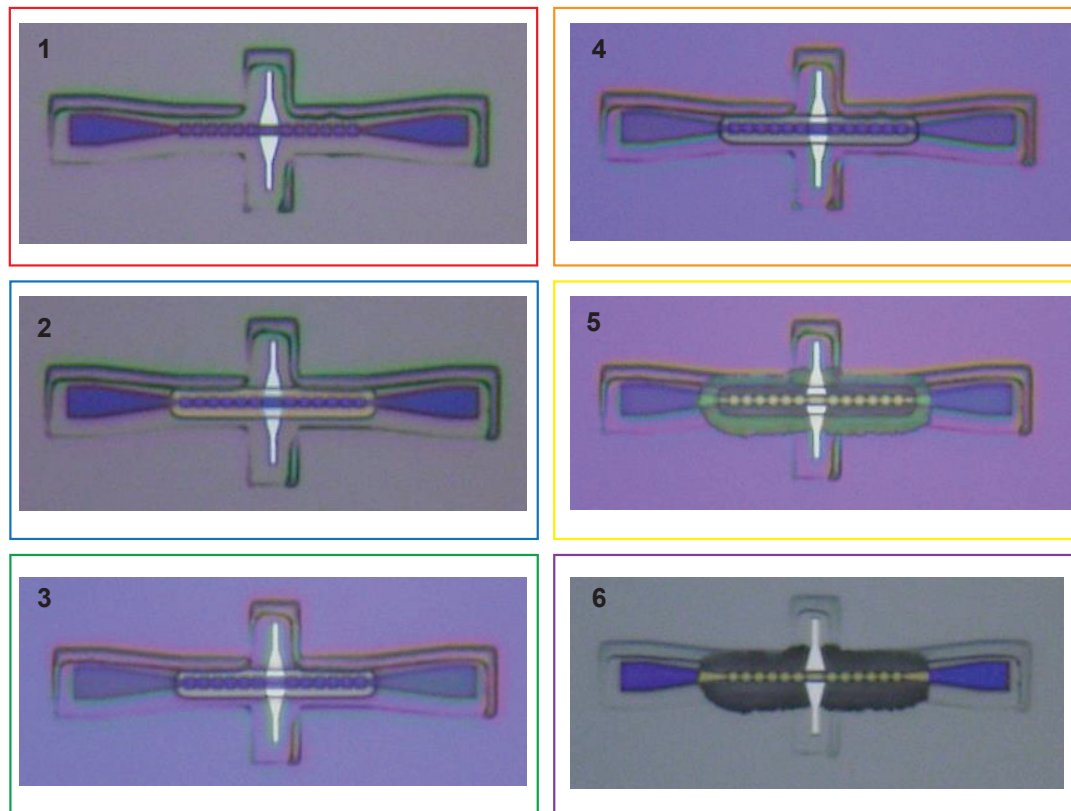


Figure D.13: **Processing stages.** Optical micrographs of test structure at various processing stages.

D.4.9 Dice and release

- DB 10 min @ 110 C
- SC SPR-220-3 40 s 2000 rpm (protective layer)
- PB 2 min @ 110 C
- Dice, feed speed = 2.0 mm/s, 30000 rpm
- Strip protective layer: 5 s ACT spray, 2 min ACT soak
- Rinse: 5 s IPA spray, 2 min IPA soak, N2BD
- Mask check: BFM

- XF2 etch: 3 cycles, 20 s/cycle, 800 mTorr XF2 40 Torr N2
- Etch check: BFM
- Repeat until done
- Strip release mask: 60 min NMP @ 80 C
- Rinse: 5 s ACT spray, 10 min ACT soak
- Rinse: 5 s IPA spray, 5 min IPA soak, N2BD
- Check structures: BFM
- Check structures: SEM
- Resistance check

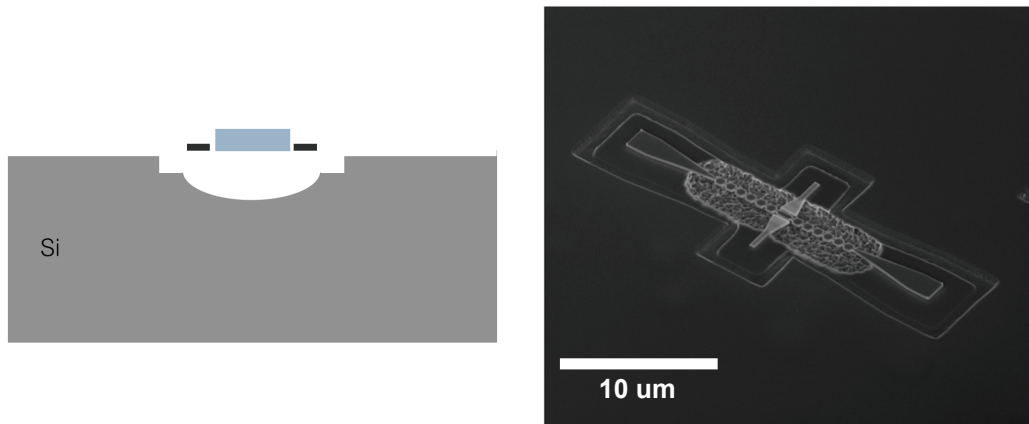


Figure D.14: **Test structure.** (left) Cross-section diagram of suspended structure; (right) SEM of test structure at the end of processing.

Appendix E

List of publications

1. P. Arrangoiz-Arriola¹, E. A. Wollack², Z. Wang, M. Pechal, W. Jiang, T. P. McKenna, J. D. Witmer, R. Van Laer, A. H. Safavi-Naeini, “Resolving the energy levels of a nanomechanical oscillator” *Nature* **571**, 537-540 (2019)
2. W. Jiang, R. N. Patel, F. M. Mayor, T. P. McKenna, P. Arrangoiz-Arriola, C. J. Sarabalis, J. D. Witmer, R. Van Laer, A. H. Safavi-Naeini, “Lithium niobate piezo-optomechanical crystals” *Optica* **6** (7), 845-853 (2019)
3. Z. Wang, M. Pechal, E. A. Wollack, P. Arrangoiz-Arriola, M. Gao, N. R. Lee, A. H. Safavi-Naeini, “Quantum dynamics of a few-photon parametric oscillator” *Phys. Rev. X* **9**, 021049 (2019)
4. M. Pechal, P. Arrangoiz-Arriola, A.H. Safavi-Naeini, “Superconducting circuit quantum computing with nanomechanical resonators as storage” *Quantum Sci. Technol.* **4** (1) (2018)
5. P. Arrangoiz-Arriola, E.A. Wollack, M. Pechal, J.D. Witmer, J.T. Hill, A.H. Safavi-Naeini, “Coupling a superconducting quantum circuit to a phononic crystal defect cavity” *Phys. Rev. X* **8**, 031007 (2018)
6. J.D. Witmer, J.A. Valery, P. Arrangoiz-Arriola, C.J. Sarabalis, J.T. Hill, A.H. Safavi-Naeini, “High-Q photonic resonators and electro-optic coupling using silicon-on-lithium niobate” *Sci. Rep.* **7**: 46313 (2017)
7. P. Arrangoiz-Arriola, A.H. Safavi-Naeini, “Engineering interactions between superconducting qubits and phononic nanostructures” *Phys. Rev. A* **94**, 063864 (2016)

¹These authors contributed equally.

²These authors contributed equally.

Bibliography

- [1] COMSOL Multiphysics 4.4, 2013.
- [2] Thiago P Mayer Alegre, Amir Safavi-Naeini, Martin Winger, and Oskar Painter. Quasi-two-dimensional optomechanical crystals with a complete phononic bandgap. *Opt. Express*, 19(6):5658–5669, 2010.
- [3] Reed W Andrews, Robert W Peterson, Tom P Purdy, Katarina Cicak, Raymond W Simmonds, Cindy A Regal, and Konrad W Lehnert. Bidirectional and efficient conversion between microwave and optical light. *Nat. Phys.*, 10(4):321–326, 2014.
- [4] Thomas Aref, Per Delsing, Maria K Ekström, Anton Frisk Kockum, Martin V Gustafsson, Göran Johansson, Peter J Leek, Einar Magnusson, and Riccardo Manenti. *Quantum Acoustics with Surface Acoustic Waves*, pages 217–244. Springer International Publishing, Cham, 2016.
- [5] A. D. Armour, M. P. Blencowe, and K. C. Schwab. Entanglement and Decoherence of a Micromechanical Resonator via Coupling to a Cooper-Pair Box. *Phys. Rev. Lett.*, 88(14):148301, mar 2002.
- [6] Patricio Arrangoiz-Arriola and Amir H. Safavi-Naeini. Engineering interactions between superconducting qubits and phononic nanostructures. *Phys. Rev. A*, 94(6):063864, dec 2016.
- [7] Patricio Arrangoiz-Arriola, E. Alex Wollack, Marek Pechal, Jeremy D. Witmer, Jeff T. Hill, and Amir H. Safavi-Naeini. Coupling a Superconducting Quantum Circuit to a Phononic Crystal Defect Cavity. *Phys. Rev. X*, 8(3):031007, jul 2018.
- [8] Patricio Arrangoiz-Arriola, E. Alex Wollack, Zhaoyou Wang, Marek Pechal, Wentao Jiang, Timothy P. McKenna, Jeremy D. Witmer, and Amir H. Safavi-Naeini. Resolving the energy levels of a nanomechanical oscillator. *Nature*, in press:arXiv:1902.04681, 2019.
- [9] Markus Aspelmeyer, Tobias J. Kippenberg, and Florian Marquardt. Cavity optomechanics. *Rev. Mod. Phys.*, 86(4):1391–1452, dec 2014.

- [10] Krishna C. Balram, Marcelo I. Davanço, Jin Dong Song, and Kartik Srinivasan. Coherent coupling between radiofrequency, optical and acoustic waves in piezo-optomechanical circuits. *Nat. Photonics*, 10(5):346–352, may 2016.
- [11] R. Barends, J. Kelly, A. Megrant, D. Sank, E. Jeffrey, Y. Chen, Y. Yin, B. Chiaro, J. Mutus, C. Neill, P. O’Malley, P. Roushan, J. Wenner, T. C. White, A. N. Cleland, and John M. Martinis. Coherent josephson qubit suitable for scalable quantum integrated circuits. *Phys. Rev. Lett.*, 111(8), 2013.
- [12] P. Bertet, A. Auffeves, P. Maioli, S. Osnaghi, T. Meunier, M. Brune, J. M. Raimond, and S. Haroche. Direct Measurement of the Wigner Function of a One-Photon Fock State in a Cavity. *Phys. Rev. Lett.*, 89(20):200402, oct 2002.
- [13] A. Bienfait, K. J. Satzinger, Y. P. Zhong, H.-S. Chang, M.-H. Chou, C. R. Conner, É. Dumur, J. Grebel, G. A. Peairs, R. G. Povey, and A. N. Cleland. Phonon-mediated quantum state transfer and remote qubit entanglement. *Science (80-.).*, 364(6438):368–371, apr 2019.
- [14] Joerg Bochmann, Amit Vainsencher, David D. Awschalom, and Andrew N. Cleland. Nanomechanical coupling between microwave and optical photons. *Nat. Phys.*, 9(11):712–716, sep 2013.
- [15] V. B. Braginsky and F. Ya. Khalili. Quantum nondemolition measurements: the route from toys to tools. *Rev. Mod. Phys.*, 68(1):1–11, jan 1996.
- [16] V. B. Braginsky, A. B. Manukin, and G. M. Keiser. Measurement of Weak Forces in Physics Experiments. *Am. J. Phys.*, 46(2):195–196, feb 1978.
- [17] M. Brune, S. Haroche, V. Lefevre, J. M. Raimond, and N. Zagury. Quantum nondemolition measurement of small photon numbers by Rydberg-atom phase-sensitive detection. *Phys. Rev. Lett.*, 65(8):976–979, aug 1990.
- [18] M. Brune, P. Nussenzveig, F. Schmidt-Kaler, F. Bernardot, A. Maali, J. M. Raimond, and S. Haroche. From Lamb shift to light shifts: Vacuum and subphoton cavity fields measured by atomic phase sensitive detection. *Phys. Rev. Lett.*, 72(21):3339–3342, may 1994.
- [19] C.K. Campbell. Applications of surface acoustic and shallow bulk acoustic wave devices. *Proc. IEEE*, 77(10):1453–1484, 1989.
- [20] Manuel Angel Castellanos Beltran. *Development of a Josephson Parametric Amplifier for the Preparation and Detection of Nonclassical States of Microwave Fields*. PhD thesis, University of Colorado, 2010.
- [21] Carlton M. Caves. Quantum-Mechanical Radiation-Pressure Fluctuations in an Interferometer. *Phys. Rev. Lett.*, 45(2):75–79, jul 1980.

- [22] Carlton M. Caves. Quantum-mechanical noise in an interferometer. *Phys. Rev. D*, 23(8):1693–1708, apr 1981.
- [23] Carlton M. Caves, Kip S. Thorne, Ronald W. P. Drever, Vernon D. Sandberg, and Mark Zimmermann. On the measurement of a weak classical force coupled to a quantum-mechanical oscillator. I. Issues of principle. *Rev. Mod. Phys.*, 52(2):341–392, apr 1980.
- [24] Jasper Chan. *Laser cooling of an optomechanical crystal resonator to its quantum ground state of motion*. PhD thesis, California Institute of Technology, 2012.
- [25] Jasper Chan, T. P. Mayer Alegre, Amir H. Safavi-Naeini, Jeff T. Hill, Alex Krause, Simon Gröblacher, Markus Aspelmeyer, and Oskar Painter. Laser cooling of a nanomechanical oscillator into its quantum ground state. *Nature*, 478(7367):89–92, oct 2011.
- [26] Yiwen Chu, Prashanta Kharel, William H Renninger, Luke D Burkhardt, Luigi Frunzio, Peter T Rakich, and Robert J Schoelkopf. Quantum acoustics with superconducting qubits. *Science* (80-.), 358(6360):199–202, oct 2017.
- [27] Yiwen Chu, Prashanta Kharel, Taekwan Yoon, Luigi Frunzio, Peter T. Rakich, and Robert J. Schoelkopf. Creation and control of multi-phonon Fock states in a bulk acoustic-wave resonator. *Nature*, 563(7733):666–670, nov 2018.
- [28] A. N. Cleland. *Foundations of Nanomechanics*. Springer-Verlag, 2001.
- [29] A. N. Cleland and M. R. Geller. Superconducting qubit storage and entanglement with nanomechanical resonators. *Phys. Rev. Lett.*, 93(7):1–4, 2004.
- [30] Andrew Cleland. Les Houches School of Physics Piezoelectricity. (August), 2015.
- [31] A A Clerk, F Marquardt, and K Jacobs. Back-action evasion and squeezing of a mechanical resonator using a cavity detector. *New J. Phys.*, 10(9):095010, sep 2008.
- [32] P. F. Cohadon, A. Heidmann, and M. Pinard. Cooling of a Mirror by Radiation Pressure. *Phys. Rev. Lett.*, 83(16):3174–3177, oct 1999.
- [33] Justin D. Cohen, Seán M. Meenehan, Gregory S. MacCabe, Simon Gröblacher, Amir H. Safavi-Naeini, Francesco Marsili, Matthew D. Shaw, and Oskar Painter. Phonon counting and intensity interferometry of a nanomechanical resonator. *Nature*, 520(7548):522–525, apr 2015.
- [34] Jonathan Cripe, Nancy Aggarwal, Robert Lanza, Adam Libson, Robinjeet Singh, Paula Heu, David Follman, Garrett D. Cole, Nergis Mavalvala, and Thomas Corbitt. Measurement of quantum back action in the audio band at room temperature. *Nature*, 568(7752):364–367, apr 2019.

- [35] M. H. Devoret and R. J. Schoelkopf. Superconducting Circuits for Quantum Information: An Outlook. *Science (80-.)*, 339(6124):1169–1174, mar 2013.
- [36] Michel H. Devoret. Quantum Fluctuations in Electrical Circuits. In S Reynaud, E Giacobino, and J Zinn-Justin, editors, *Quantum Fluctuations (Les Houches Sess. LXIII)*, pages 351–386. Elsevier, New York, 1997.
- [37] Michel H Devoret and Others. Quantum fluctuations in electrical circuits. *Les Houches, Sess. LXIII*, 7(8), 1995.
- [38] G. J. Dolan. Offset masks for liftoff photoprocessing. *Appl. Phys. Lett.*, 31(5):337–339, sep 1977.
- [39] A. Dunsworth, A. Megrant, C. Quintana, Zijun Chen, R. Barends, B. Burkett, B. Foxen, Yu Chen, B. Chiaro, A. Fowler, R. Graff, E. Jeffrey, J. Kelly, E. Lucero, J. Y. Mutus, M. Neeley, C. Neill, P. Roushan, D. Sank, A. Vainsencher, J. Wenner, T. C. White, and John M. Martinis. Characterization and reduction of capacitive loss induced by sub-micron Josephson junction fabrication in superconducting qubits. *Appl. Phys. Lett.*, 111(2):022601, jul 2017.
- [40] Matt Eichenfield, Jasper Chan, Ryan M. Camacho, Kerry J. Vahala, and Oskar Painter. Optomechanical crystals. *Nature*, 462(7269):78–82, nov 2009.
- [41] C. Eichler, Y. Salathe, J. Mlynek, S. Schmidt, and A. Wallraff. Quantum-Limited Amplification and Entanglement in Coupled Nonlinear Resonators. *Phys. Rev. Lett.*, 113(11):110502, sep 2014.
- [42] Albert Einstein. Planck’s theory of radiation and the theory of the specific heat. *Ann. Phys.*, 22:180–190, 1907.
- [43] Ronald M Foster. A Reactance Theorem. *Bell Syst. Tech. J.*, 3(2):259–267, 1924.
- [44] Jay Gambetta, Alexandre Blais, D. I. Schuster, A. Wallraff, L. Frunzio, J. Majer, M. H. Devoret, S. M. Girvin, and R. J. Schoelkopf. Qubit-photon interactions in a cavity: Measurement-induced dephasing and number splitting. *Phys. Rev. A*, 74(4):042318, oct 2006.
- [45] C. W. Gardiner and M. J. Collett. Input and output in damped quantum systems: Quantum stochastic differential equations and the master equation. *Phys. Rev. A*, 31(6):3761–3774, jun 1985.
- [46] S. M. Girvin. Circuit QED: superconducting qubits coupled to microwave photons. In Michel Devoret, Benjamin Huard, Robert Schoelkopf, and Leticia Cugliandolo, editors, *Quantum Mach. Meas. Control Eng. Quantum Syst.* Oxford University Press, 2014.

- [47] Maxim Goryachev, Daniel L. Creedon, Serge Galliou, and Michael E. Tobar. Observation of Rayleigh Phonon Scattering through Excitation of Extremely High Overtones in Low-Loss Cryogenic Acoustic Cavities for Hybrid Quantum Systems. *Phys. Rev. Lett.*, 111(8):085502, aug 2013.
- [48] Martin V. Gustafsson, Thomas Aref, Anton Frisk Kockum, M. K. Ekstrom, Göran Johansson, and Per Delsing. Propagating phonons coupled to an artificial atom. *Science (80-.).*, 346(6206):207–211, oct 2014.
- [49] Bjørn Gustavsen and Adam Semlyen. Rational approximation of frequency domain responses by vector fitting. *IEEE Trans. Power Deliv.*, 14(3):1052–1059, 1999.
- [50] Connor T. Hann, Chang-Ling Zou, Yaxing Zhang, Yiwen Chu, Robert J. Schoelkopf, Steven M. Girvin, and Liang Jiang. Hardware-efficient quantum random access memory with hybrid quantum acoustic systems. pages 1–15, jun 2019.
- [51] Hashimoto. *RF Bulk Acoustic Wave Filters for Communications*. Artech House, 1 edition, 2015.
- [52] L. B. Ioffe, V. B. Geshkenbein, Ch Helm, and G. Blatter. Decoherence in superconducting quantum bits by phonon radiation. *Phys. Rev. Lett.*, 93(5):1–4, 2004.
- [53] E. K. Irish and K. Schwab. Quantum measurement of a coupled nanomechanical resonatorCooper-pair box system. *Phys. Rev. B*, 68(15):155311, oct 2003.
- [54] M. T Jaekel and S Reynaud. Quantum Limits in Interferometric Measurements. *Europhys. Lett.*, 13(4):301–306, oct 1990.
- [55] J. R. Johansson, P. D. Nation, and Franco Nori. QuTiP: An open-source Python framework for the dynamics of open quantum systems. oct 2011.
- [56] B. R. Johnson, M. D. Reed, A. A. Houck, D. I. Schuster, Lev S. Bishop, E. Ginossar, J. M. Gambetta, L. DiCarlo, L. Frunzio, S. M. Girvin, and R. J. Schoelkopf. Quantum non-demolition detection of single microwave photons in a circuit. *Nat. Phys.*, 6(9):663–667, sep 2010.
- [57] Julian Kelly. *Fault-tolerant superconducting qubits*. Thesis, University of California, Santa Barbara, 2015.
- [58] Mikael Kervinen, Ilkka Rissanen, and Mika Sillanpää. Interfacing planar superconducting qubits with high overtone bulk acoustic phonons. *Phys. Rev. B*, 97(20):205443, may 2018.
- [59] H. J. Kimble, Yuri Levin, Andrey B. Matsko, Kip S. Thorne, and Sergey P. Vyatchanin. Conversion of conventional gravitational-wave interferometers into quantum nondemolition

- interferometers by modifying their input and/or output optics. *Phys. Rev. D*, 65(2):022002, dec 2001.
- [60] Jens Koch, Terri M. Yu, Jay Gambetta, A. A. Houck, D. I. Schuster, J. Majer, Alexandre Blais, M. H. Devoret, S. M. Girvin, and R. J. Schoelkopf. Charge-insensitive qubit design derived from the Cooper pair box. *Phys. Rev. A*, 76(4):042319, oct 2007.
 - [61] Dany Lachance-Quirion, Yutaka Tabuchi, Seiichiro Ishino, Atsushi Noguchi, Toyofumi Ishikawa, Rekishi Yamazaki, and Yasunobu Nakamura. Resolving quanta of collective spin excitations in a millimeter-sized ferromagnet. *Sci. Adv.*, 3(7):e1603150, jul 2017.
 - [62] M D LaHaye, O Buu, B Camarota, and K C Schwab. Approaching the quantum limit of a nanomechanical resonator. *Science*, 304(5667):74–7, apr 2004.
 - [63] M D LaHaye, J Suh, P M Echternach, K C Schwab, and M L Roukes. Nanomechanical measurements of a superconducting qubit. *Nature*, 459(7249):960–4, jun 2009.
 - [64] K M Lakin. Thin film resonators and filters. *Proc. - IEEE Ultrason. Symp.*, 2:895–906, 1999.
 - [65] F Lecocq, J D Teufel, J Aumentado, and R W Simmonds. Resolving the vacuum fluctuations of an optomechanical system using an artificial atom. *Nat. Phys.*, 11(8):635–639, aug 2015.
 - [66] Hanxiao Liang, Rui Luo, Yang He, Haowei Jiang, and Qiang Lin. High-quality lithium niobate photonic crystal nanocavities. *Optica*, 4(10):1251, oct 2017.
 - [67] James J. Licari and George Whitfield. Anisotropic piezoelectric polaron. *Phys. Rev. B*, 9(4):1432–1440, feb 1974.
 - [68] Max Ludwig, Amir H. Safavi-Naeini, Oskar Painter, and Florian Marquardt. Enhanced Quantum Nonlinearities in a Two-Mode Optomechanical System. *Phys. Rev. Lett.*, 109(6):063601, aug 2012.
 - [69] H Mabuchi. Cavity Quantum Electrodynamics: Coherence in Context. *Science (80-.).*, 298(5597):1372–1377, nov 2002.
 - [70] Gregory MacCabe, Hengjiang Ren, Jie Luo, Justin Cohen, Hengyun Zhou, Anthony Ardzizzi, and Oskar Painter. Optomechanical Measurements of Ultra-Long-Lived Microwave Phonon Modes in a Phononic Bandgap Cavity. *Bull. Am. Phys. Soc.*, 2018.
 - [71] Gregory S. MacCabe, Hengjiang Ren, Jie Luo, Justin D. Cohen, Hengyun Zhou, Alp Sipahigil, Mohammad Mirhosseini, and Oskar Painter. Phononic bandgap nano-acoustic cavity with ultralong phonon lifetime. *arXiv Prepr. arXiv1901.04129*, 2019.

- [72] E. B. Magnusson, B. H. Williams, R. Manenti, M. S. Nam, a. Nersisyan, M. J. Peterer, a. Ardavan, and P. J. Leek. Surface acoustic wave devices on bulk ZnO crystals at low temperature. *Appl. Phys. Lett.*, 106(6):4–7, 2015.
- [73] Riccardo Manenti, Anton F. Kockum, Andrew Patterson, Tanja Behrle, Joseph Rahamim, Giovanna Tancredi, Franco Nori, and Peter J. Leek. Circuit quantum acoustodynamics with surface acoustic waves. *Nat. Commun.*, 8(1):975, dec 2017.
- [74] Vladimir E Manucharyan. *Superinductance*. PhD thesis, Yale University, 2012.
- [75] Vladimir E Manucharyan, Jens Koch, Leonid I Glazman, and Michel H Devoret. Fluxonium: Single cooper-pair circuit free of charge offsets. *Science (80-.).*, 326(5949):113–116, 2009.
- [76] Nicholas A Masluk. *Reducing the losses of the fluxonium artificial atom*. PhD thesis, Yale University, 2012.
- [77] Nicholas A Masluk, Ioan M Pop, Archana Kamal, Zlatko K Minev, and Michel H Devoret. Microwave Characterization of Josephson Junction Arrays : Implementing a Low Loss Superinductance. 137002(September):1–5, 2012.
- [78] Katherine C. McCormick, Jonas Keller, Shaun C. Burd, David J. Wineland, Andrew C. Wilson, and Dietrich Leibfried. Quantum-enhanced sensing of a single-ion mechanical oscillator. *Nature*, 572(7767):86–90, aug 2019.
- [79] Seán M Meenehan, Justin D Cohen, G. S. MacCabe, Francesco Marsili, Matthew D Shaw, and Oskar Painter. Pulsed Excitation Dynamics of an Optomechanical Crystal Resonator near Its Quantum Ground State of Motion. *Phys. Rev. X*, 5(4):041002, 2015.
- [80] Haixing Miao, Stefan Danilishin, Thomas Corbitt, and Yanbei Chen. Standard Quantum Limit for Probing Mechanical Energy Quantization. *Phys. Rev. Lett.*, 103(10):100402, sep 2009.
- [81] Bradley A. Moores, Lucas R. Sletten, Jeremie J. Viennot, and K. W. Lehnert. Cavity Quantum Acoustic Device in the Multimode Strong Coupling Regime. *Phys. Rev. Lett.*, 120(22):227701, may 2018.
- [82] A. Naik, O. Buu, M. D. LaHaye, A. D. Armour, A. A. Clerk, M. P. Blencowe, and K. C. Schwab. Cooling a nanomechanical resonator with quantum back-action. *Nature*, 443(7108):193–196, sep 2006.
- [83] R. K. Naik, N. Leung, S. Chakram, Peter Groszkowski, Y. Lu, N. Earnest, D. C. McKay, Jens Koch, and D. I. Schuster. Random access quantum information processors using multimode circuit quantum electrodynamics. *Nat. Commun.*, 8(1):1904, dec 2017.

- [84] Matthew Neeley, M. Ansmann, Radoslaw C. Bialczak, M. Hofheinz, N. Katz, Erik Lucero, A. O’Connell, H. Wang, A. N. Cleland, and John M. Martinis. Process tomography of quantum memory in a Josephson-phase qubit coupled to a two-level state. *Nat. Phys.*, 4(7):523–526, jul 2008.
- [85] Simon E. Nigg, Hanhee Paik, Brian Vlastakis, Gerhard Kirchmair, S. Shankar, Luigi Frunzio, M. H. Devoret, R. J. Schoelkopf, and S. M. Girvin. Black-Box Superconducting Circuit Quantization. *Phys. Rev. Lett.*, 108(24):240502, jun 2012.
- [86] Atsushi Noguchi, Rekishu Yamazaki, Yutaka Tabuchi, and Yasunobu Nakamura. Qubit-Assisted Transduction for a Detection of Surface Acoustic Waves near the Quantum Limit. *Phys. Rev. Lett.*, 119(18):180505, nov 2017.
- [87] C. F. Ockeloen-Korppi, E. Damskägg, J.-M. Pirkkalainen, M. Asjad, A. A. Clerk, F. Massel, M. J. Woolley, and M. A. Sillanpää. Stabilized entanglement of massive mechanical oscillators. *Nature*, 556(7702):478–482, apr 2018.
- [88] A D O’Connell, M Hofheinz, M Ansmann, Radoslaw C Bialczak, M Lenander, Erik Lucero, M Neeley, D Sank, H Wang, M Weides, J Wenner, John M Martinis, and a N Cleland. Quantum ground state and single-phonon control of a mechanical resonator. *Nature*, 464(7289):697–703, 2010.
- [89] Nissim Ofek, Andrei Petrenko, Reinier Heeres, Philip Reinhold, Zaki Leghtas, Brian Vlastakis, Yehan Liu, Luigi Frunzio, S M Girvin, L Jiang, Mazyar Mirrahimi, M H Devoret, and R J Schoelkopf. Extending the lifetime of a quantum bit with error correction in superconducting circuits. *Nature*, 536(7617):441, 2016.
- [90] T A Palomaki, J D Teufel, J D Simmonds, and K W Lehnert. Entangling Mechanical Motion with Microwave Fields. *Science (80-.).*, 342(6159):710–713, 2013.
- [91] Rishi N. Patel, Zhaoyou Wang, Wentao Jiang, Christopher J. Sarabalis, Jeff T. Hill, and Amir H. Safavi-Naeini. Single-Mode Phononic Wire. *Phys. Rev. Lett.*, 121(4):040501, jul 2018.
- [92] Marek Pechal, Patricio Arrangoiz-Arriola, and Amir H Safavi-Naeini. Superconducting circuit quantum computing with nanomechanical resonators as storage. *Quantum Sci. Technol.*, 4(1):015006, sep 2018.
- [93] Luca Pezzè, Augusto Smerzi, Markus K. Oberthaler, Roman Schmied, and Philipp Treutlein. Quantum metrology with nonclassical states of atomic ensembles. *Rev. Mod. Phys.*, 90(3):035005, sep 2018.

- [94] J-M Pirkkalainen, S U Cho, Jian Li, G S Paraoanu, P J Hakonen, and M A Sillanpää. Hybrid circuit cavity quantum electrodynamics with a micromechanical resonator. *Nature*, 494(7436):211–5, feb 2013.
- [95] J-M Pirkkalainen, S U Cho, F Massel, J Tuorila, T T Heikkilä, P J Hakonen, and M A Sillanpää. Cavity optomechanics mediated by a quantum two-level system. *Nat. Commun.*, 6:6981, jan 2015.
- [96] Flavius V. Pop, S. Abhay Kochhar, Gabriel Vidal-Alvarez, and Gianluca Piazza. Laterally vibrating lithium niobate MEMS resonators with 30% electromechanical coupling coefficient. *2017 IEEE 30th Int. Conf. Micro Electro Mech. Syst.*, 2017.
- [97] T. P. Purdy, R. W. Peterson, C. A. Regal, C. A. Fuchs, H. J. Kimble, and E. S. Polzik. Observation of Radiation Pressure Shot Noise on a Macroscopic Object. *Science (80-.).*, 339(6121):801–804, feb 2013.
- [98] A. P. Reed, K. H. Mayer, J. D. Teufel, L. D. Burkhardt, W. Pfaff, M. Reagor, L. Sletten, X. Ma, R. J. Schoelkopf, E. Knill, and K. W. Lehnert. Faithful conversion of propagating quantum information to mechanical motion. *Nat. Phys.*, 13(12):1163–1167, dec 2017.
- [99] Susanne Richer. *Perturbative analysis of two-qubit gates on transmon qubits*. PhD thesis, 2013.
- [100] Ralf Riedinger, Sungkun Hong, Richard A. Norte, Joshua A. Slater, Juying Shang, Alexander G. Krause, Vikas Anant, Markus Aspelmeyer, and Simon Gröblacher. Non-classical correlations between single photons and phonons from a mechanical oscillator. *Nature*, 530(7590):313–316, jan 2016.
- [101] Ralf Riedinger, Andreas Wallucks, Igor Marinković, Clemens Löschnauer, Markus Aspelmeyer, Sungkun Hong, and Simon Gröblacher. Remote quantum entanglement between two micromechanical oscillators. *Nature*, 556(7702):473–477, apr 2018.
- [102] Amir H. Safavi-Naeini. *Quantum Optomechanics with Silicon Nanostructures*. PhD thesis, California Institute of Technology, 2013.
- [103] Amir H. Safavi-Naeini, Jasper Chan, Jeff T. Hill, Thiago P. Mayer Alegre, Alex Krause, and Oskar Painter. Observation of Quantum Motion of a Nanomechanical Resonator. *Phys. Rev. Lett.*, 108(3):033602, jan 2012.
- [104] Amir H. Safavi-Naeini, Simon Gröblacher, Jeff T. Hill, Jasper Chan, Markus Aspelmeyer, and Oskar Painter. Squeezed light from a silicon micromechanical resonator. *Nature*, 500(7461):185–189, aug 2013.

- [105] Amir H. Safavi-Naeini, Jeff T. Hill, Seán Meenehan, Jasper Chan, Simon Gröblacher, and Oskar Painter. Two-Dimensional Phononic-Photonic Band Gap Optomechanical Crystal Cavity. *Phys. Rev. Lett.*, 112(15):153603, 2014.
- [106] Amir H. Safavi-Naeini and Oskar Painter. Design of optomechanical cavities and waveguides on a simultaneous bandgap phononic-photonic crystal slab. *Opt. Express*, 18(14):14926, jul 2010.
- [107] Amir H. Safavi-Naeini and Oskar Painter. Proposal for an optomechanical traveling wave phonon-photon translator. *New J. Phys.*, 13, 2011.
- [108] Amir H. Safavi-Naeini and Oskar Painter. Optomechanical Crystal Devices. In Markus Aspelmeyer, Tobias J Kippenberg, and Florian Marquardt, editors, *Cavity Optomech.*, Quantum Science and Technology, pages 195–231. Springer Berlin Heidelberg, Berlin, Heidelberg, 2014.
- [109] K. J. Satzinger, Y. P. Zhong, H.-S. Chang, G. A. Peairs, A. Bienfait, Ming-Han Chou, A. Y. Cleland, C. R. Conner, É. Dumur, J. Grebel, I. Gutierrez, B. H. November, R. G. Povey, S. J. Whiteley, D. D. Awschalom, D. I. Schuster, and A. N. Cleland. Quantum control of surface acoustic-wave phonons. *Nature*, 563(7733):661–665, nov 2018.
- [110] A. Schliesser, P. Del’Haye, N. Nooshi, K. J. Vahala, and T. J. Kippenberg. Radiation Pressure Cooling of a Micromechanical Oscillator Using Dynamical Backaction. *Phys. Rev. Lett.*, 97(24):243905, dec 2006.
- [111] J. R. Schrieffer and P. A. Wolff. Relation between the Anderson and Kondo Hamiltonians. *Phys. Rev.*, 149(2):491–492, 1966.
- [112] D. I. Schuster, A. A. Houck, J. A. Schreier, A. Wallraff, J. M. Gambetta, A. Blais, L. Frunzio, J. Majer, B. Johnson, M. H. Devoret, S. M. Girvin, and R. J. Schoelkopf. Resolving photon number states in a superconducting circuit. *Nature*, 445(7127):515–518, feb 2007.
- [113] D. I. Schuster, A. Wallraff, A. Blais, L. Frunzio, R.-S. Huang, J. Majer, S. M. Girvin, and R. J. Schoelkopf. ac Stark Shift and Dephasing of a Superconducting Qubit Strongly Coupled to a Cavity Field. *Phys. Rev. Lett.*, 94(12):123602, mar 2005.
- [114] Lucas R. Sletten, Bradley A. Moores, Jeremie J. Viennot, and Konrad W. Lehnert. Resolving Phonon Fock States in a Multimode Cavity with a Double-Slit Qubit. *Phys. Rev. X*, 9(2):21056, 2019.
- [115] A. Stockklauser, P. Scarlino, J. V. Koski, S. Gasparinetti, C. K. Andersen, C. Reichl, W. Wegscheider, T. Ihn, K. Ensslin, and A. Wallraff. Strong Coupling Cavity QED with Gate-Defined Double Quantum Dots Enabled by a High Impedance Resonator. *Phys. Rev. X*, 7(1):011030, mar 2017.

- [116] J Suh, A J Weinstein, C U Lei, E E Wollman, S K Steinke, P Meystre, A A Clerk, and K C Schwab. Mechanically detecting and avoiding the quantum fluctuations of a microwave field Title. *Science (80-.)*, 344(6189):1262–1265, 2014.
- [117] L. Sun, A. Petrenko, Z. Leghtas, B. Vlastakis, G. Kirchmair, K. M. Sliwa, A. Narla, M. Hattridge, S. Shankar, J. Blumoff, L. Frunzio, M. Mirrahimi, M. H. Devoret, and R. J. Schoelkopf. Tracking photon jumps with repeated quantum non-demolition parity measurements. *Nature*, 511(7510):444–448, jul 2014.
- [118] J. D. Teufel, T. Donner, Dale Li, J. W. Harlow, M. S. Allman, K. Cicak, A. J. Sirois, J. D. Whittaker, K. W. Lehnert, and R. W. Simmonds. Sideband cooling of micromechanical motion to the quantum ground state. *Nature*, 475(7356):359–363, jul 2011.
- [119] J. D. Teufel, Dale Li, M. S. Allman, K. Cicak, A. J. Sirois, J. D. Whittaker, and R. W. Simmonds. Circuit cavity electromechanics in the strong-coupling regime. *Nature*, 471(7337):204–208, mar 2011.
- [120] J. D. Thompson, B. M. Zwickl, A. M. Jayich, Florian Marquardt, S. M. Girvin, and J. G. E. Harris. Strong dispersive coupling of a high-finesse cavity to a micromechanical membrane. *Nature*, 452(7183):72–75, mar 2008.
- [121] Kip S. Thorne, Ronald W. P. Drever, Carlton M. Caves, Mark Zimmermann, and Vernon D. Sandberg. Quantum Nondemolition Measurements of Harmonic Oscillators. *Phys. Rev. Lett.*, 40(11):667–671, mar 1978.
- [122] Michael Tinkham. *Introduction to Superconductivity*. Dover Books, 2004.
- [123] Amit Vainsencher, K. J. Satzinger, G. A. Peairs, and A. N. Cleland. Bi-directional conversion between microwave and optical frequencies in a piezoelectric optomechanical device. *Appl. Phys. Lett.*, 109(3):033107, jul 2016.
- [124] Gabriel Vidal-álvarez, Abhay Kochhar, and Gianluca Piazza. Delay Lines Based on a Suspended Thin Film of X- Cut Lithium Niobate. *Ius 2017*, 2017.
- [125] J. J. Viennot, X. Ma, and K. W. Lehnert. Phonon-Number-Sensitive Electromechanics. *Phys. Rev. Lett.*, 121(18):183601, oct 2018.
- [126] Brian Vlastakis, Gerhard Kirchmair, Zaki Leghtas, Simon E Nigg, Luigi Frunzio, Steven M Girvin, Mazyar Mirrahimi, Michel H Devoret, and Robert J Schoelkopf. Deterministically Encoding Quantum Information Using 100-Photon Schrodinger Cat States. *Science (80-.)*, 342(6158):607–610, nov 2013.

- [127] A. Wallraff, D. I. Schuster, A. Blais, L. Frunzio, R.-S. Huang, J. Majer, S. Kumar, S. M. Girvin, and R. J. Schoelkopf. Strong coupling of a single photon to a superconducting qubit using circuit quantum electrodynamics. *Nature*, 431(7005):162–167, sep 2004.
- [128] Cheng Wang, Michael J Burek, Zin Lin, Haig A Atikian, Vivek Venkataraman, I-Chun Huang, Peter Stark, and Marko Lončar. Integrated high quality factor lithium niobate microdisk resonators. *Opt. Express*, 22(25):30924–33, dec 2014.
- [129] Renyuan Wang, Sunil A. Bhave, and Kushal Bhattacharjee. High kt2Q, multi-frequency lithium niobate resonators. *Proc. IEEE Int. Conf. Micro Electro Mech. Syst.*, pages 165–168, 2013.
- [130] Ronald Winkler. *SpinOrbit Coupling Effects in Two-Dimensional Electron and Hole Systems*. Springer-Verlag, 2003.
- [131] E E Wollman, C U Lei, A J Weinstein, J Suh, A Kronwald, F Marquardt, A A Clerk, and K C Schwab. Quantum squeezing of motion in a mechanical resonator. *Science (80-.).*, 349(6251):952–955, aug 2015.
- [132] X. Zhou, V. Schmitt, P. Bertet, D. Vion, W. Wustmann, V. Shumeiko, and D. Esteve. High-gain weakly nonlinear flux-modulated Josephson parametric amplifier using a SQUID array. *Phys. Rev. B*, 89(21):214517, jun 2014.
- [133] Chang-Ling Zou, Xu Han, Liang Jiang, and Hong X Tang. Cavity piezomechanical strong coupling and frequency conversion on an aluminum nitride chip. *Phys. Rev. A*, 94:13812, 2016.
- [134] Jie Zou. High Quality Factor Lamb Wave Resonators, MS Thesis. 2014.